11-8-2016

Effective Post-Tensioned Splicing System for Prestressed Concrete Piles

Zhongxin Wu
University of South Florida, wuzx88@yahoo.com

Effective Post-Tensioned Splicing System for Prestressed Concrete Piles

by

Zhongxin Wu

A dissertation submitted in partial fulfillment
of the requirements for the degree of
Doctor of Philosophy
Department of Civil and Environmental Engineering
College of Engineering
University of South Florida

Co-Major Professor: Rajan Sen, Ph.D.
Co-Major Professor: Gray Mullins, Ph.D.
Michael Stokes, Ph.D.
Autar Kaw, Ph.D.
Kandethody Ramachandran, Ph.D.

Date of Approval:
October 24, 2016

Keywords: Precast, Staggered Anchorage, Transfer Zone, Flexural Test, Finite Element

DEDICATION

Dedicated to my parents Xianzhi Wu and Xiuzhi Wang who always love me.

ACKNOWLEDGMENTS

First, I would like to thank my major professors, Dr. Rajan Sen and Dr. Gray Mullins for their great guidance, profound knowledge, kind support, and constant encouragement during the entire period of the research project.

I thank Dr. Michael Stokes, Dr. Autar Kaw, and Dr. Kandethody Ramachandran for their assistance and serving as my committee members.

I want to thank my colleagues Miles Mullins, Kevin Johnson, and Jeffrey Vomacka for their help during the tests.

Finally, I thank my family across the Pacific Ocean for their consistent love. I will live with them soon in China after graduation from USF.

TABLE OF CONTENTS

LIST OF TABLES

LIST OF FIGURES

ABSTRACT

Precast prestressed concrete piles are widely used in deep foundation construction. Due to unexpected site soil conditions and difficulties associated with transportation and handling long precast piles, splicing is sometimes necessary at the construction site.

Available splicing methods utilize steel type connections that are more suitable for reinforced concrete construction and result in limited tensile capacity at the splice. This dissertation describes studies associated with the development of a new post-tensioned splicing system using staggered, embedded anchorages. The new system has the potential to provide the same tensile capacity as a one piece prestressed pile.

To develop the post-tensioned splicing system it was necessary to conduct varied numerical analyses to solve immediate technical problems associated with the design, fabrication and testing of a prototype. This included the design of a self-stressing prestressing bed, optimization of the shape of the embedded anchorages and their layout within the piles being spliced. The focus of the dissertation is on non-linear finite element studies conducted to model the flexure behavior of prototype laboratory and full-sized spliced piles in comparison to their identical non-spliced counterpart.

Though finite element analysis of prestressed elements is not new, issues relating to modeling post-tensioned, spliced elements with embedded, staggered anchorages have not been the subject of any previous investigation and constitute the principal contribution of this study.

Nonlinear finite element analysis was conducted using ANSYS. The William-Warnke failure criterion used to establish concrete failure. A three-dimensional analysis was conducted in which SOLID65 element was used for modeling concrete and LINK8 for the prestressing strands. The post-tensioning ducts were modeled using PIPE20 elements. Perfect bond was assumed between the concrete and the ducts. Embedded anchorages were modeled as fixed locations within the concrete. Epoxy used to join the two splicing surfaces was modeled using contact elements. Since the layout of the post-tensioning ducts was staggered, a full model was required. In contrast, advantage was taken of symmetry for the analysis of the one piece controls.

The finite element model was able to accurately capture the flexural behavior of both the control and the spliced piles. The results suggested that tensile separation at the splice interface acted as a pivot about which the section rotated. As a result, the compression failure zone in the spliced pile was confined to a smaller region compared to the control.

The stress distribution in the spliced pile indicated that the concrete in the cover above the splice was crushed at the ultimate stage before the steel had yielded. As a result, the ultimate capacity of the spliced pile was controlled by concrete failure.

The results also indicated that, among the multiple layers of post-tensioning strands, only one approached yield while others remained in the elastic range. As a result, when the applied load was released, the spliced pile rebounded back to a large degree, which resulted in a much smaller residual permanent deformation. This behavior of a spliced pile can be beneficial for structures in a seismic zone because it will induce smaller secondary moments.

This study helped to refine and improve the new post-tensioned splicing system. Its availability makes it possible to extend and further improve the concept without the need for costly prototype fabrication and testing.

CHAPTER 1: INTRODUCTION

1.1 Introduction

Precast concrete piles have been used extensively in deep foundation construction. The lengths of piles are restricted by weight concerns and difficulties associated with transportation and handling. Shorter pile segments can reduce internal stresses and cracking arising from weight and require smaller equipment for manufacture, transport, and handling. In cases where the pile length exceeds 120 ft, installation becomes difficult and a splicing pile procedure is required (Figure 1.1).

Figure 1.1 Deep foundation construction.

Moreover, due to unexpected geotechnical conditions at the construction site, longer pile lengths may be needed to achieve the required structural capacity. In such circumstances,

splicing makes this possible. Therefore, an efficient splicing technique for precast prestressed concrete piles is necessary in deep foundation construction.

1.2 Literature Review

1.2.1 Available Systems

Several pile splice systems have been developed and are used in construction, Bruce and Hebert 1974, Venuti 1980, Gamble and Bruce 1990. These include epoxy doweled method, sleeve splicing method, shear key type, bolted method, welded system, and full-length post-tensioning. The advantages and disadvantages of these systems are reviewed in the following sections.

1.2.2 Epoxy Doweled Splice Method

The doweled splice is bonded by epoxy. Dowel holes are cast or field drilled into the bottom pile section (Fig. 1.2). The top pile segment with rebar dowels protruding 3~6 feet from the end and the grout or epoxy in the holes cures around the dowels. The strength of the pile splice is limited and the tensile stress during driving is restricted to 250 psi per FDOT Specifications (2010). Although material cost of this method is low, it requires that the pile top segment be held in place until the epoxy or grout cures, which causes the construction delays.

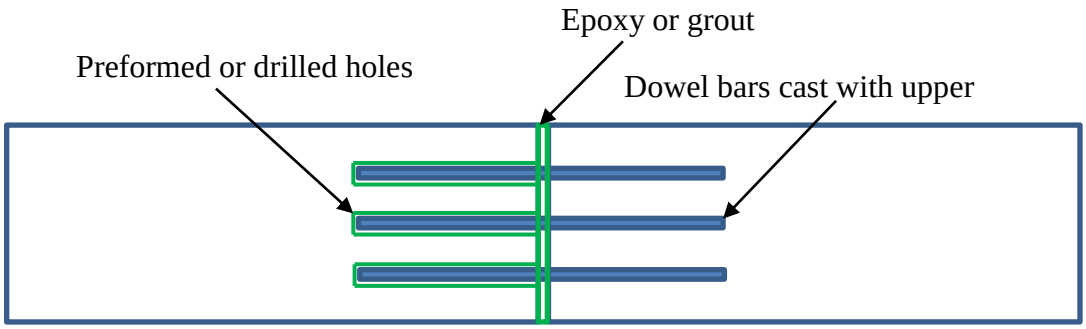

Figure 1.2 Epoxy doweled splice.

1.2.3 Sleeve Splice Method

In this system, a steel tube is placed between two voided pile segments (Cook et al., 2003). To transfer load, the steel tube is grouted to the piles (Fig. 1.3). Additionally, 0.5 in. diameter steel bars are spirally wound and welded to the steel tubing to improve the bond between steel tubing and the pile.

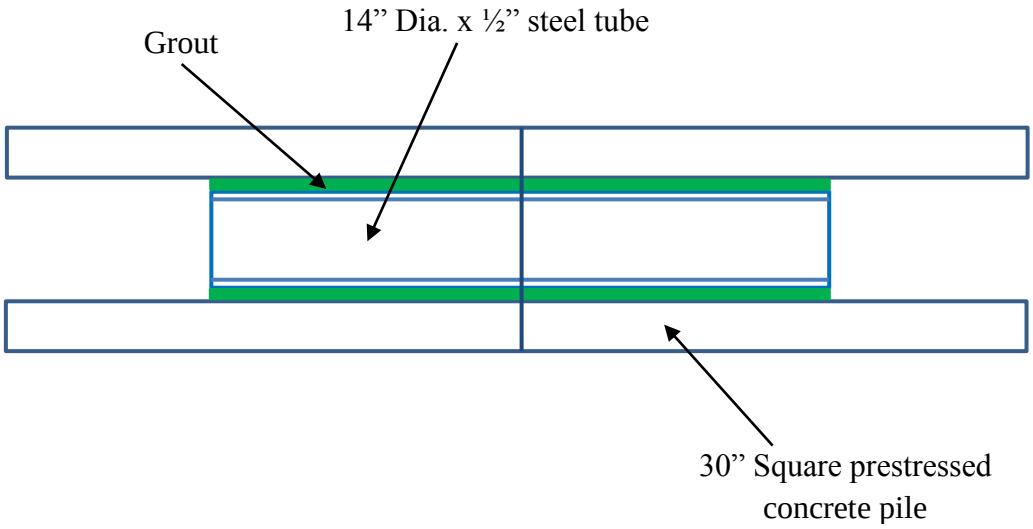

Figure 1.3 Sleeve splice method.

Using this sleeve splice method, driving cannot resume until the grout has reached the design strength. Load transfer mechanism totally depends on the bond between the tubing and the pile. If bond failure occurs, driving failure is inevitable.

1.2.4 Shear Key Type Splicing System

The typical system of shear key type splice is the Kie-Lock system, which is also known as Sure-Lock system. The steel connection components are cast within the pile segments (Fig. 1.4). The caps are joined and bonded together by high strength steel pins which are inserted into the alignment grooves. The interlocking bars go through the steel plates to the location of development length based on the theory of reinforced concrete design to form a shear key

(Ansley, 2002, Ansley et al. 2011). Although this method is widely used, the exposed steel connection has corrosion concerns. Meanwhile, during pile driving, FDOT Specifications (2010) require that the tensile stress of the steel type splice shall not exceed 500 psi, which affects the pile driving efficiency.

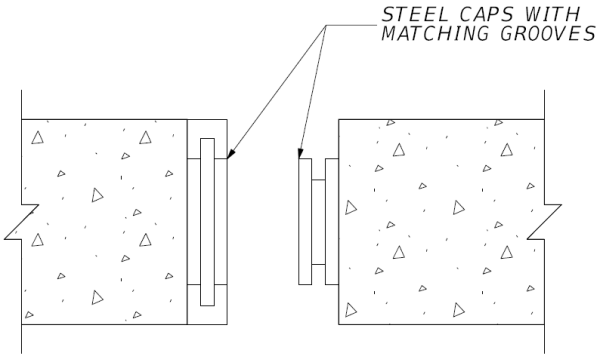

Figure 1.4 Embedded steel caps.

1.2.5 Bolted Splice Method

This pile splice method uses the bolted system, such as the Japanese Bolted Splice used by Tokyo Concrete Industry Company (1968). End steel plates are embedded in pile segments. The end plates have recesses in the concrete to provide the spaces for tightening the hex nuts on threaded rods. During experiments, brittle failure was observed due to the large recesses at the edges of pile cross sections. Strand slippage was also observed. The recess areas in concrete restrict the strand configurations, which add to the disadvantages of the bolted splice method.

1.2.6 Welded Splicing System

This welded splice system is adopted in splicing the spun-cast cylindrical piles by Industrial Concrete Products, Inc. (ICP). The cylindrical piles have end plates that can be welded together to form this type of splice. Based on the research of Beitelman (2001), there are several concerns about this splicing method, including brittle failure, limited concrete cover, and

cracking under service loads. This splicing technique has high cost requirements of equipment and labor. The disadvantages also include the occurrence of fatigue failure.

1.2.7 Macalloy Splice Technique

Currently, there are only two types of post-tensioning splice systems ever to be used including Macalloy splice and GCP splice. Macalloy splice uses special tension bars which are threaded at both ends to receive a coupler or turnbuckle (Fig. 1.5). The 1 ½ in. grouting ducts are installed in position before cast of pile segments.

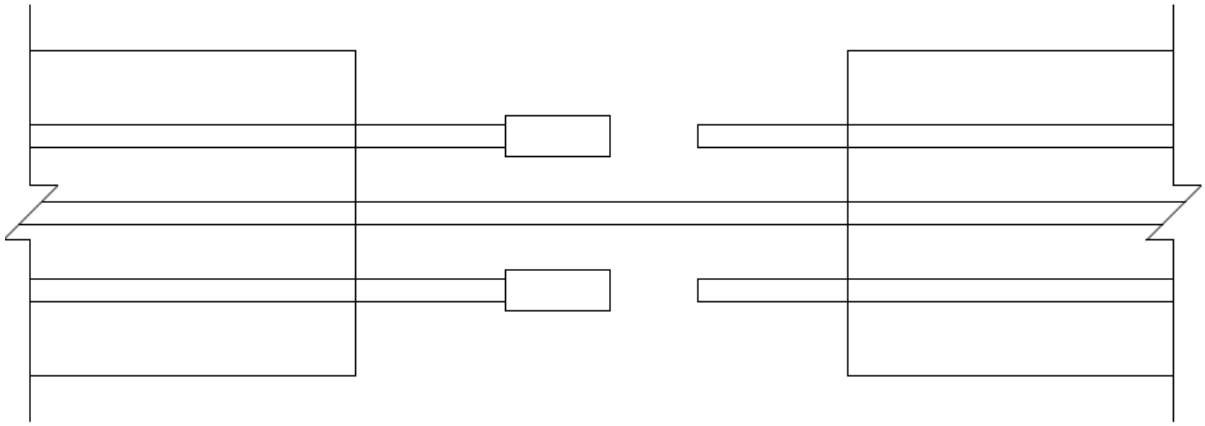

Figure 1.5 Macalloy splice technique.

The lower segment contains the Macalloy bars which are anchored by a sleeve at the end of bars. The bars extend out from the lower segment. The upper segment is cast with high-strength dowel. Macalloy bars are threaded into the embedded ducts. Once the lower segment is driven into position, the upper segment is then positioned on top.

Although this method is practical, it is patented in Britain. There is no published case study of its application in the U.S. This method applies the full length post-tensioning, which adds unwanted compressive stress to the entire pile.

1.2.8 GCP (Gulf Coast Prestress) Splice

The GCP splice is another post-tensioning splice system. It is primarily used in spun cast concrete piles (Chamberlain 2010). The pile segments are spun cast as 16 ft sections. Centrifugal force can achieve a high density concrete. The resulting pile has low porosity and is impervious to moisture. The corrosion-resistance of the piles has been found to be satisfactory under severe environmental exposure (Lau et al. 2006).

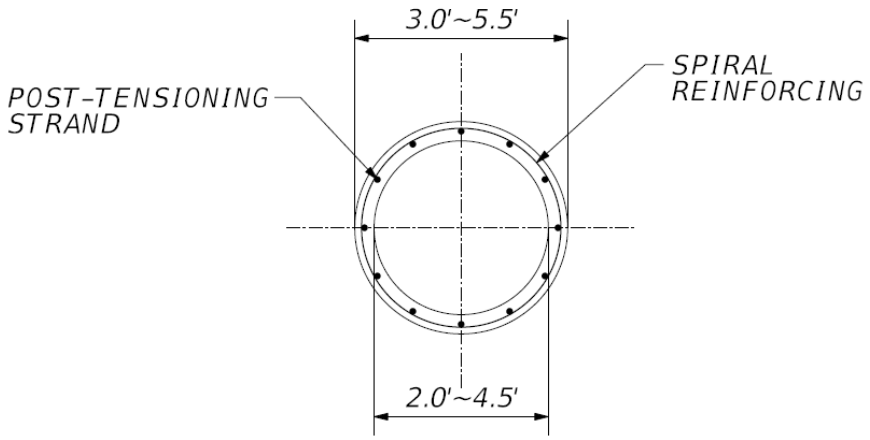

Figure 1.6 Cylinder pile with post-tensioning strands.

The diameter of the formed strand ducts is 1 3/8 in. Before pile assembly, the strand ducts are aligned in positions and the strands go through the ducts (Fig. 1.6). The post-tensioning forces are then applied to join the segments together to the designed length. After that, the ducts are pressure grouted.

Although this splicing system is widely used in the gulf coast area, the pile length has to be decided before the pile can be assembled. It means that the length is determined from load tests first and the required number of segments is then fixed which is not flexible if subsequent splices are required at the construction site.

Based on the literature review, it can be seen that, among the current methods, several problems exist such as complex construction, cost, lack of durability in a marine environment, and time taken for installation.

The main concern is the low tensile strength of the splice region without full restoration of pre-compression. FDOT Specifications (2010) have restricted the tensile stress in the mechanical and epoxy dowel splices during pile driving.

Although Macalloy splice and GCP splice restore the pre-compression across the splice, these methods add additional compressive stresses to the entire length of piles. At the same time, FDOT Specifications (2010) require the strength of pile splice to meet following criteria shown in the following Table 1.1.

Table 1.1 Bending capacities of FDOT prestressed concrete piles

Pile Size (in.)	Bending Capacity (k-ft)
18	245
20	325
24	600
30	950

Therefore, it is a challenging research task to solve these problems and meet the FDOT requirements simultaneously. There is a need to provide an efficient concrete pile splice. This method can also address corrosion resistance in marine environments.

1.3 Objectives

To solve the aforementioned difficulties, a method of post-tensioning splice using dual staggered embedded anchorages was invented by Mullins and Sen (2015). This uses intermediate post-tensioning to splice piles.

This system can restore the full prestress across the splice. More importantly, this system confines the pre-compression within the transfer zone instead of the entire length of the piles. The embedded internal intermediate anchorage eliminates deviations in the strands and corrosion concerns. This staggered layout of the anchorages also decreases the superimposition of stresses in the transfer zone of pile segments. By placing the strands in pairs, there are no unwanted torsional or bending stresses.

To implement the new post-tensioning splice concept using dual embedded anchorages, various analyses were undertaken. The complex behavior of splicing system under load conditions was studied experimentally and numerically. Nonlinear behavior of the spliced pile was investigated. The methods of analyzing and modeling the post-tensioning spliced pile using dual embedded anchorages were developed and examined.

1.4 Organization of Dissertation

This dissertation is organized into five chapters and five appendices. The conceptual splice design and laboratory prototyping are discussed in Chapter 2.

Chapter 3 presents results of experimental and finite element analysis of the laboratory spliced pile specimens. Nonlinear finite element analysis is presented and the predictions compared with experimental results.

Chapter 4 presents the corresponding information for full-scale spliced piles. Based on accumulated experience, design improvements are incorporated and tested to verify splice efficiency. The principal conclusions are summarized in Chapter 5.

Five appendices are included at the end of this dissertation. Appendix A summarizes the calculations of prestress loss based on AASHTO lump sum method. Appendix B presents details of the strain compatibility analysis.

Appendix C provides the properties of materials used in the tests and analysis. Appendix D presents the key information of finite element analysis. Appendix E includes the copyright authorization.

CHAPTER 2: CONCEPT SPLICE DESIGN AND LABORATORY PROTOTYPING

2.1 Introduction

The critical stresses in piles are experienced during its installation. For conventional spliced precast prestressed concrete piles, tensile stresses are difficult to restore at the splice. Therefore, FDOT specifies the limits on tensile stresses for spliced piles, such as 250 psi for epoxy dowel splices and 500 psi for steel type splices (FDOT 2010).

To prevent failure, spliced piles have to be driven slowly and construction delays are therefore inevitable. This chapter describes the conceptual splice design and laboratory prototyping to implement the new concept of post-tensioning splice using dually embedded anchorages technique.

2.2 Conceptual Post-Tensioning Pile Splice

The basic concepts include (1) intermediate anchorages, (2) embedded anchorages with full length post-tensioning, (3) combination of intermediate and (4) embedded anchorages, and embedded strands with intermediate anchorages.

The design alternatives 1, 3, and 4 confine the post-tensioning stress within transfer length and avoid the full-length post-tensioning. However, these design concepts result in construction complexity due to inclined openings for external anchorages. Potential corrosion problem of the external anchorages make design concepts less desirable.

The alternative 2 uses standard prestressing chucks and the strands extending the full length throughout the upper pile segment, which is a revision of the Macalloy splice concept.

Embedded anchorages could solve the corrosion problem. However, the full length post-tensioning causes the entire top pile in a state of unnecessary overstress.

To solve the aforementioned problems, a new concept of post-tensioning splice technique using dual embedded anchorages was developed (Mullins and Sen 2015) shown in Fig.2.1.

Figure 2.1 Post-tensioning splice with dual embedded anchorages.

The anchorages will be fabricated from prestressing chucks and revisions will be required to feed the ducts. The wedges in the chucks allow the strand to be inserted and the strands could not be pulled backward. Thus the strands are locked into positions firmly.

The strands will be inserted in the upper pile segment ducts and extend to the top of the pile. In the process of splicing, strands will be clamped to prevent moving upward. The strands will be inserted into the lower pile anchorages until they are fully embedded. Then the strands will be stressed from the top to reach the prestress level as the monolithic pile.

The new concept will solve the problem of overstress on entire pile and confine the post-tensioning stress within the transfer zone. The prestress over the splice interface can be ensured by this new concept.

2.3 Implementation of New Concept of Splice

To implement the new splice concept into a prototype, a series of laboratory studies were undertaken to develop the concept and evaluate its feasibility. The laboratory studies included component fabrication, assembly, and testing.

A prototype was developed by implementing the new concept for a 14 in. square precast prestressed concrete pile specimen. The cross section of the pile specimen is shown in Fig.2.2. It used eight 7-wire ½" low relaxation GR270 strands. Spiral ties were W3.4.

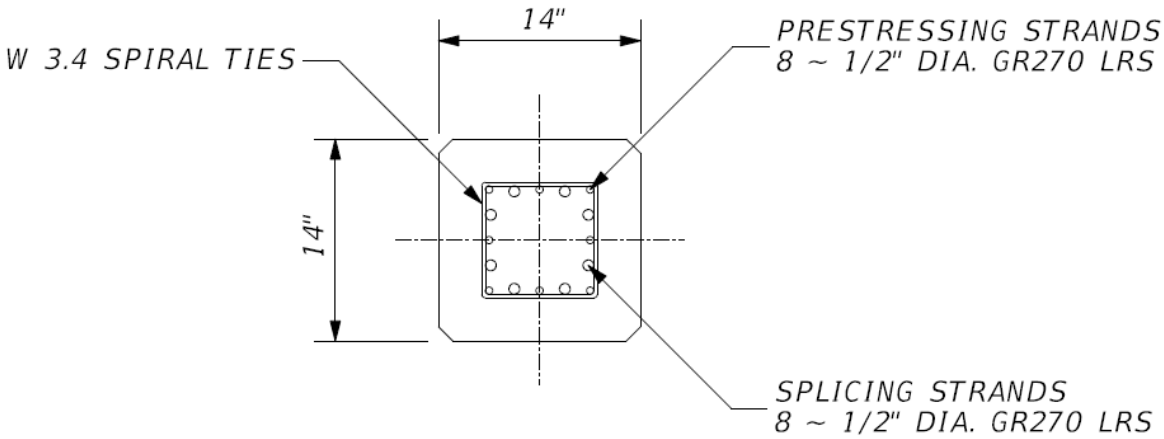

Figure 2.2 Cross section of 14 in. concrete spliced pile.

Conventional stressing equipment is typically used for strand sizes of 0.5 in., 0.5 in. special, or 0.6 in (Naaman 2004). Larger 0.7 in. strands are not commonly available since it requires larger stressing jacks (Schuler 2009). The size selection of splicing strands was therefore restricted.

To provide similar effective prestress and ultimate strength as the one-piece pile, the size of strands, number of strands, and their locations were kept the same as for the prototype.

The available space for positioning the post-tensioning duct is between the prestressing strands. Therefore, the practical solution was to locate one splicing strand every space between the pile strands. These are identified by the larger circles along the perimeter in Fig. 2.2.

2.4 Layout Design of Post-Tensioning Strands

The implementation of the new concept is challenging since it will not only need to restore prestress at the splice, but also to confine the pre-compression within the transfer zone. To achieve these goals, the layout design of post-tensioning strands is important and requires accurate determination of transfer length.

The transfer length is the distance over which the prestressing force is transferred to the surrounding concrete. Based upon ACI 318 code, transfer length is given by Eq.2.1.

$$l_t = \frac{f_{pe}}{3} d_b \qquad (2.1)$$

In Eq. 2.1, l_t is the transfer length; f_{pe} is the effective prestressing stress; and d_b is the nominal diameter of the strand.

The prestressing force is transferred from strands to the concrete through bond. To evaluate the transfer length, a preliminary experiment was conducted at the Concrete Laboratory at the University of South Florida.

In the experimental test, a series of strain gages were attached to the concrete surface of the 14 in. prestressed prototype pile. These were placed at 5, 15, 25, 35, and 45 inches from each end of the pile to measure the strains at prestress transfer. Details of strain gage layout are shown in Fig. 2.3.

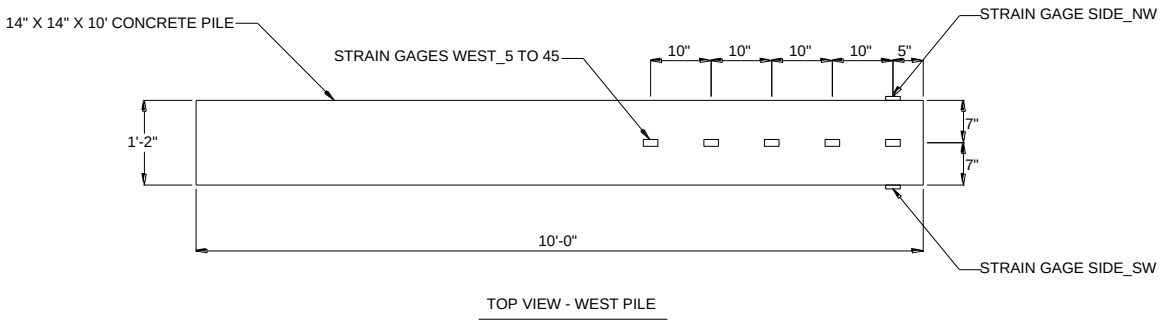

Figure 2.3 Strain gage layout details.

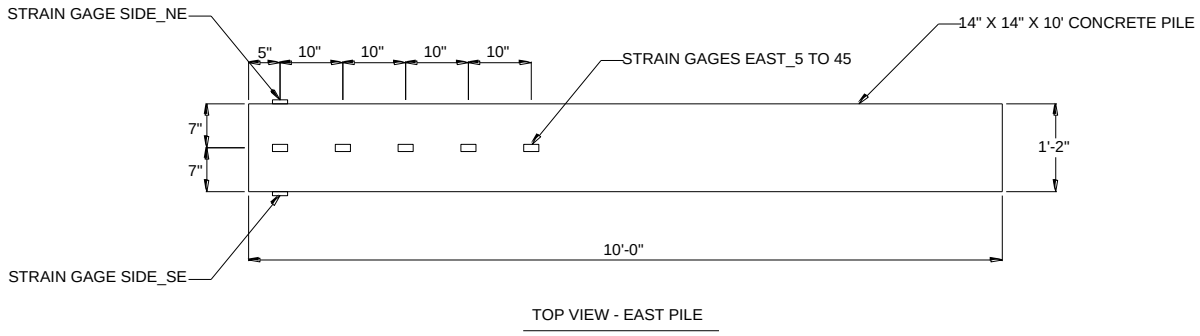

Figure 2.3 Continued.

The finished strain gage layout is shown in Fig.2.4.

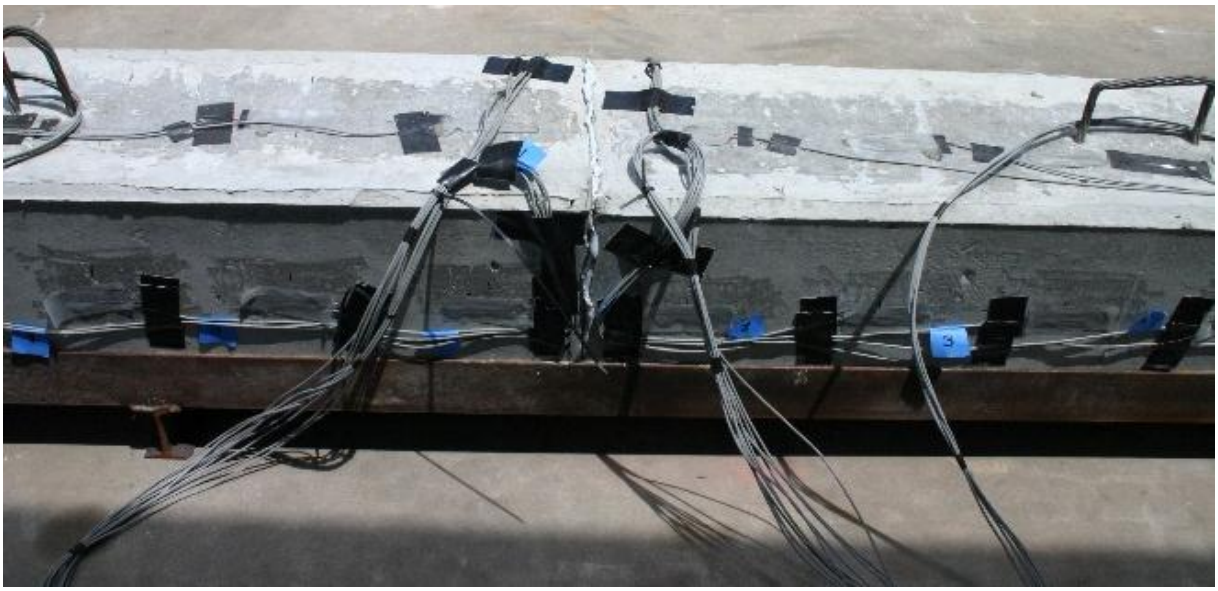

Figure 2.4 Photo of finished strain gage layout.

The results from measurements were compared against the ACI code values as shown in Fig. 2.5. The initial prestress at transfer was estimated to be 170ksi based on load cell measurement.

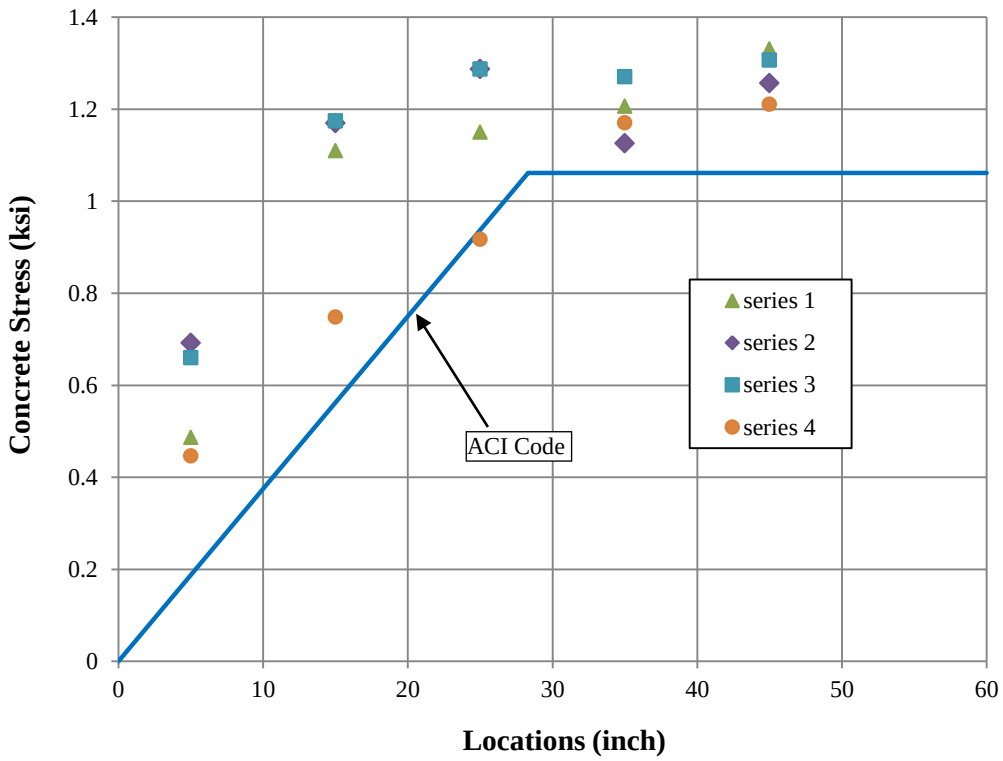

Figure 2.5 Transfer length.

It may be seen that the code value serves as a conservative envelope for the transfer length. The ACI code transfer length is 28.3" which is about $57d_b$. To cover the entire transfer zone, the post-tensioning strand needs were extended 40 inches from the splicing interface.

Since the same numbers of post-tensioning strands are used, this layout will result in overstress in the transfer zone and will cause a sudden stress jump at the anchorage locations.

To reduce the superimposed stresses in the splice zone, the embedment of post-tensioning strand layout was staggered (Mullins and Sen 2015) as shown in Fig.2.6.

The stagger was in pairs that eliminated the asymmetric torsional stress and unwanted bending stress.

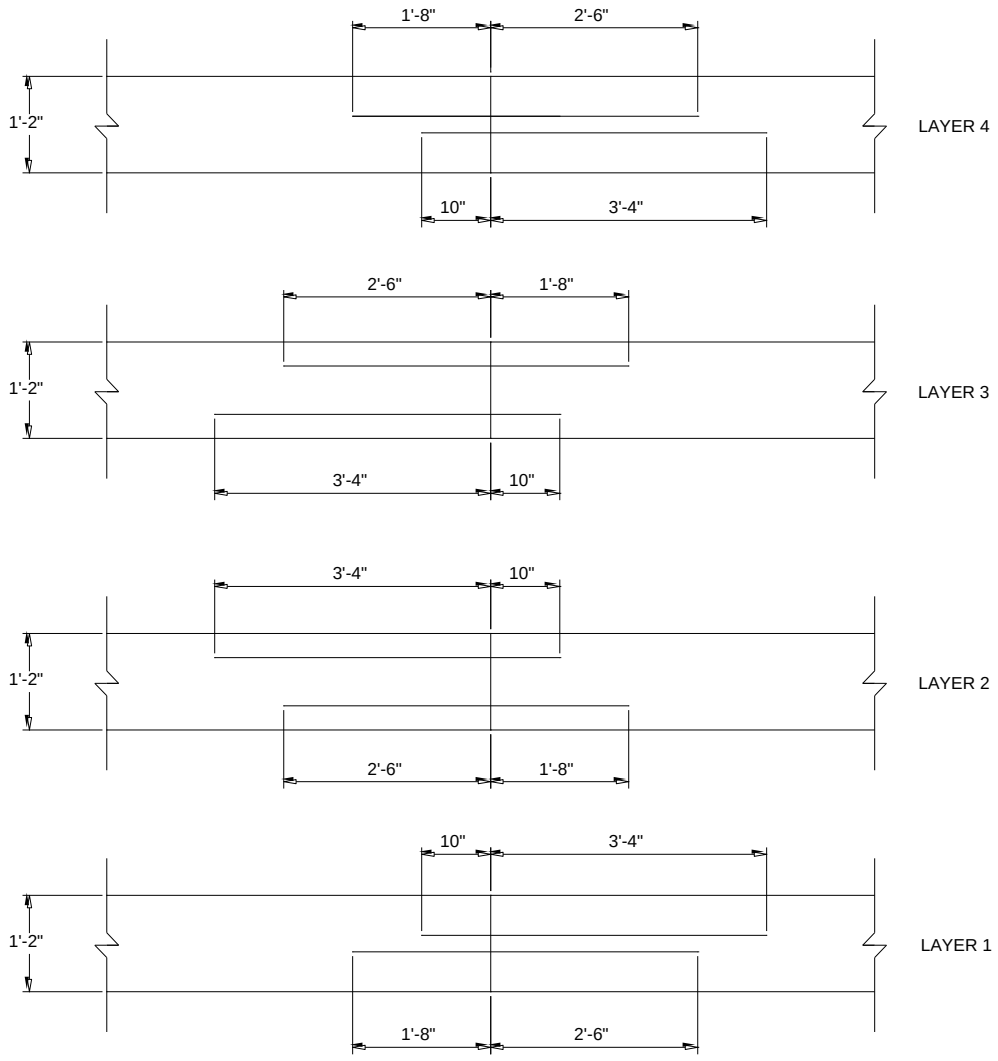

Figure 2.6 Post-tensioning strand staggered layout.

With this staggered strand layout, the magnitude of stress jump at the splicing due to the superimposed stresses was reduced. The stresses along the end of pile are shown in Fig.2.7. It may be seen that the post-tensioning splicing not only kept the required strength but also resulted in a gradual stress transfer due to the staggered layout.

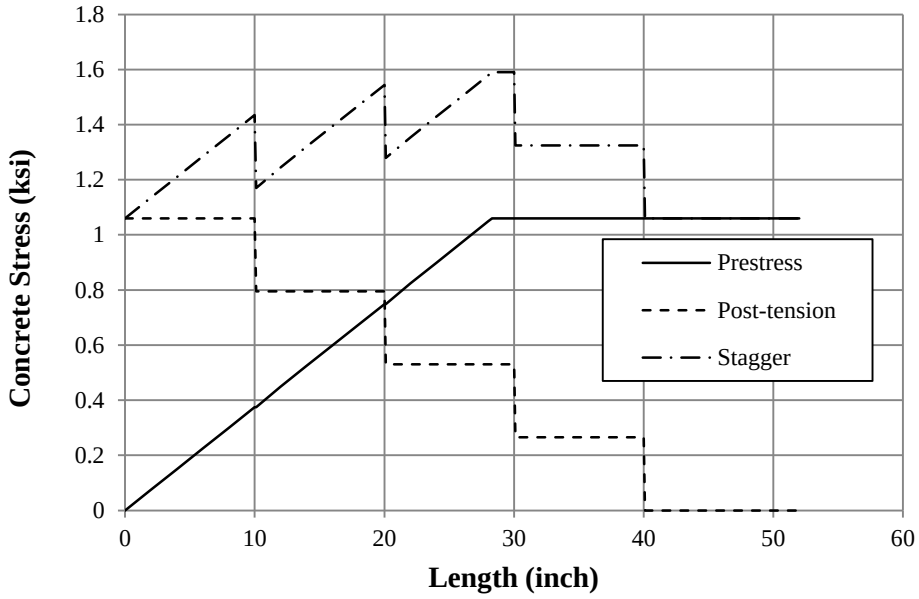

Figure 2.7 Stress distribution of post-tensioning splice.

The cross-sectional layout of the splice has fewer post-tensioning strands in the outer layers (two vs three for the prototype in Fig. 2.2). The strand forces to resist tension and compression due to flexural moment are therefore smaller compared to the one piece pile, which results in a smaller flexural capacity.

It can be seen from Fig. 2.7 that the concrete stress is larger in the transfer zone of the spliced pile. Thus, under the same flexural loading, the concrete strain in the spliced zone will reach its ultimate compressive strain earlier than the one piece pile, which also decreases the moment capacities.

2.5 Development Length

Development length is the length over which a prestressing strand can reach its ultimate strength. This length must be provided in the post-tensioning strands. Based upon ACI318-11 code, the development length of prestressing strand is shown in Fig.2.8.

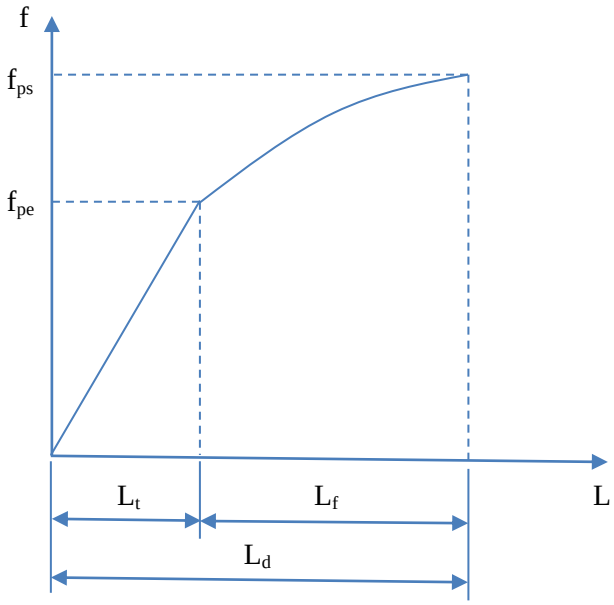

Figure 2.8 Strand stress over development length.

In Fig. 2.8, f_{pe} is the effective prestressing stress and f_{ps} is the prestressing stress in strand at its nominal ultimate strength. The length L_t is the transfer length and the length L_f is the flexural bond length. The development length L_d is given by Eq. 2.2.

$$L_d = \frac{f_{pe}d_b}{3} + (f_{ps} - f_{pe})d_b \qquad (2.2)$$

Cook et al. (2003) used a length of 57 inches. In this study, 60 inches was used to fully develop the ultimate capacity of the strands.

2.6 Strain Compatibility Analysis

The moment resistance capacity of the prototype spliced piles was calculated using strain compatibility analysis. The strain variation in the cross section is shown in Fig.2.9.

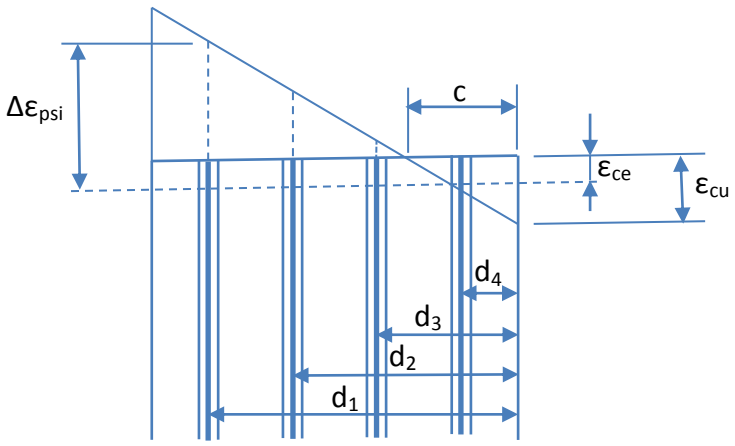

Figure 2.9 Strain diagram.

In the above figure, ε_{ce} is the concrete strain under effective post-tensioning stress; $\Delta\varepsilon_{psi}$ is the strain change in the i^{th} layer of post-tensioning strands under applied load; d_i is the distance from the extreme compressive side to the centroid of the i^{th} layer of strand; c is the depth of neutral axis; and ε_{cu} is the ultimate concrete compressive strain.

The compressive strain in concrete under prestress can be calculated as Eq. 2.3.

$$\varepsilon_{ce} = \frac{A_{ps}f_{pe}}{A_nE_c} = \frac{A_{ps}f_{pe}}{(A_g - A_{ps})E_c} \qquad (2.3)$$

The strain change in i^{th} layer of strand is calculated as Eq. 2.4.

$$\Delta\varepsilon_{psi} = \varepsilon_{ce} + \varepsilon_{cu}\left(\frac{d_i - c}{c}\right) \qquad (2.4)$$

The total strain in the i^{th} layer of strand can be found as Eq. 2.5.

$$\varepsilon_{psi} = \varepsilon_{pe} + \Delta\varepsilon_{psi} \qquad (2.5)$$

ε_{pe} is the strain of strand under effective prestressing. The concrete stress diagram is shown in Fig.2.10.

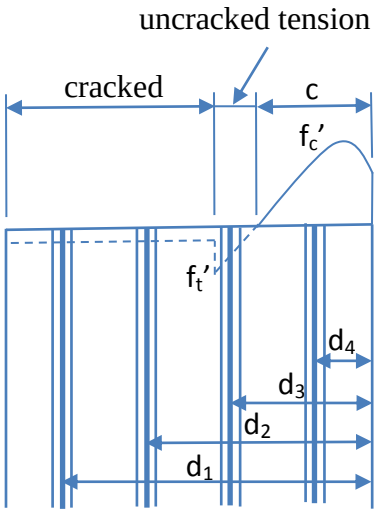

Figure 2.10 Stress diagram.

The resultant force diagram is shown in Fig.2.11.

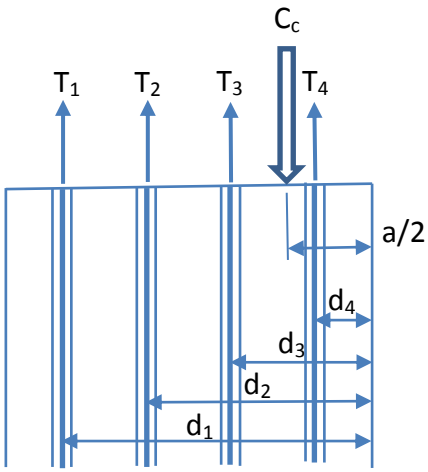

Figure 2.11 Resultants diagram.

where T_i (i = 1 to 4) is the tensile force in the i^{th} layer of strand. T_i consists of T_{ip}, the tensile force in i^{th} layer of strand, and T_{id}, the tensile force in i^{th} layer of duct.

The compressive resistance of the concrete at ultimate stage C_c is determined using a rectangular compressive stress block (Eq. 2.6).

$$C_c = 0.85 f_c' b \beta_1 c \qquad (2.6)$$

In Eq. 2.6, b is the width of concrete compression zone and β_1 is the compression block depth factor specified in ACI code. Summing up the axial forces on the section leads to the nominal force resistance.

$$P_n = C_c - \sum_i T_{ip} - \sum_i T_{id} \qquad (2.7)$$

Summing up the moments with respect to the centerline leads to the nominal moment resistance.

$$M_n = C_c \left(\frac{h}{2} - \frac{a}{2}\right) + \sum_i T_{ip} \left(d_i - \frac{h}{2}\right) + \sum_i T_{id} \left(d_i - \frac{h}{2}\right) \qquad (2.8)$$

Sum of the forces acting on the section needs to be zero. The location of the neutral axis for this case is unknown. Iteration calculations are necessary with an assumed value of c.

The forces at each layer of strands and the compression force on concrete were computed. If the sum is non-zero, a new converging value of c is selected. The iteration calculation continues until the converged result is achieved.

Based upon the calculations, the flexural capacity of spliced specimen was calculated as 1844.96 kip-in, which resulted in the failure load of 38.5 kips. The details of the calculations are shown in Appendix B.

2.7 Analysis and Design of Embedded Anchorages

The chuck used in this study was KN220, ½" model with a spring loaded end cap and wedges. The dimensions of the chucks are shown in Fig.2.12.

To fit the duct (outer diameter of 15/16"), the chucks were modified to enlarge the inner diameter of 3/4" at the anchorage side to 15/16" as shown in Figure 2.13.

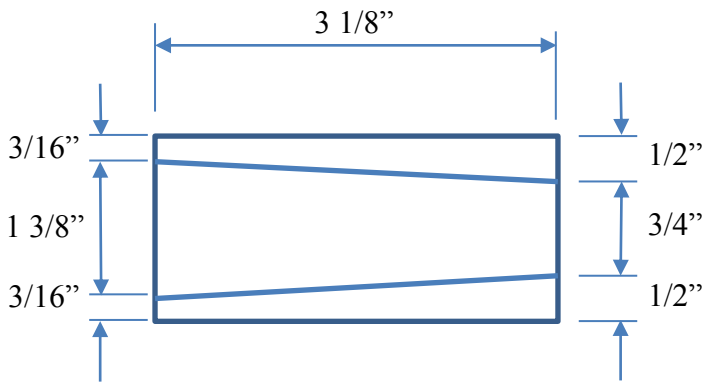

Figure 2.12 Chuck dimensions.

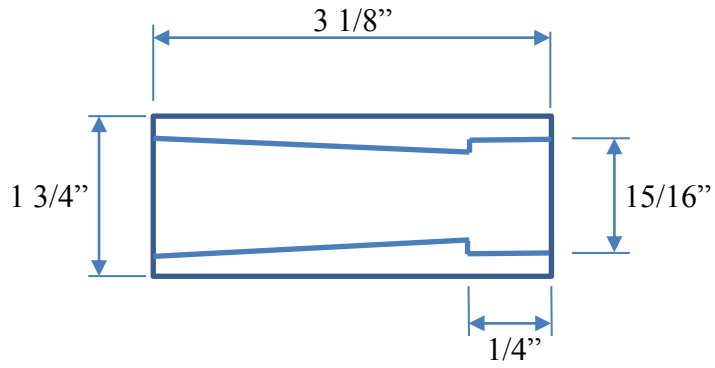

Figure 2.13 Modified chuck dimensions.

The modified chuck was welded to a 3” x 2 ½” x ¾” steel plate with a circular opening of diameter of 15/16” shown in Fig. 2.14.

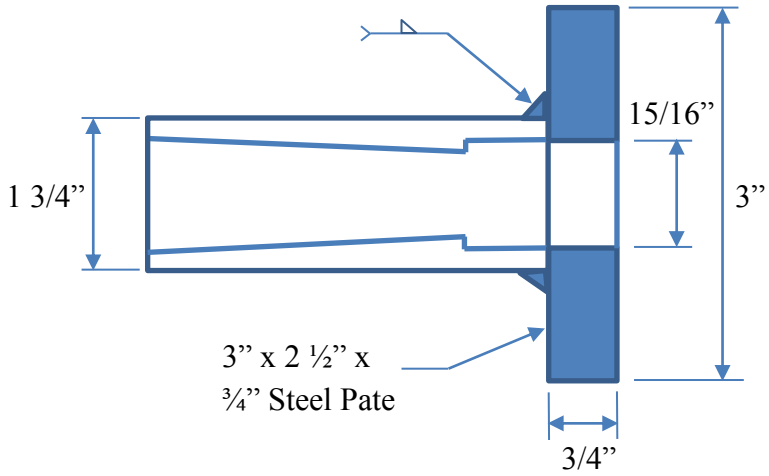

Figure 2.14 Modified chuck assembly.

In the process of prototyping, it was noted that the 2 ½" x 3" bearing plate conflicted with the corner ducts during installation. Based upon the study of dimensions of ducts and strand spacing, a special bearing plate was designed and is shown in Fig.2.15. This special shaped-plate could fit various strand configurations.

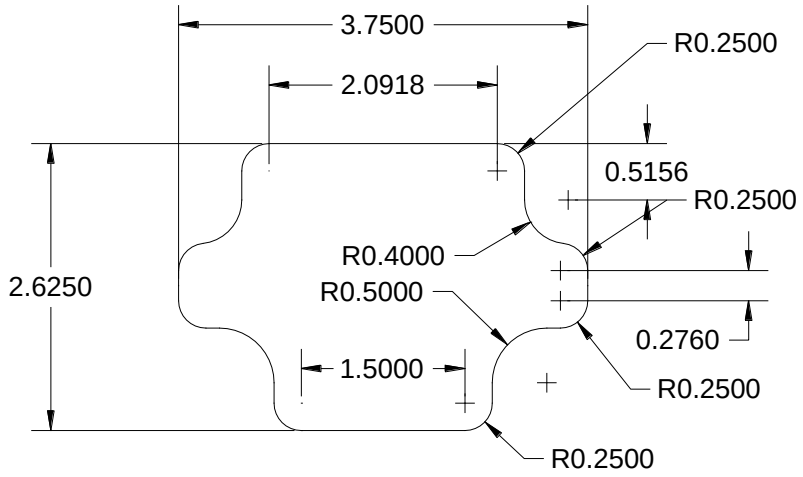

Figure 2.15 Dimensions of special bearing plate (unit: in.).

The finished plate is shown in Fig.2.16.

Figure 2.16 Photo of special bearing plate.

The smooth chamfer at the corner can not only fit the adjacent circular duct and strand, but also avoid stress concentration. Since large concentrated forces are applied to the anchorages, attention was paid to ensure there was no localized concrete failure. A finite element model was established to evaluate the stress acting on the bearing plate. This special shaped plate was modeled using ANSYS as shown in Fig.2.17.

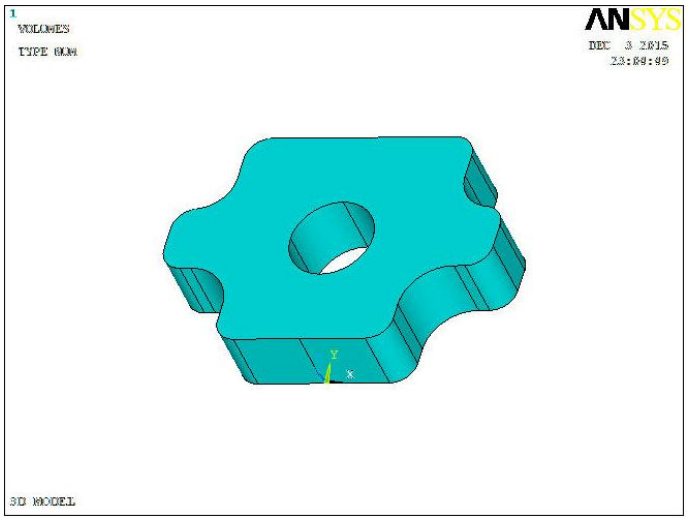

Figure 2.17 3D model of special bearing plate.

The chuck welded on bearing plate is modeled in Fig.2.18.

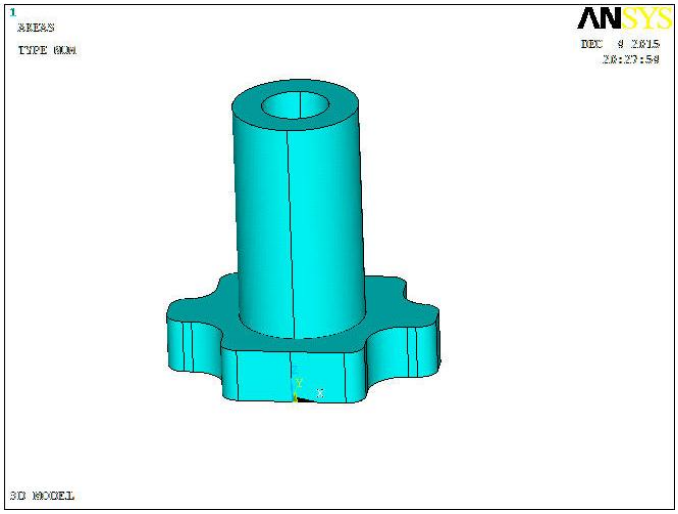

Figure 2.18 3D model of chuck assembly.

To ensure accuracy, a high order 10-node tetrahedral SOLID92 element was utilized in the analysis. SOLID92 has a quadratic displacement behavior at each node. This element is shown in Fig.2.19.

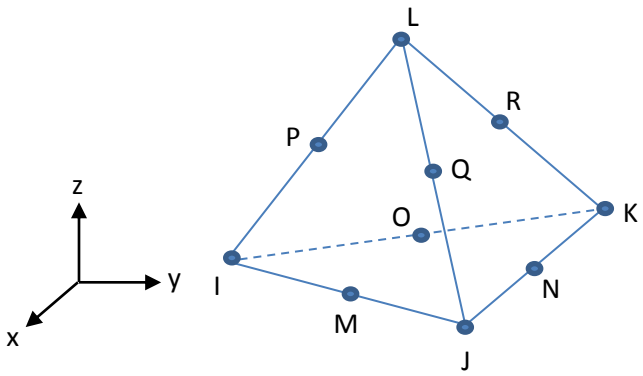

Figure 2.19 High order 10-node tetrahedral SOLID92 element.

The finished mesh is shown in Fig.2.20.

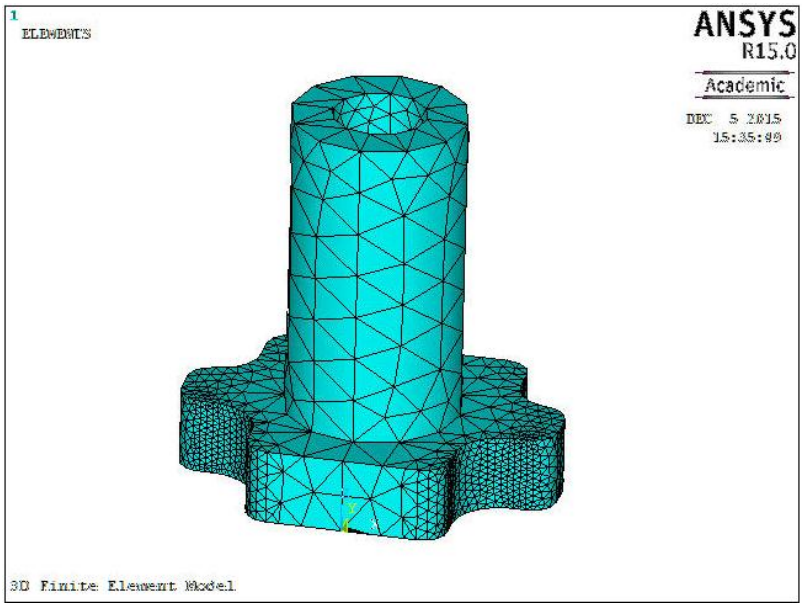

Figure 2.20 Finite element model of chuck assembly.

For locations where the stress gradient was large, the mesh was made finer while at other locations the mesh could be made coarser to save modeling and computation time.

Then the modeled chuck and plate were attached to concrete as shown in Fig.2.21.

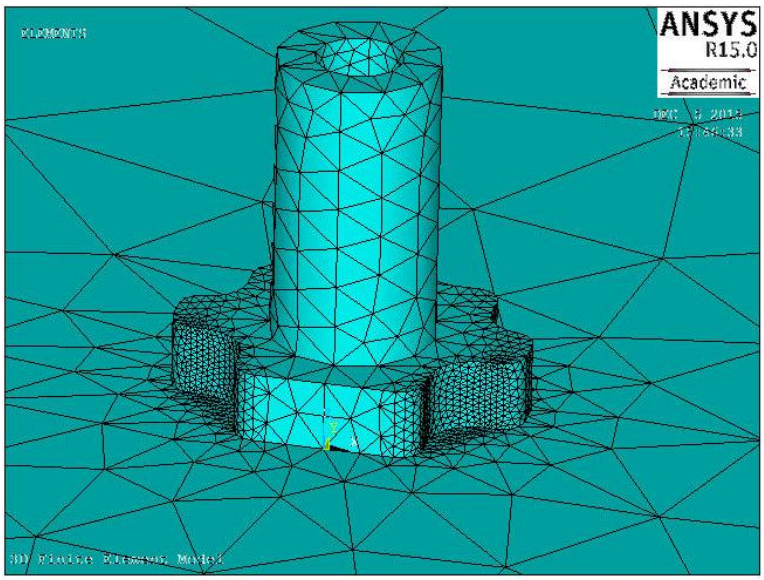

Figure 2.21 Finite element model of chuck assembly on concrete.

The obtained contact stress distribution is shown in the Fig.2.22.

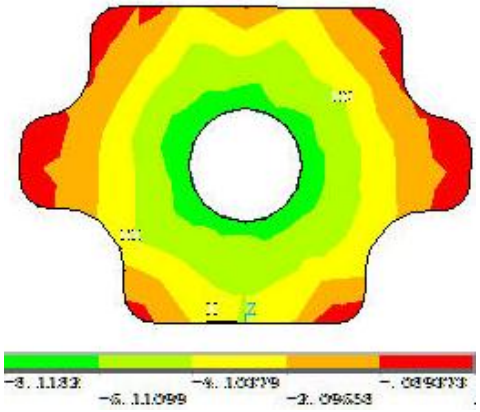

Figure 2.22 Contact stress contour of plate.

The results showed that a ½ in. thick special-sized plate produced a contact stress of up to 8.1 ksi. Although it would not cause local concrete to crush, the effect of localized stress can be mitigated using confinement steel coils around the post-tensioning ducts.

2.8 Splicing Components

To ensure that the locally higher stresses did not affect pile capacity, confinement coils can be used to increase local concrete strength (Leet and Bernal, 1997). The diameter of the coil used was 3/16 in. and the pitch of the coil was 1 ½ in. The height of the coil was 9 in. and the confinement diameter was 2 ½ in., which was designed to fit the bearing plate dimensions. The pitch of the coils was set to permit adequate concrete flow since the typical aggregate size is ¾". The finished confinement coils welded on special bearing plate is shown in Fig. 2.23.

Figure 2.23 Confinement coils welded on special bearing plate.

The strands were required to be bonded for fully developing the splice strands after concrete cracking. The ducts were grouted by pumping the grout into the grouting manifold as shown in Fig.2.24.

Figure 2.24 Grouting manifold.

In order to ensure bond between the grouted strand and the surrounding concrete, the ducts were deformed by creating indentations at spacing intervals of 2 in. as shown in Fig.2.25.

Figure 2.25 Deformed ducts.

To evaluate the efficiency of the splicing system, a series of flexural testing were conducted at the Structural Laboratory that is presented in Chapter 3.

CHAPTER 3: LABORATORY SPLICED PILE STUDIES

3.1 Introduction

To study the flexural behavior of post-tensioning spliced piles, a series of tests were conducted at the Structural Laboratory, University of South Florida. The test specimens include two spliced 14" prestressed concrete piles with each segment 10 ft long and two corresponding control piles with a length of 20 ft.

3.2 Fabrication of Test Specimens

This section describes the strand configuration of the specimens, the design of the prestressing facilities, specimen components fabrication, instrumentation, initial prestress, transfer, and post-tensioned splicing procedures.

3.2.1 Strand Configuration

The strand configuration for the test specimens was based upon FDOT standard specifications. The cross sectional view of the 14 in. x 14 in. test specimen is shown in Fig.3.1.

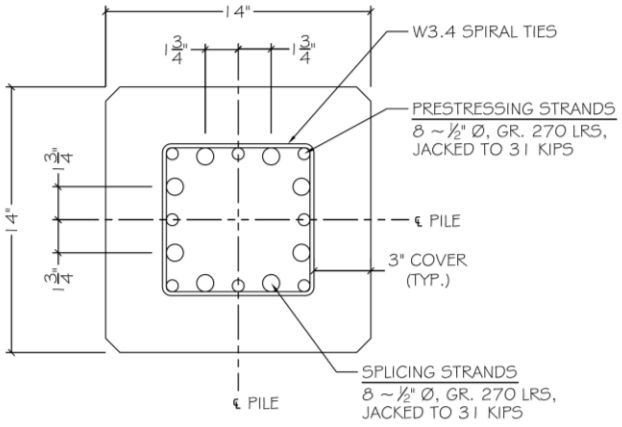

Figure 3.1 Strand configurations of test specimens. (Courtesy Mullins and Sen)

The splicing strands were located within the steel ducts between the prestressing strands,. Grout was pumped into the ducts to provide bond between the strands and ducts. The grout also prevented corrosion of the splicing strands.

3.2.2 Design of Self-Stressing Cast Bed

A self-stressing cast bed was designed to produce the 14-inch prestressed control pile and the two ten feet long 14-inch pile segments that needed to be spliced. The walls of the bed consisted of three 14-inch concrete piles which can carry the loads from the jacking forces and also serve as the formwork for casting the test piles. Seven-foot long steel plates (2.5 inch thick) were used as the end plates of the cast bed. The outdoor bed setup is as shown in Fig.3.2.

Figure 3.2 Casting bed for test piles.

Under the large applied prestressing force, the header plate can bend. Bending in the header plate causes high stresses in the compression struts and result in associated lateral displacements due to the eccentricity of the loads. To reduce or eliminate the lateral displacements of the concrete piles that were used as the form for the concrete casting bed, a lead plate was planned to be used for reducing the eccentric loading effects. However, the uneven

surface of the pile end causes stress concentration, which results in uncontrolled eccentricity during loading.

To solve this problem, the following approach was used: Rockite high strength anchor bolt cement was chosen to be poured between the compression strut and header plate to form a layer with a thickness of ¼" inch. The high strength compound can result in a seamless contact plate. A series of finite element analysis were conducted to locate the optimum offset of the plate from the edge of concrete pile.

Due to the geometric and loading symmetries, the pile cast bed was analyzed using a quarter model to save modeling and computation times. The corresponding boundary conditions were constrained at the symmetric planes. The quarter model was established as shown in Fig.3.3, using ANSYS, a finite element analysis program.

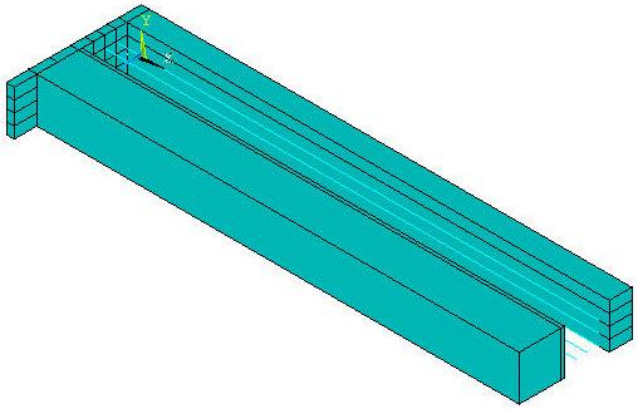

Figure 3.3 Quarter model of cast bed.

The plate was not only subjected to in-plane tension, but also subjected to out-of-plane compression (Timoshenko and Woinowsky 1959). Therefore, an 8-node shell element was used (Fig. 3.4) with element boundary continuity along the interface.

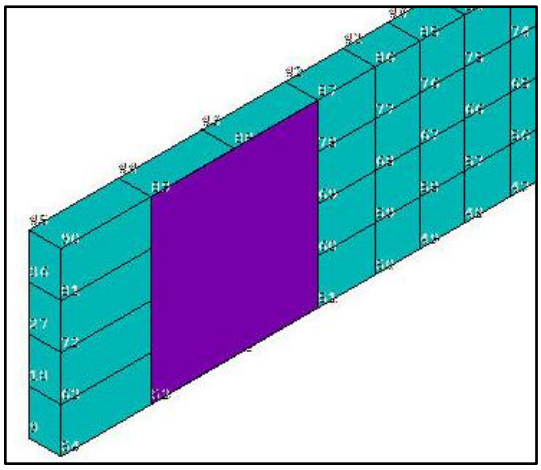

Figure 3.4 Shell element model.

The prestressing load of 31 kips was applied at each strand location. Fig. 3.5 shows the deformed shape of the cast bed.

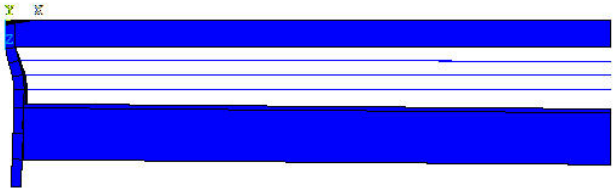

Figure 3.5 Deformed shape of cast bed.

Based on the finite element analysis, a 0.327 inch of outer pile lateral displacement can be expected without making any eccentricity adjustments. A one-inch offset yields a lateral deflection of 0.136 inch; a two-inch offset reduces the lateral deflection to 0.0101 inch, while a three-inch offset causes an inward deflection of -0.0768 inch. Using these findings, the lateral deflection versus lead shim offset is plotted in Figure 3.6.

It can be seen that the optimum offset of the plate is between two inches and three inches crossing the x-axis approximately at 2-1/8 inches. Therefore, a 2-inch offset was used for the cast

bed design. During stressing of the bed, the lateral outward movement was recorded as 0.013 inch for both outer piles, which verified the predictions from the analysis.

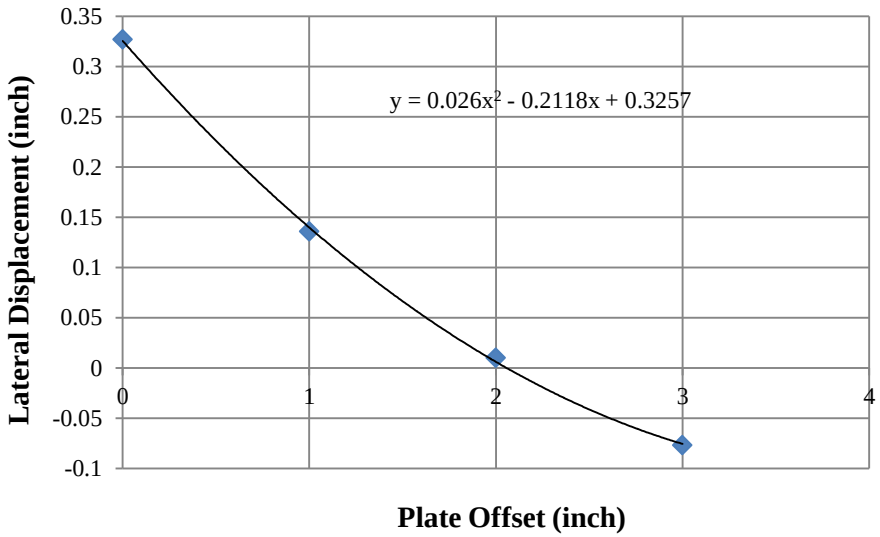

Figure 3.6 Lateral displacement vs plate offset.

3.2.3 Fabrication of Splicing Components

The splicing components include anchorage assemblies, splice header, post-tensioning ducts, confinement coils, grouting manifold, and jacking plate. These splicing components are shown in Fig. 3.7. The anchorages were staggered to introduce uniform pre-compression in the splice zone. In the upper pile segment, the ducts allowed the strands to extend to the pile top. In the lower pile segment, ducts were extended to the grouting manifold, which allowed grout to flow through the ducts. The first series used smooth metal ducts. The second test series used deformed metal ducts, which was achieved by using indentations around the circumference spaced at two inches.

The layout of the splicing system may be seen in Fig. 3.8. By using this layout, the two spliced segments and a control could be cast during each pour, which ensures the same concrete material properties for the spliced piles and the controls.

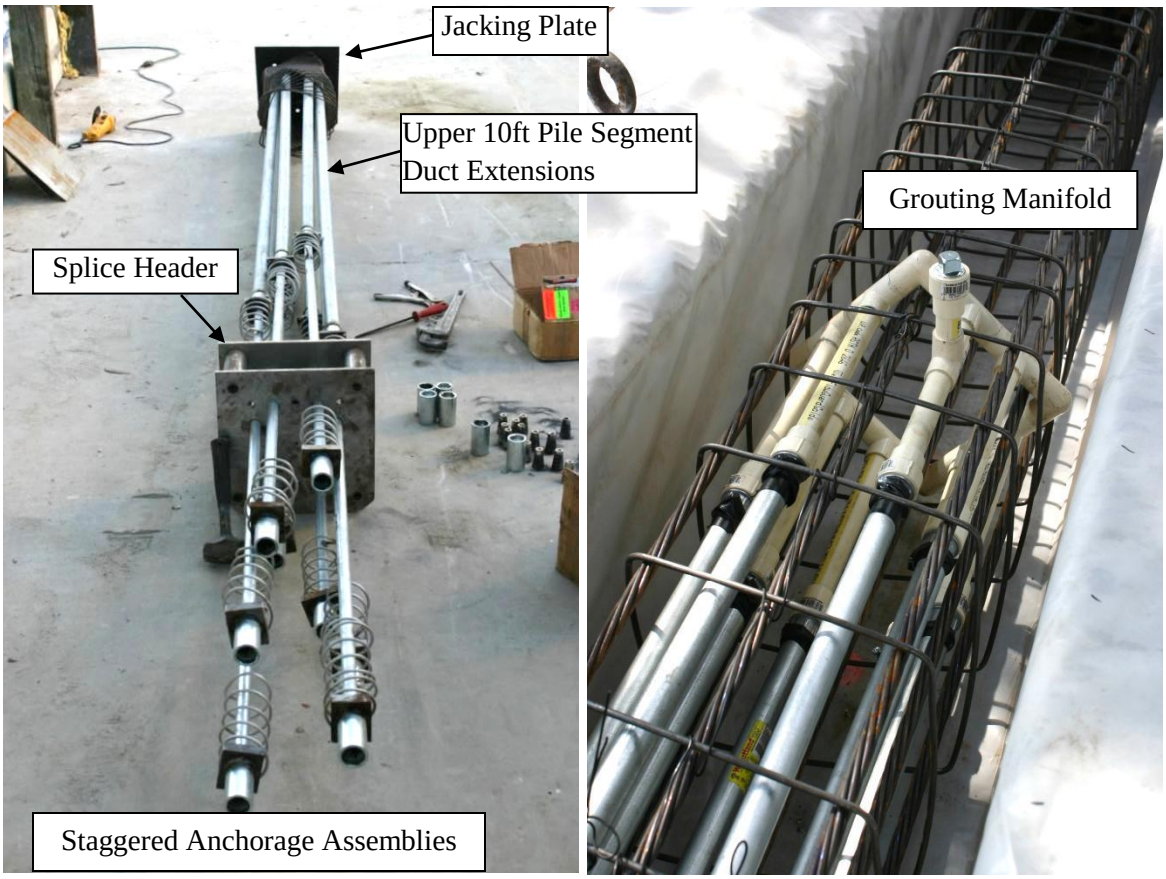

Figure 3.7 Splicing system components.

3.2.4 Cast of Test Pile Specimens

High-strength concrete was used to cast the pile specimens. The concrete supplier was Preferred Materials, Inc., Odessa, Florida. Based upon 4" x 8" cylinder tests, the concrete compressive strengths for the two series of tests are listed in Table 3.1.

Table 3.1 Concrete compressive strengths

Series	Concrete Age (days)	Concrete Compressive Strength f'_c (psi)		
		Cylinder 1	Cylinder 2	Average
Test Series 1	3	6344	6448	6396
	14	7874	7706	7790
	91	9324	9431	9377
Test Series 2	3	5672	6000	5836
	10	7644	7754	7699
	56	9064	9143	9104

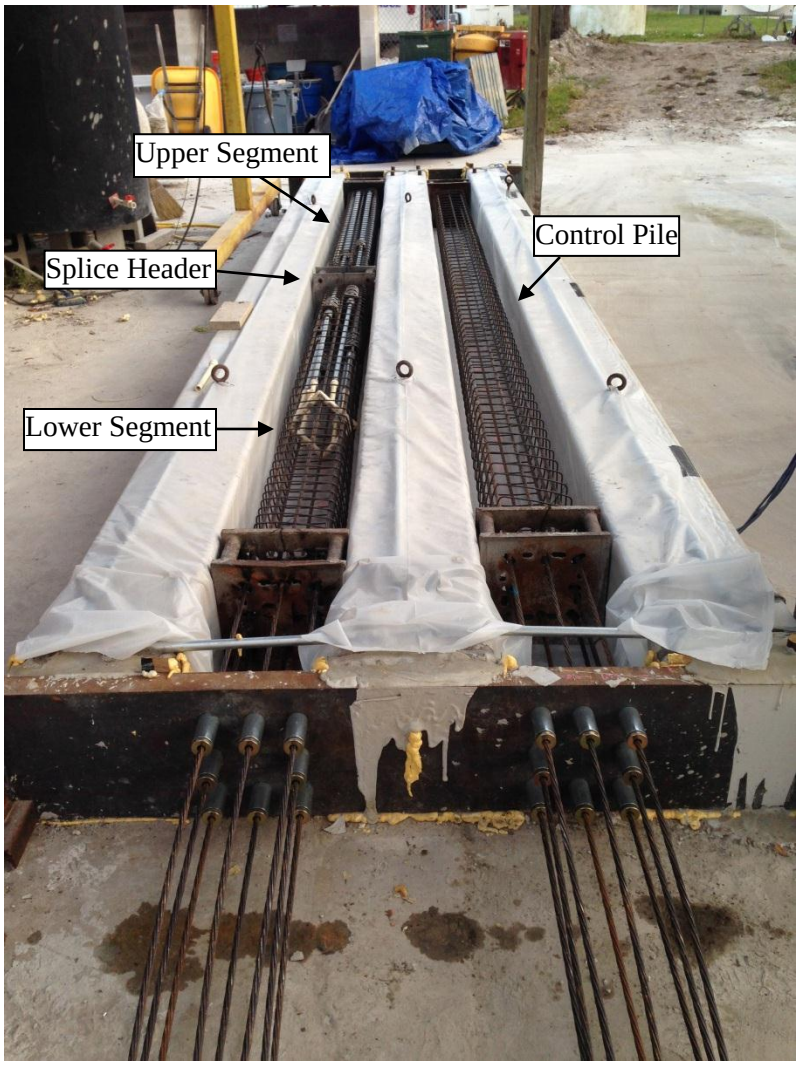

Figure 3.8 Layout of splicing system in the fully stressed bed.

3.2.5 Transfer Length Monitoring

After concrete was poured and cured in the forms for three days, the strands were detensioned to transfer the pre-compression loads to the concrete. To monitor transfer lengths, a series of strain gages were mounted on the concrete surface of the pile specimens at 10 in. spacing to coincide with the midpoint between anchorages. Fig. 3.9 shows the recorded strain results. It was found that the transfer lengths were in the range of $50d_b$~$70d_b$, i.e., 25 in. to 35 in. The anchorage location of 40 in. used covers this transfer length.

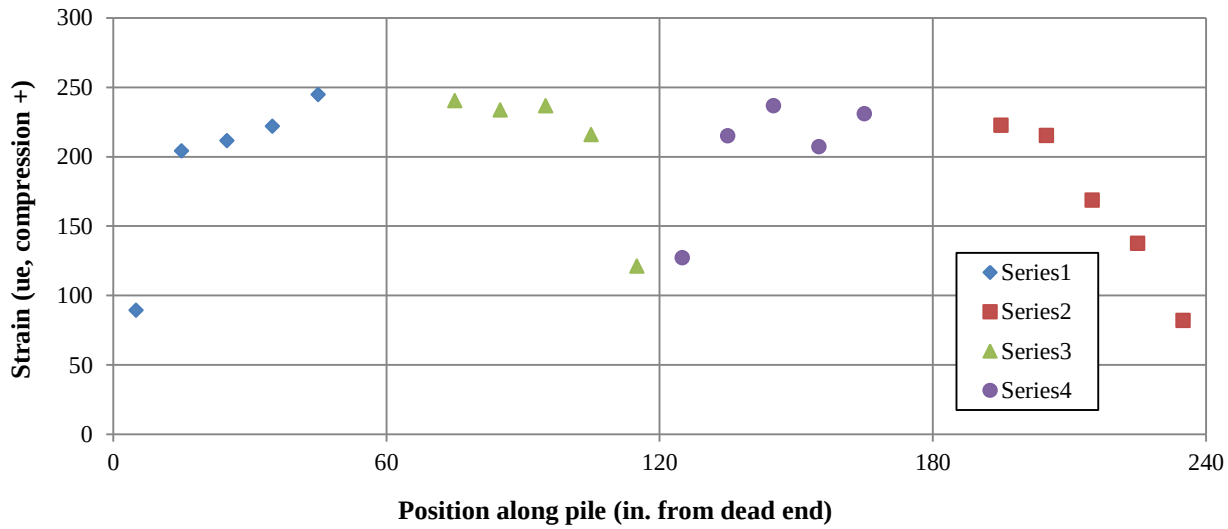

Figure 3.9 Strain variations at the time of detensioning. (Courtesy Mullins and Sen)

3.2.6 Splicing Test Specimens

Before splicing procedures, quality control steps were taken to ensure the quality of the test specimens. First, all ducts were inspected using a borescope with a 360-degree articulating viewing head as shown in Fig.3.10.

Figure 3.10 Inspection of ducts using borescope.

If any debris was found, e.g. steel filings at the grouting duct connectivity, the debris was blown out using compressed air.

The second quality control step was to ensure that the strands could be pushed through embedded chucks by measuring the movement of the spring actuated wedges. For the bottom pile, the movement was confirmed as 3/8 in. For the upper pile, the movement was confirmed as 1/4 in. because the upper pile wedges were equipped with two 0.06 in. shims to reduce anchor set losses.

The strands were then threaded into the upper pile segment. When pushing the strands into the lower segment, the strands were clamped to prevent further movement into the upper segment. Splicing was conducted on splicing rails made of steel angles. The lower segment was supported by an overhead crane and pushed by a forklift. When all the strands were inserted into the anchorages, epoxy was applied onto the two contact surfaces. The overhead crane was used to ensure correct splicing by adjusting the alignment.

3.2.7 Post-Tensioning the Splice

The post-tensioning order is shown in Fig.3.11.

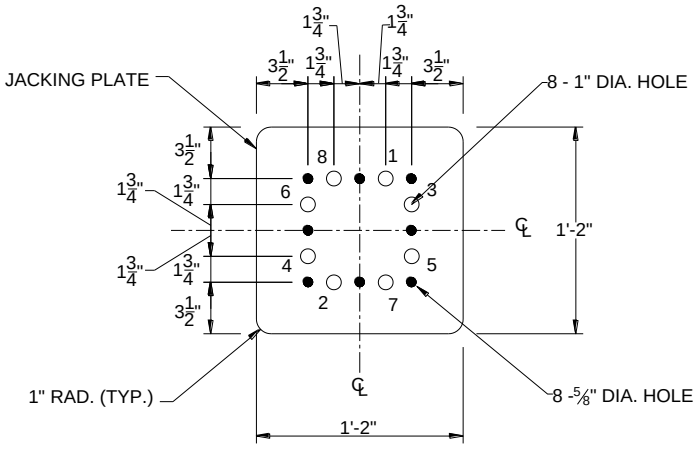

Figure 3.11 Post-tensioning order on jacking plate.

The pairs of post-tensioning strands with the same anchorage locations were jacked simultaneously. To reduce losses from elastic compression of concrete, jacking procedures were conducted in stages. More stages can result in a more uniform pre-compression in concrete, but it affects field efficiency. The following table shows the forces in the first stressed strand in the three-stage jacking procedures.

Table 3.2 Forces in the first stressed strand in three-stage jacking

Force in the first stressed strand (kips)			
Strand Loaded	Stage 1	Stage 2	Stage 3
1	7.00	18.50	26.50
2	6.94	18.45	26.46
3	6.88	18.40	26.43
4	6.82	18.35	26.39
5	6.76	18.30	26.36
6	6.70	18.24	26.32
7	6.64	18.19	26.29
8	6.58	18.14	26.25

At the conclusion of the splicing procedure, the computed stress distributions based upon strain gage measurements are shown in the Fig.3.12.

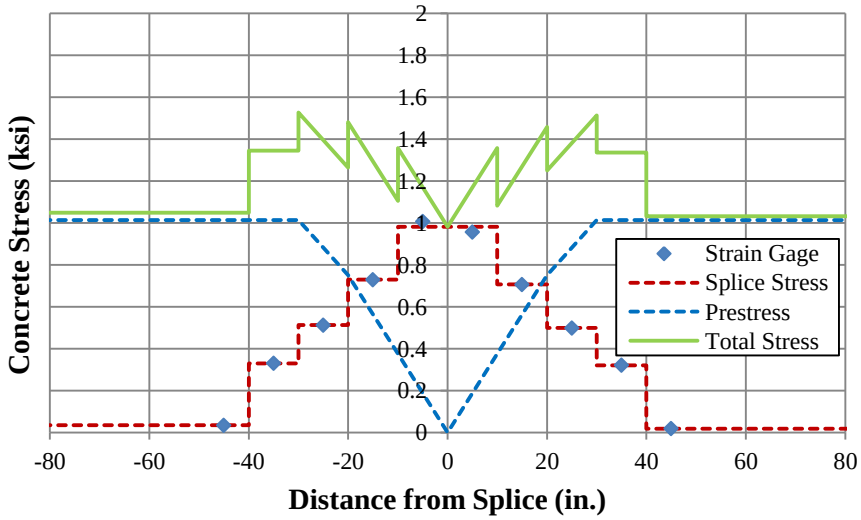

Figure 3.12 Stress distributions in the splicing procedures.

It may be seen that the staggered layouts of the dually embedded anchorages resulted in a gradual superimposition of stresses. The stress induced at the interface was close to the target 1000 psi according to FDOT specifications. There was no sudden stress jump due to the stagger layouts and therefore, the excessive pre-compressive stress was avoided in the splice zone by using this new technique.

3.3 Flexural Test Setup and Procedures

The flexural test was conducted at the Structural Laboratory of University of South Florida. The load configuration was a four-point bending test. The dimensions of the experimental setup were shown in Fig.3.13.

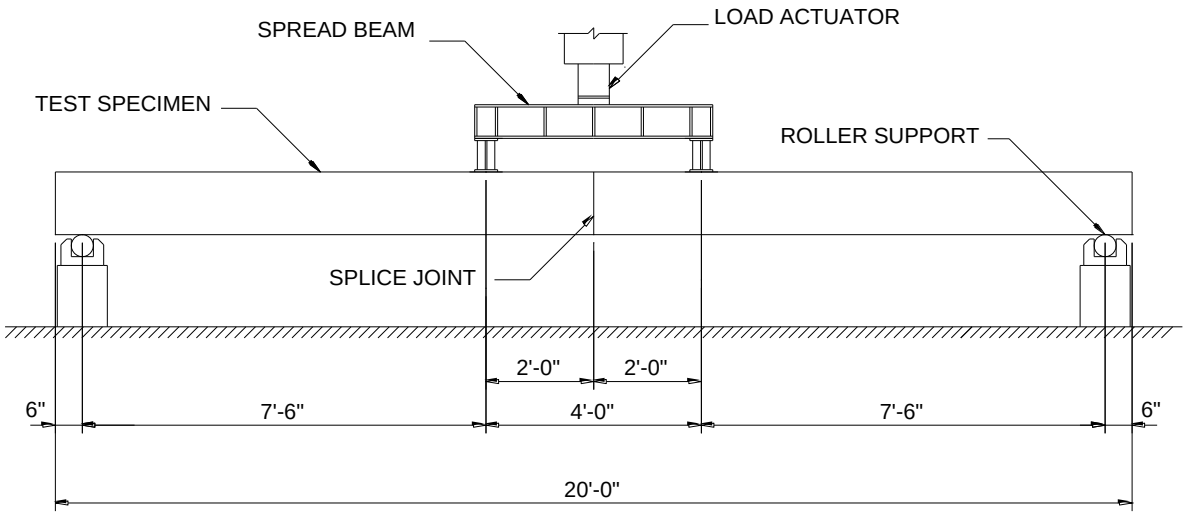

Figure 3.13 Dimensions of the flexural experiment.

The flexural test was conducted by applying loadings on a spread beam which included three I-shape steel beams. The specimen was supported on two roller supports at each end. The positions of the supports were carefully adjusted to ensure correct alignment.

To measure deflections along the test specimens, three LVDTs were placed at the quarter point and midspan of the pile. The spacing of LVDTs was shown in Fig.3.14.

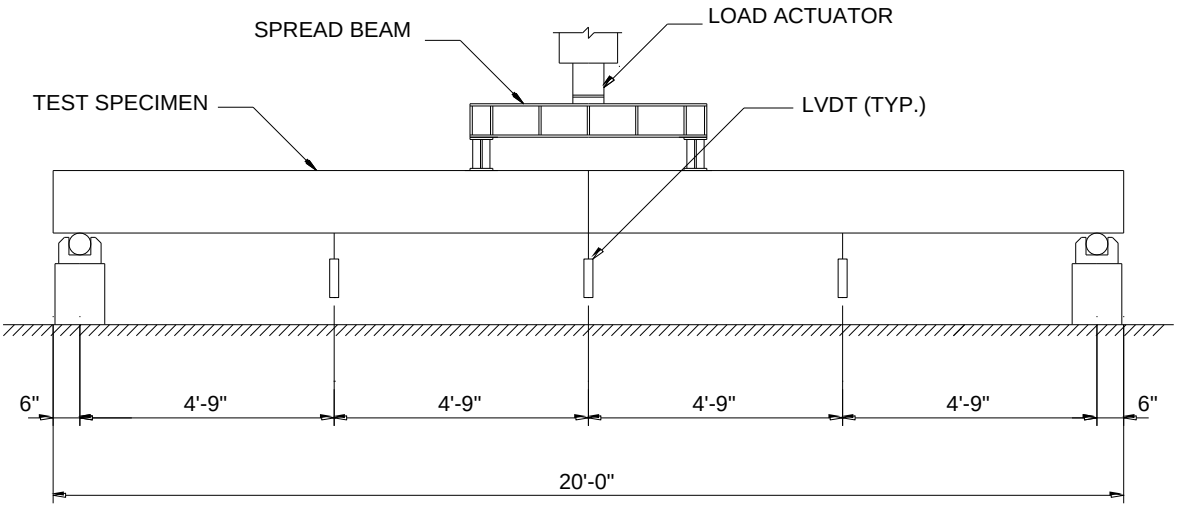

Figure 3.14 Instrumentation of LVDTs.

The finished experimental setup is shown in Fig.3.15.

Figure 3.15 Finished experimental setup.

The Applied load from the load actuator was split into two loads 2 ft off the midspan. Loads were applied incrementally through an actuator until failure occurred. Test data were recorded via a high resolution computerized data acquisition system for further analysis.

3.4 Experimental Results

The measured cracking loads and failure loads are listed in Table 3.3. The performance of the spliced piles was similar to that of controls. Higher stiffness was observed for the test series two which was cast with deformed ducts.

Table 3.3 Cracking and failure loads of test specimens

Event	Test 1		Test 2	
	Control	Splice	Control	Splice
Cracking Load (kips)	16.5	14.6	16.8	15.0
Failure Load (kips)	39.2	32.8	39.4	36.0
Ultimate Deflection at Midspan (in.)	3.42	1.99	3.54	1.92

The observed ultimate stages for the test specimens are shown in the Fig. 3.16 ~ 3.19.

Figure 3.16 Ultimate stage of control 1.

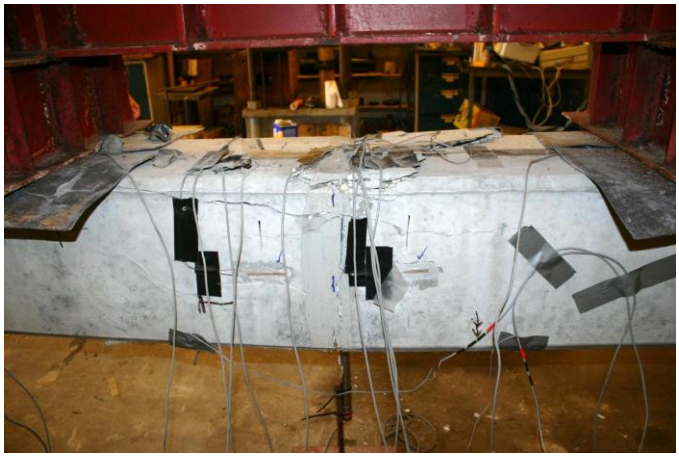

Figure 3.17 Ultimate stage of splice 1.

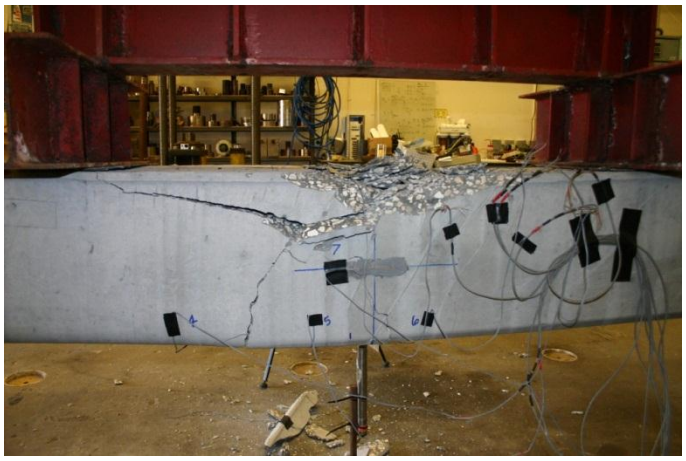

Figure 3.18 Ultimate stage of control 2.

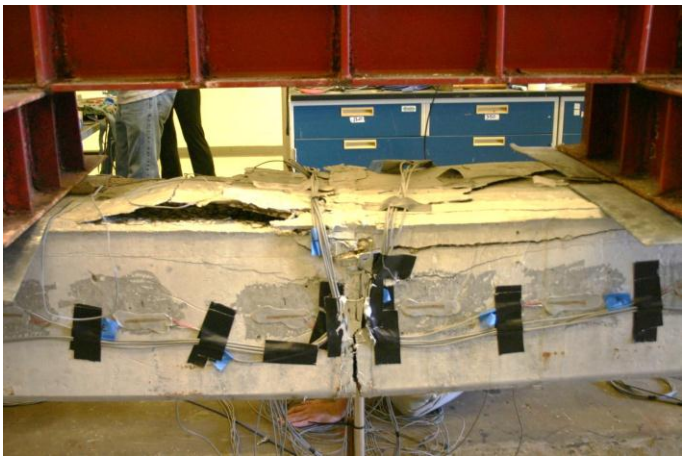

Figure 3.19 Ultimate stage of splice 2.

It may be seen that for control specimens, flexural tensile cracks developed from the bottom and concrete crushed in the top compression zone. The compression block extended below the spiral level and several vertical tensile cracks developed in the constant moment zone. The test specimens displayed large permanent deformations. Failure in the spliced piles started in the compression zone after joint separation occurred in the tension region at the splice. Crack was confined to the splice interface. The compression block crushed within a small localized area above the spiral ties. After the load was released, the spliced piles rebounded almost fully, resulting in very small permanent deformation.

The load versus mid-span deflection plots for the test specimens are shown in Fig. 3.20 ~ 3.21. It can be seen that the response of the spliced piles was similar to that of the control specimens until ultimate. However, permanent deformation in the spliced piles was small compared to that of the control specimens. The stiffness of the spliced 2 specimen (Fig 3.21) was higher than the other pile, which was attributed to better bond of the deformed ducts with concrete.

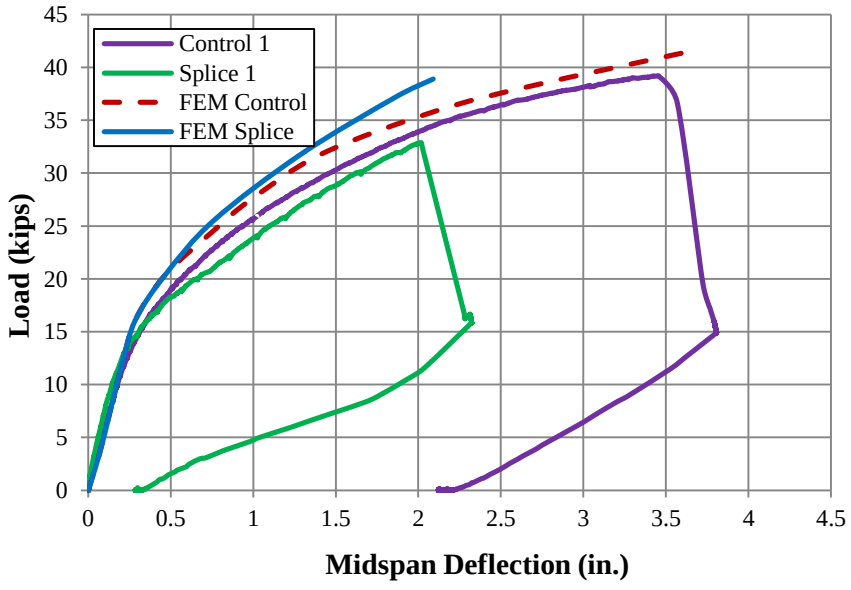

Figure 3.20 Load vs mid-span deflection for test series 1.

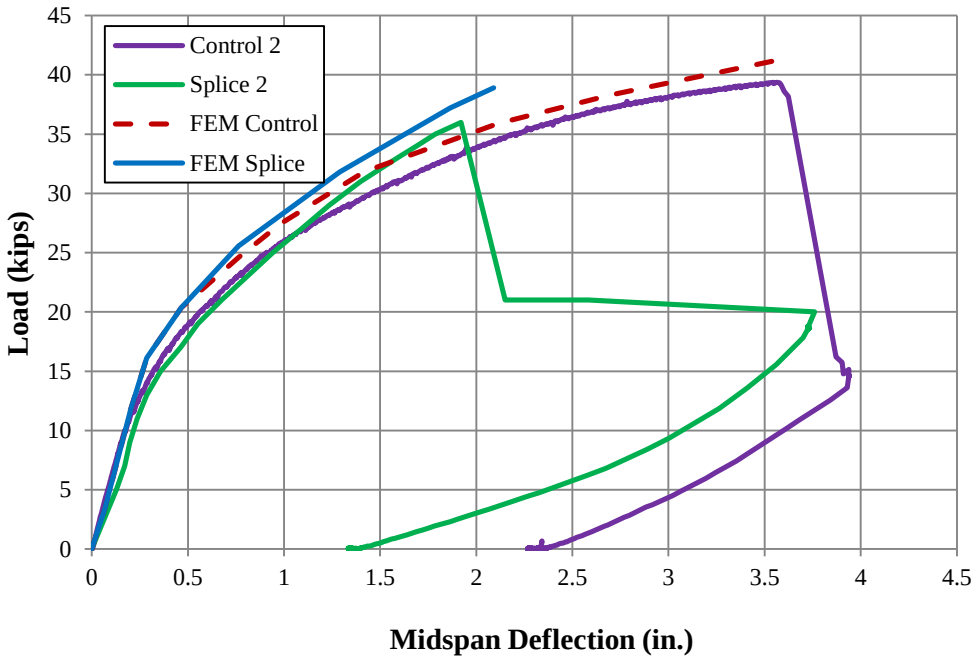

Figure 3.21 Load vs midspan deflection for test series 2.

3.5 Finite Element Analysis

Finite element analysis was conducted to better understand how the structural response of spliced pile differed from that of the control. Although finite element method is widely used for the analysis of concrete structures (Kang, 1977, Scordelis, 1984), realistic finite element modeling still remains one of the difficult challenges in understanding the nonlinear behavior of reinforced and prestressed concrete structures (Zienkiewicz, 2000, Hughes, 2000).

Effective use of commercial finite element software can help solve the complex problems in Civil Engineering. ANSYS was developed in 1970 in Pennsylvania, USA. After decades of improvement, it has become one of the top-listed software for finite element analysis. ANSYS can be used in personal computers or large mainframe computers.

Most importantly, ANSYS has a large collection of elements, some specially designed for solving complex problems. In this study, ANSYS was used because of its powerful modeling capacity of concrete and its computational versatility.

3.5.1 Concrete Constitutive Model

Several constitutive models of concrete have been proposed to date (Kupfer 1969, Chen 1976). Among them, the modified Hognestad concrete model has been successfully used (MacGregor, 1997). This model is given by Eq. 3.1.

$$f_c = f_c'\left[\frac{2\varepsilon_c}{\varepsilon_0} - \left(\frac{\varepsilon_c}{\varepsilon_0}\right)^2\right] \qquad (3.1)$$

In Eq. 3.1, f_c is the concrete stress; ε_c is concrete strain; fc' is the ultimate compressive strength of concrete; and ε_0 is given by Eq. 3.2.

$$\varepsilon_0 = \frac{1.8 f_c'}{E_c} \qquad (3.2)$$

In Eq. 3.2, E_c is the tangent elastic modulus of concrete. The modified Hognestad concrete model is shown in Fig.3.22.

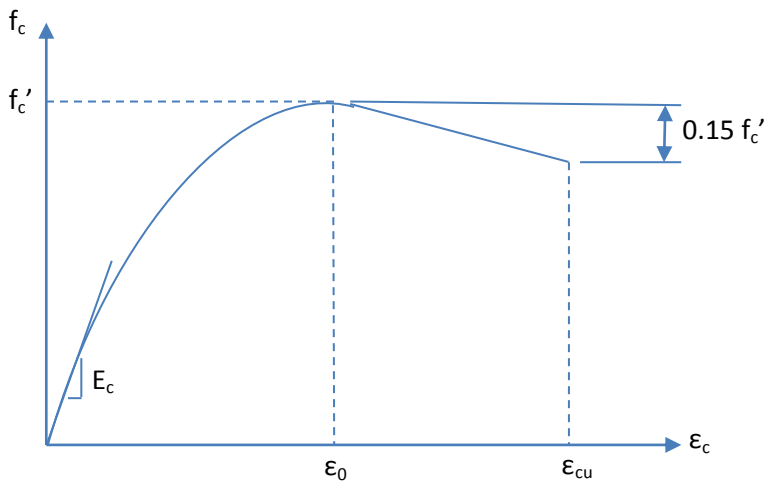

Figure 3.22 Modified Hognestad model.

The above model was incorporated into ANSYS as shown in Fig. 3.23 for the following nonlinear finite element analysis.

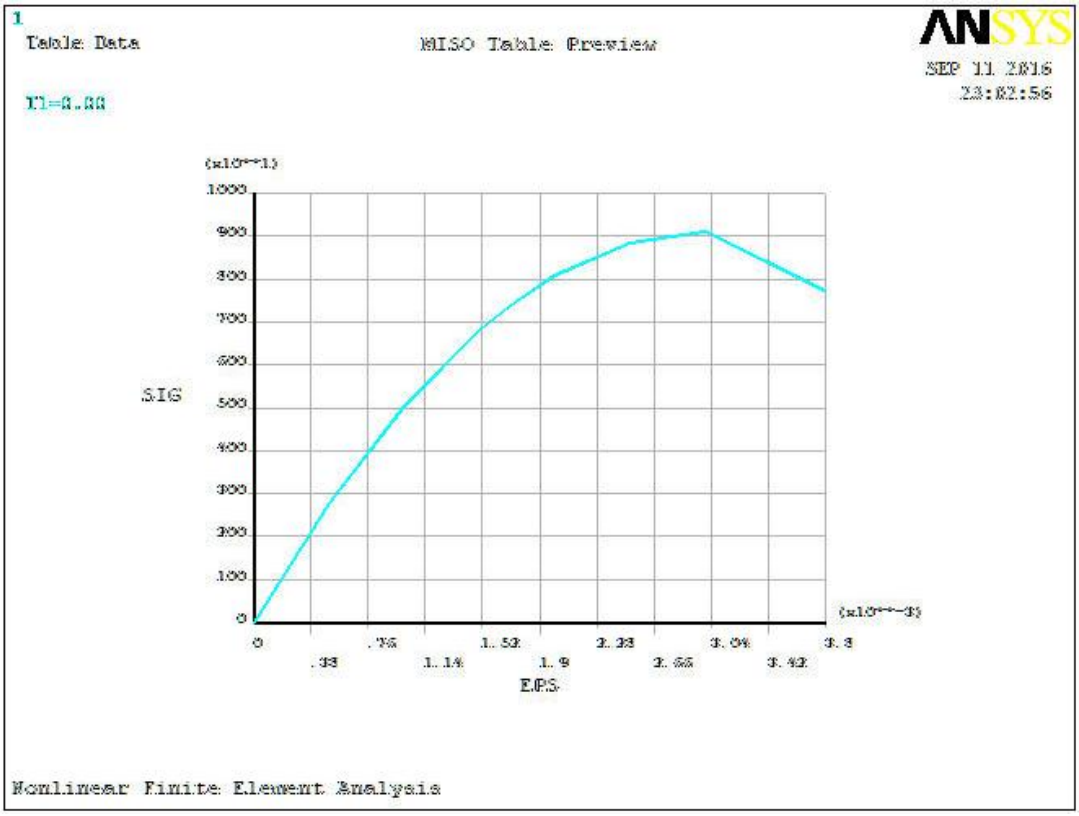

Figure 3.23 Concrete model used in finite element analysis.

3.5.2 Concrete Cracking Simulation

To model concrete cracking behavior, Lin and Scordelis (1975) presented a shear transfer coefficient to improve the representation of concrete cracking in finite element analysis of concrete structures.

The shear transfer coefficient incorporates the effect of dowel action of reinforcement across a crack and the aggregate interlock action along the crack interface. Shear transfer coefficient is typically given as a range. The incremental constitutive relationship of a cracked concrete element for 2D analysis is given by Eq. 3.3.

$$\begin{Bmatrix} d\sigma_{11} \\ d\sigma_{22} \\ d\tau_{12} \end{Bmatrix} = \frac{1}{1-\nu^2}\begin{bmatrix} 0 & 0 & 0 \\ 0 & E & 0 \\ 0 & 0 & \beta(1-\nu^2)G \end{bmatrix} \cdot \begin{Bmatrix} d\varepsilon_{11} \\ d\varepsilon_{22} \\ d\gamma_{12} \end{Bmatrix} \qquad (3.3)$$

In Eq. 3.3, σ and ε are stress and strain; τ and γ are shear stress and shear strain; $\boldsymbol{\nu}$ is the Poisson's ration; E is the Young's modulus; G is the shear modulus; and β is the shear transfer coefficient, which reduces the shear modulus G in Eq.3.3.

Accurate assessment of the shear transfer coefficient is complex and several studies have been conducted, e.g. Gilbert and Warner (1978) used a β value of 0.6 for the analysis of reinforced concrete slab; Hand, Pecknold, and Schnobrich (1973) used a β value of 0.4 for the analysis of reinforced concrete plates and shells.

For 3D analysis, ANSYS (2013) provides two separate shear transfer coefficients: open crack shear transfer coefficient β_t is applied to consider the shear transfer of opening concrete cracks and closed crack shear transfer coefficient βc is applied to consider the shear transfer of closed concrete cracks.

These shear transfer coefficients range from 0.0 to 1.0, where 0.0 refers to very smooth cracks with zero shear transfer; 1.0 refers to very rough cracks so that there is no loss of shear transfer.

For cracked concrete element with open cracks, the magnitude of the transferred normal stress across the crack is reduced. There is sliding and shear along the crack. Shear transfer capacity becomes less. The stiffness matrix $[D_{ck}]$ of the cracked concrete element with open crack is given in Eq. 3.4.

$$\left(D_{ck}\right) := \frac{E}{1+\nu}\begin{bmatrix} \frac{R_t\cdot(1+\nu)}{E} & 0 & 0 & 0 & 0 & 0 \\ 0 & \frac{1}{1-\nu} & \frac{\nu}{1-\nu} & 0 & 0 & 0 \\ 0 & \frac{\nu}{1-\nu} & \frac{1}{1-\nu} & 0 & 0 & 0 \\ 0 & 0 & 0 & \frac{\beta_t}{2} & 0 & 0 \\ 0 & 0 & 0 & 0 & \frac{1}{2} & 0 \\ 0 & 0 & 0 & 0 & 0 & \frac{\beta_t}{2} \end{bmatrix} \quad (3.4)$$

In Eq. 3.4, R_t is the concrete strain softening rate; E is the Young's Modulus; $\boldsymbol{\nu}$ is the Poisson's ration; β_t is the shear transfer coefficient for an open crack.

For cracked concrete element with closed cracks, it is assumed that the normal stress can be transferred across the crack. The shear transfer capacity is reduced. The stiffness matrix $[D_{ck}]$ of the cracked concrete element with closed crack is given in Eq.3.5.

$$\left(D_{ck}\right) := \frac{E}{(1+\nu)\cdot(1-2\cdot\nu)}\begin{bmatrix} 1-\nu & \nu & \nu & 0 & 0 & 0 \\ \nu & 1-\nu & \nu & 0 & 0 & 0 \\ \nu & \nu & 1-\nu & 0 & 0 & 0 \\ 0 & 0 & 0 & \beta_c\cdot\frac{(1-2\cdot\nu)}{2} & 0 & 0 \\ 0 & 0 & 0 & 0 & \frac{1-2\cdot\nu}{2} & 0 \\ 0 & 0 & 0 & 0 & 0 & \beta_c\cdot\frac{(1-2\cdot\nu)}{2} \end{bmatrix} \quad (3.5)$$

In the finite element model, the open crack shear transfer coefficient β_t was specified as 0.5 and the closed crack shear transfer coefficient βc was specified as 0.95 based upon several

test runs that were conducted to determine the coefficients until there was a good agreement between numerical and experimental results.

3.5.3 Smeared Crack Model for Concrete Element

Since concrete cracking is a major parameter for material nonlinearity, modeling of concrete cracking affects the accurate simulation of nonlinear response of concrete structures. In finite element analysis, concrete cracking modeling is a complex task since the propagation of concrete cracks requires redefinition of the mesh topology. This increases computational time without improving accuracy because the crack orientation can only follow the mesh topology. To solve this problem, a smeared crack model is used in ANSYS. This model assumes that the concrete cracks spread within a concrete element (smeared). Using a continuum approach, the local displacement discontinuities at cracks are distributed within the cracked concrete element. In a smeared model, the concrete element cracks at the integration points as shown in Fig.3.24.

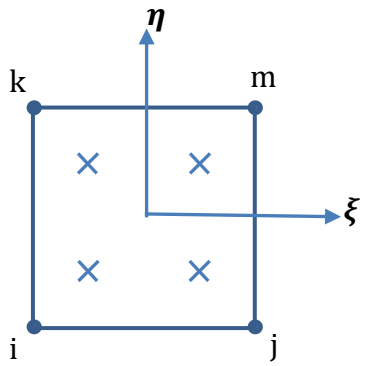

Figure 3.24 Integration points for Gaussian quadrature.

The element stiffness matrix $[k]^e$ relates nodal loads to nodal displacement. $[k]^e$ is computed in natural coordinates given by Eq. 3.6.

$$[k]^e = \iint_{-1}^{1} [B]^T [D_{ck}][B] t|J| \, d\xi \, d\eta \qquad (3.6)$$

where [B] is the matrix of shape function; $[D_{ck}]$ is given in Eq. 3.4 and 3.5; t is the thickness of the element; |J| is the determinate of the Jacobian matrix, which is given in Eq. 3.7.

$$[J] = \begin{bmatrix} \frac{\partial x}{\partial \xi} & \frac{\partial y}{\partial \xi} \\ \frac{\partial x}{\partial \eta} & \frac{\partial y}{\partial \eta} \end{bmatrix} \qquad (3.7)$$

Instead of direct integration, computer software utilizes a numerical method which is easy for programming. ANSYS uses Gaussian quadrature as the numerical integration method given by Eq. 3.8.

$$[k]^e = \sum_i \sum_j W_i \, W_j \; [B]^T [D_{ck}][B] t|J| \qquad (3.8)$$

In Eq.3.8, W_i and W_j are the applied weight factors of i^{th} and j^{th} integration points. Once the computed principal stress at an integration point exceeds the concrete tensile strength, concrete cracks as shown by the dotted lines in Fig. 3.25.

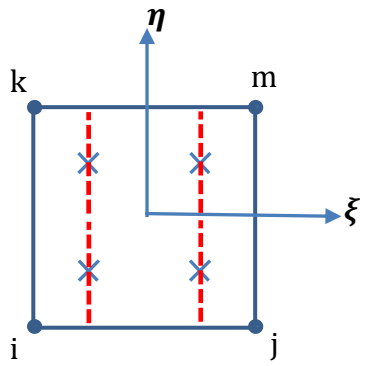

Figure 3.25 Smeared cracks in concrete element.

Concrete cracks spread over the regions where principal stresses exceed concrete's tensile strength. The smeared crack model allows automatic generation and propagation of cracks. The orientation of concrete cracking is flexible, i.e., cracks can rotate about the integration points.

3.5.4 SOLID65 Concrete Element

ANSYS has a library of different types of elements that can be used for structural modeling. The three-dimensional, eight-node element SOLID65 (Fig.3.26) is a dedicated element to simulate the nonlinear response of concrete.

This element has been used in several studies, e.g., Fanning (2001) used the SOLID65 in nonlinear modeling of reinforced and post-tensioned concrete beams. The flexural responses of the specimens were accurately captured by the established models.

Lu and Jiang (2003) used SOLID65 element in the analysis of reinforced concrete frame structures. The study results showed that, with proper setup, this type of element can simulate concrete behavior accurately.

Si and Sun et al. (2007) used SOLID65 element in an investigation of steel-concrete composite frame. The numerical results were in good agreement with experimental results.

Laith and Hamza (2008) used SOLID65 element to analyze the reinforced concrete beam with embedded prestressed concrete prisms. The concrete element captured the nonlinear behavior of the structural member accurately.

Kim et al. (2010) used SOLID65 element to study the unbounded post-tensioned concrete beams. The analysis results validated the efficiency of this element. Therefore, SOLID65 element was used in this study.

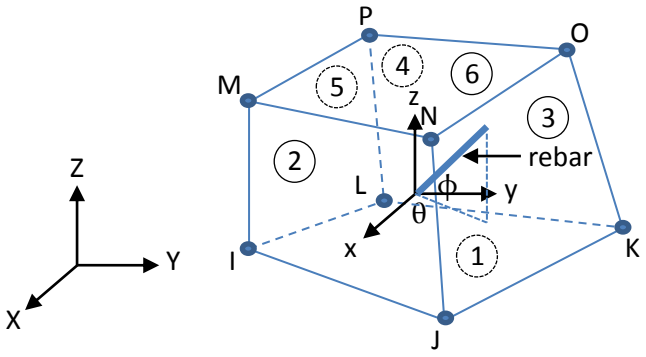

Figure 3.26 Eight-node SOLID65 element.

The SOLID65 element incorporates the smeared crack model in the tension zone and a plastic deformation and crushing model in the compression zone. The smeared model represents cracked concrete with reduced modulus in the direction normal to the cracked concrete plane. Concrete cracks can be generated automatically while maintaining continuity of the nodal displacement field. This element is able to crack in three orthogonal directions, deform plastically, and crush in a tri-axial compression state.

3.5.5 Failure Criterion

ANSYS adopts the William-Warnke failure criterion (1975) for representing the tri-axial behavior of concrete element because this criterion was found to work well for quasi-brittle materials such as concrete (ANSYS 2013). This criterion has been used in several studies, e.g. Fanning (2001), Lu and Jiang (2003).

The William-Warnke criterion for failure of concrete due to multi-axial stress state is given in Eq. 3.9.

$$\frac{F}{f_c'} - S \geq 0 \qquad (3.9)$$

In Eq. 3.9, F is a function of the principal stress state and S is the failure surface expressed in principal stresses and five parameters, f_t, f_c', f_{cb}, f_1, and f_2.

These parameters are defined as the following: f_t is the uniaxial tensile strength; f_c' is the uniaxial compressive strength; f_{cb} is the biaxial compressive strength; f_1 is the compressive strength for a state of biaxial compression superimposed on the hydrostatic stress state σ_h; and f_2 is the compressive strength for a state of uniaxial compression superimposed on the hydrostatic stress state (William and Warnke 1975). In ANSYS, these parameters are defined in Eq. 3.10 to Eq. 3.13.

$$\sigma_h = \frac{1}{3}(\sigma_{xp} + \sigma_{yp} + \sigma_{zp}) \quad (3.10)$$

In Eq. 3.10, σ_{xp}, σ_{yp}, and σ_{zp} are the principal stresses in the principal directions.

$$f'_{cb} = 1.2\, f'_c \quad (3.11)$$

$$f_1 = 1.45\, f'_c \quad (3.12)$$

$$f_2 = 1.725\, f'_c \quad (3.13)$$

The above parameters in the concrete model are set as default in ANSYS. The parameters f_t and f_c' need to be set as input variables.

3.5.6 Prestressing Strand Model

The typical stress-strain relationship of low-relaxation prestressing strand (Nilson 1987) is shown in Fig. 3.27. Compared with ordinary steel reinforcement, prestressing strand has no obvious yield plateau in the stress-strain relationship. Therefore, 0.2% offset method (Nawy 1996) was used to determine the yield strength of prestressing strand.

In finite element analysis, the strands are typically modeled as elasto-plastic material. In this study, the inelastic behavior of strand is simulated as a rate independent strain hardening model given by Eq. 3.14.

$$f_{ps} = E_{ps}\varepsilon_{ps}\left\{0.029 + \frac{0.971}{\left\{1+\left(101.489\varepsilon_{ps}\right)^{9.942}\right\}^{0.101}}\right\} \qquad (3.14)$$

In Eq. 3.14, f_{ps} is the stress in strands under loading; E_{ps} is the modulus of elasticity of strands; and ε_{ps} is the strain in strands under loading conditions. Comparison with experimental results (Fig. 3.28) obtained from uniaxial tension tests proved its validity.

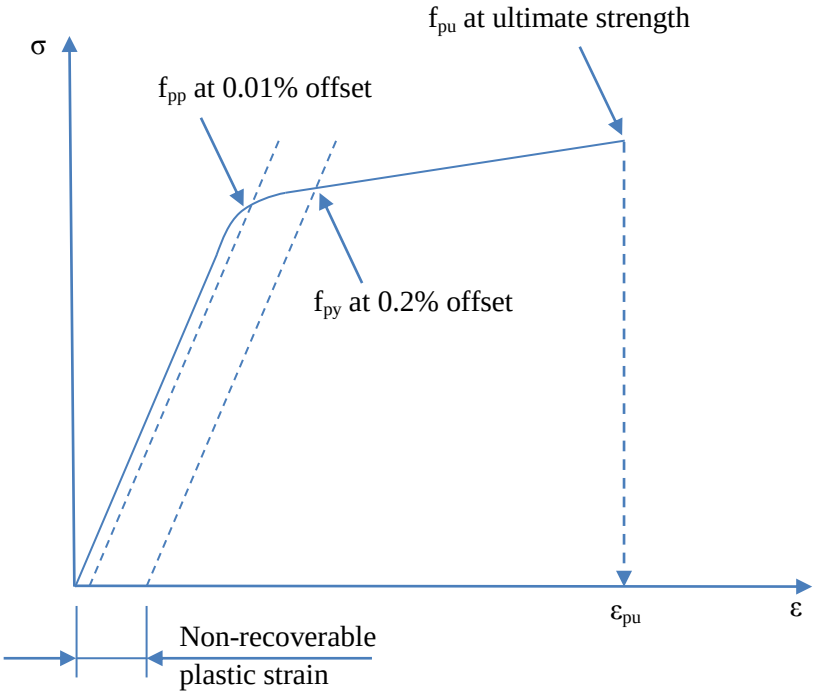

Figure 3.27 Stress-strain relationships for prestressing strands.

It may be seen from Fig. 3.28 that the ANSYS model correlates well with the inelastic behavior of the low-relaxation strands used in the experiments.

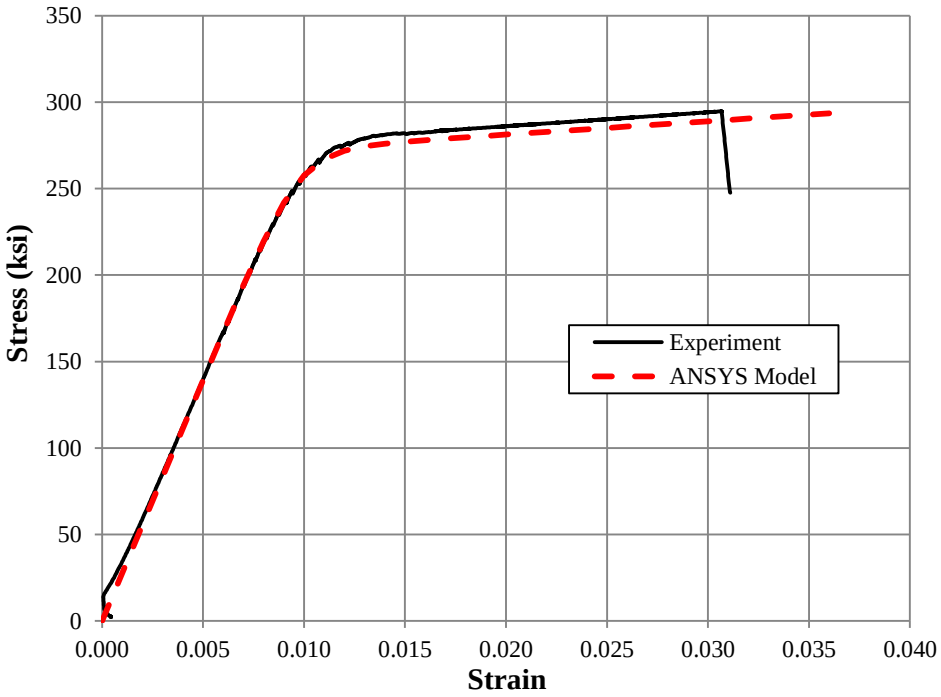

Figure 3.28 Comparison between test results and strain hardening model.

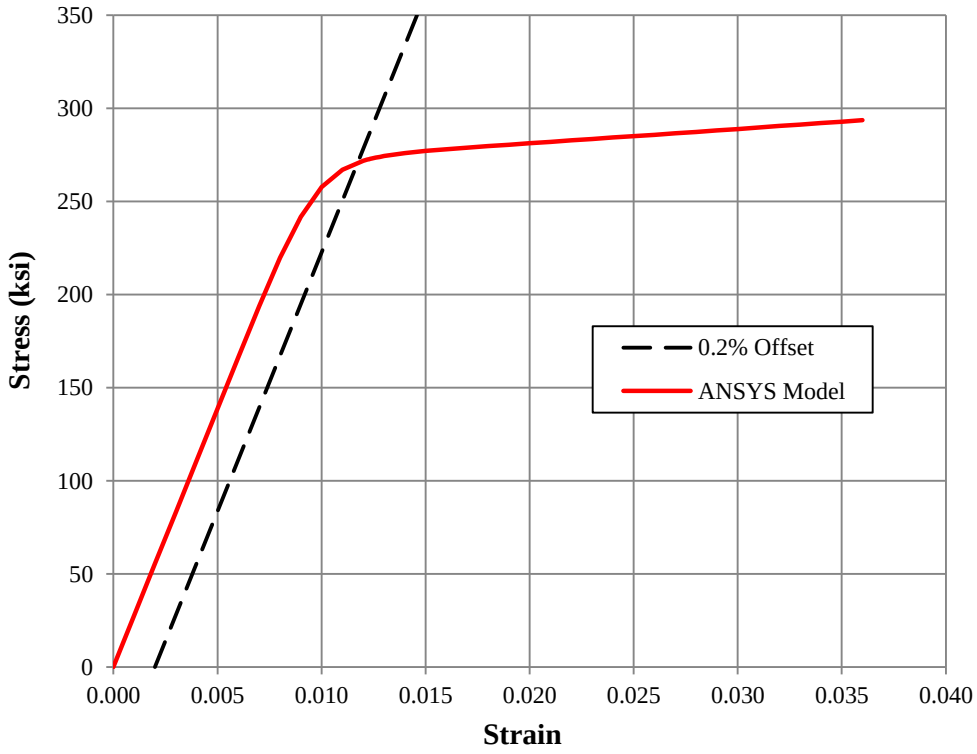

Figure 3.29 0.2% Offset method to determine yield strength of strands.

Based upon Fig.3.29, the yield strength of strand, f_{py}, is determined as 272.85 ksi, which is 92.9% of the ultimate strength, f_{pu}. This finding is consistent with the ACI 318 code (2013) definition of low relaxation strands, where f_{py} is equal to $0.9f_{pu}$.

Since the numbers and locations of the strands were known, the strands were modeled as LINK8 element (Fig.3.30). Each node has three degrees of freedom. LINK8 incorporates strain stiffening and large deflection. This element is a three-dimensional space element and is capable of plastic deformation.

In finite element method, there are three approaches to model prestressing effects: (1) using temperature expansion, (2) applying load on the end of strands, and (3) initial strain method.

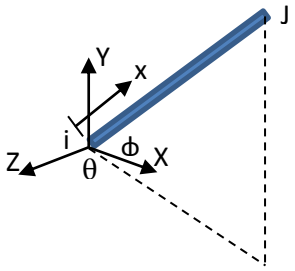

Figure 3.30 Space spar element LINK8.

Temperature expansion method is easy to use but it cannot simulate the actual prestressing procedure. The second method can generate equivalent loads on prestressed members, but the load directions cannot change with the deformation of strands in the prestressed members. The third method applies an initial tensile strain due to prestressing into the strand element before establishing the effective stress and applying compression stress onto

concrete, which is the situation of the actual prestressing procedure (ANSYS 2013). Therefore, this modeling technique was used.

3.5.7 Nonlinear Analysis Procedures

During nonlinear analysis, the Newton-Raphson method was used as illustrated in Fig. 3.31.

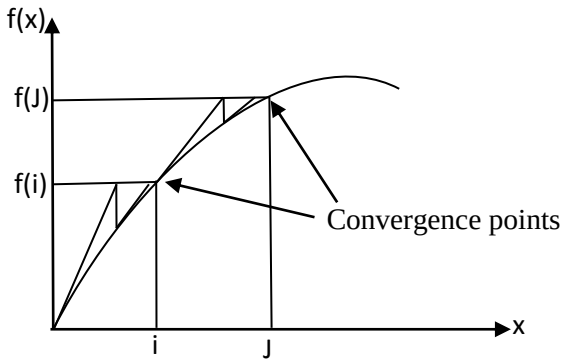

Figure 3.31 Newton-Raphson nonlinear analysis.

This method can be simplified as given in Eq. 3.15.

$$x_{n+1} = x_n - \frac{f(x_n)}{f'(x_n)} \qquad (3.15)$$

In nonlinear finite element analysis, load is applied to the model in load steps. In each iterative step, the unbalanced residual nodal forces $\{R\}_{re}$ are calculated as Eq. 3.16.

$$\{R\}_{re} = \{R\}_{ap} - \{R\}_{eq} \qquad (3.16)$$

In Eq. 3.16, $\{R\}_{ap}$ are applied nodal forces and $\{R\}_{eq}$ are equivalent nodal forces, which can be calculated as Eq. 3.17.

$$\{R\}_{eq} = \sum \int_V [B]^T \{\sigma\} dV \qquad (3.17)$$

In Eq. 3.17, $[B]^T$ is the transpose of the matrix of shape functions. Upon convergence at each load step, the stiffness matrix is adjusted and is input as the start of the next load step until convergence is achieved.

3.5.8 Convergence Criteria

The convergence criteria used were based on force and displacement. After several trials, the tolerance limits were set as 0.5% for force check and 5% for displacement check to obtain convergent solutions. During nonlinear finite element analysis, the automatic time stepping function in ANSYS was turned on to control the size of load steps.

If the convergence was smooth, the load increment was automatically increased until it reached the selected maximum load step size. Otherwise, the load increment was decreased until it reached the selected minimum load step size. The maximum number of iterations was set as 1000 for each load step to ensure convergence.

In the nonlinear analysis procedure, SOLID65 concrete element has an option to include stress relaxation after cracking. When concrete element cracks, stress relaxation allows a gradual reduction of the nodal stress (ANSYS 2013), which can help obtain a converged solution.

3.5.9 Finite Element Modeling Control Specimens

Fig. 3.32 shows the established finite element model for the control specimen. Due to the symmetry of the geometry and loadings, one half of the control pile was modeled.

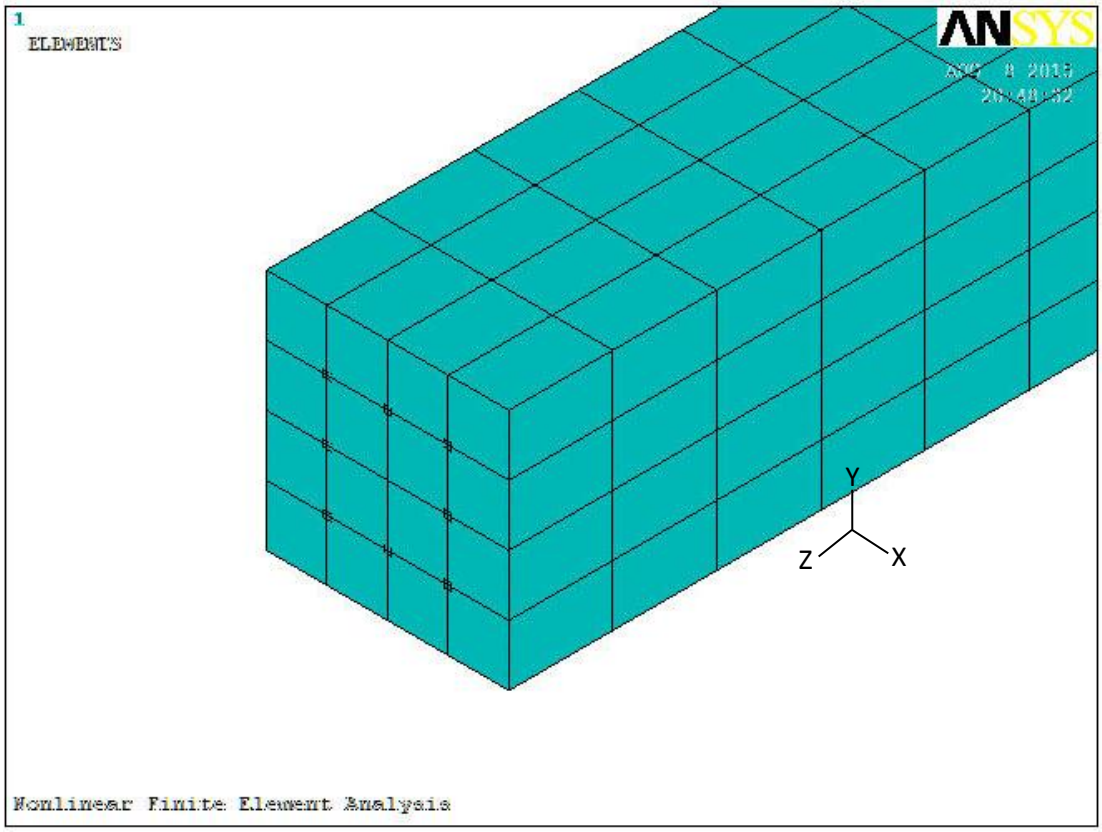

Figure 3.32 Finite element model for control specimen.

Boundary conditions should simulate the actual support conditions and have the correct numbers of degree of freedom. Boundary conditions permit in-plane deflection but restrain the out-of-plane deflections. Thus, at mid-span, the in-plane deflection in y direction was permitted, but the out-of-plane deflections in x and z directions are prohibited.

At the end, the degree of freedom in x and y directions are restrained. The z direction is set free to simulate the roller support in the experiment. The out-of-plane rotations about y and z axis were also restrained. The established boundary conditions are shown in Fig.3.33.

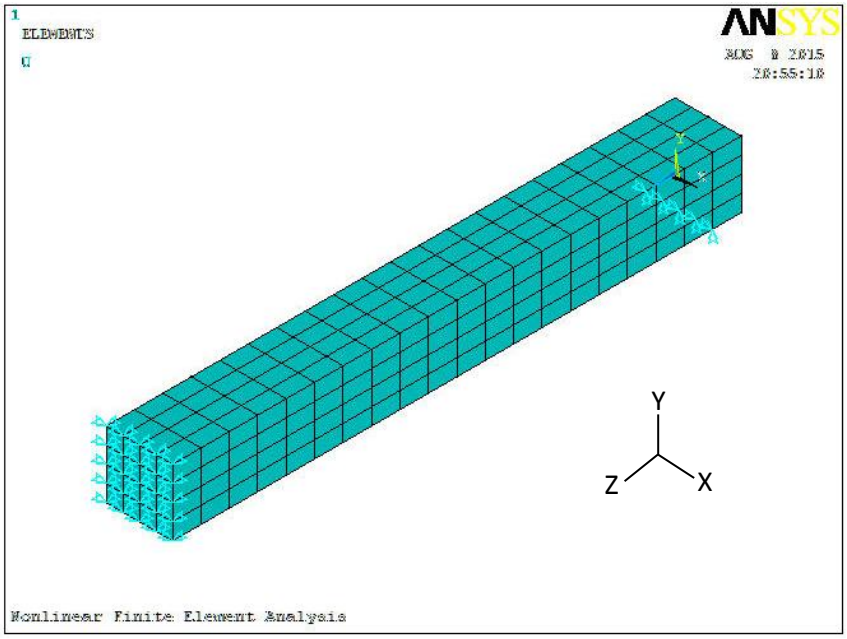

Figure 3.33 Boundary conditions of finite element model.

The deformed shape of the finite element model is shown in Fig.3.34.

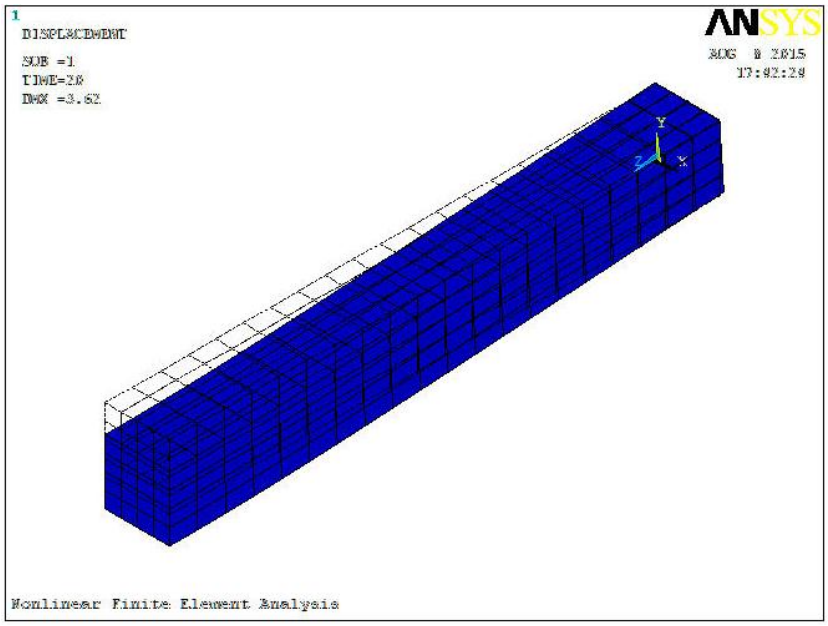

Figure 3.34 Deflected shape of finite element model.

The results obtained for the pile deflection were compared with experimental results as shown in Fig.3.35.

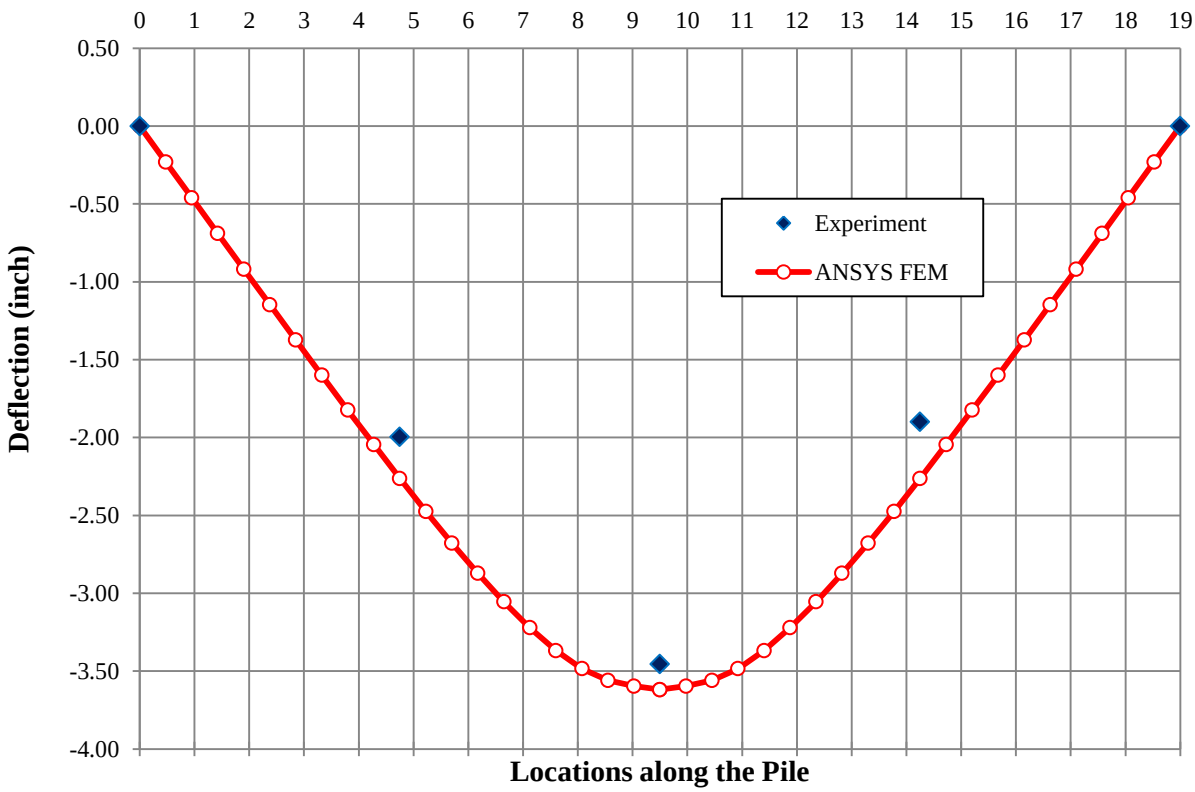

Figure 3.35 Deformation along the pile.

It may be seen that the FEM analysis accurately predicts the deflection response. Comparisons between the predicted and observed load versus mid-span deflection plots are shown in Fig. 3.20 and 3.21. It may be seen that the predictions from the finite element models captured the overall structural response of the test specimens. Fig.3.36 shows the comparison of experimental and predicted cracking patterns at ultimate stage.

The vertical flexural cracks uniformly distributed in the tension zone and the concrete crushed in the top compressive zone. The disagreements are the exact crack locations and crack spacing.

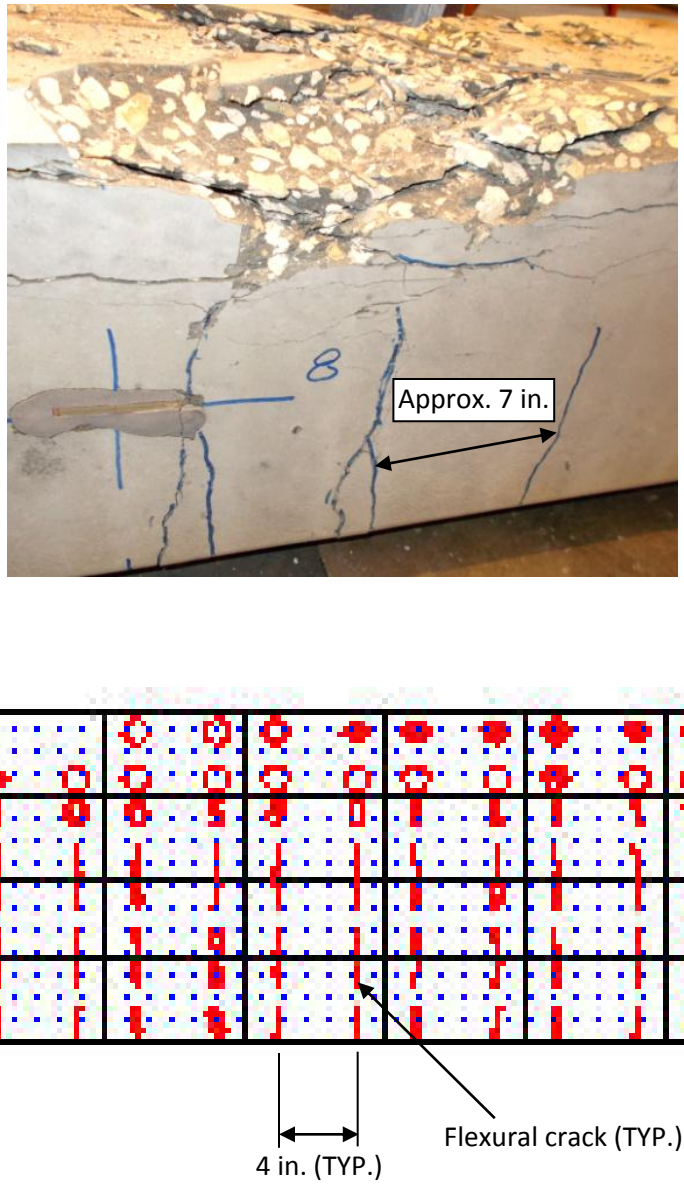

Figure 3.36 Cracking patterns in control, experiment (top) and prediction (bottom).

ANSYS uses a smeared crack model for concrete which generates cracks at the integration points where the computed principal tensile stress exceeds the concrete tensile strength. As a result, there is only general agreement between the predicted and experimental results (Fig. 3.36). Predicted cracks are more closely spaced than the experimental results. The failure modes were generally matched by predictions.

3.5.10 Finite Element Modeling Spliced Specimens

Unlike the control pile, the spliced pile requires modeling of the interface, post-tensioning strands, and ducts. Furthermore, no advantage can be taken of symmetry because of the staggered layout of the post-tensioning strands (Fig. 2.6). The interface was modeled using contact elements; the post-tensioning strands were modeled using LINK8 elements; the ducts were modeled using PIPE20 elements.

The established spliced pile model is shown in Fig.3.37 using the similar procedures as discussed in the prior sections. The simulated full model of spliced pile is shown in Fig. 3.38.

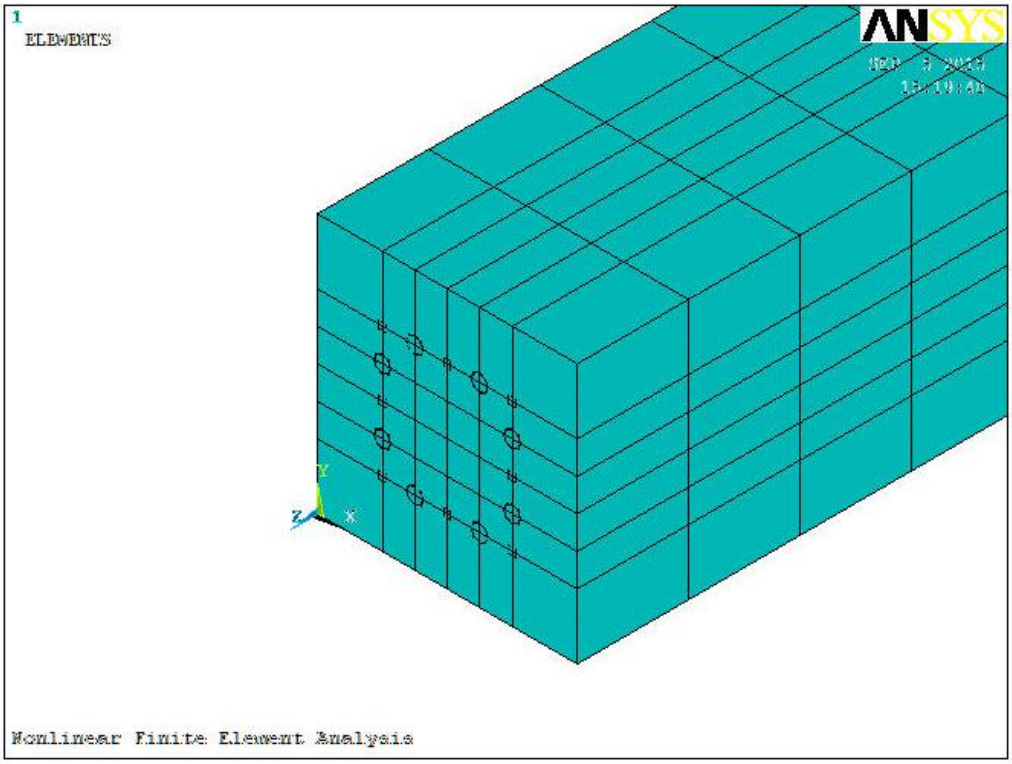

Figure 3.37 Finite element model of post-tensioning strands.

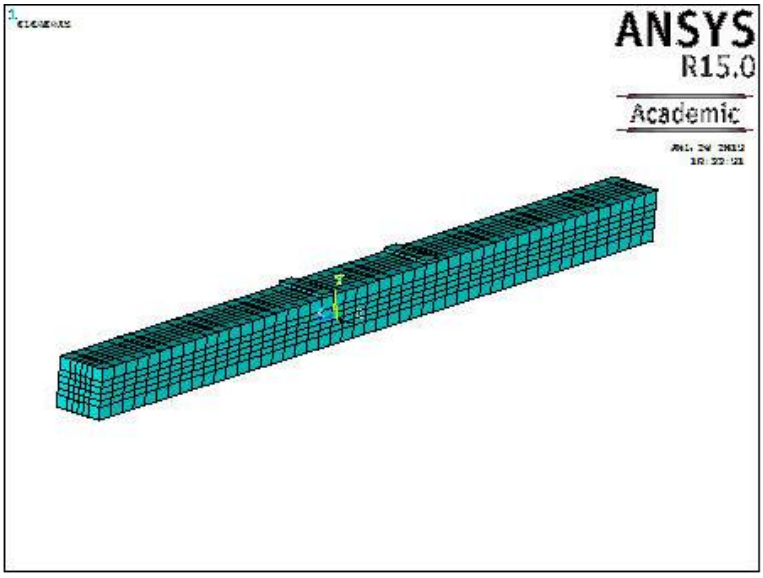

Figure 3.38 Finite element model of spliced pile.

The interface between the two spliced pile segments was modeled by contact elements using TARGE170 elements and CONTA173 elements. The material properties of the interface were based on the tensile bond and elastic modulus of the epoxy as specified by the manufacturer (Appendix B). The generated contact elements are shown in Fig.3.39.

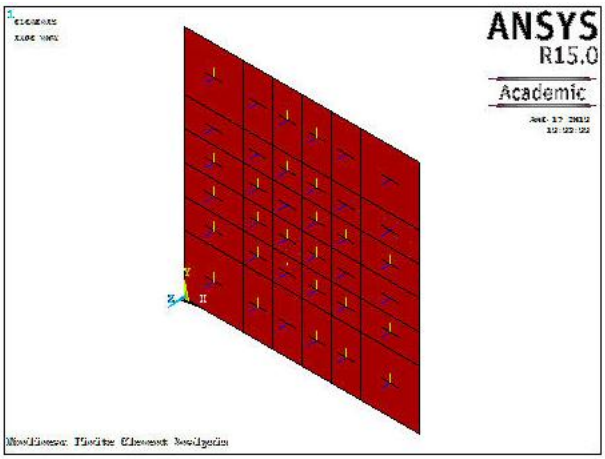

Figure 3.39 Contact elements.

The energy criterion is used in ANSYS to define the mixed-mode debonding at the interface.

$$\frac{\int \sigma_t du_t}{G_{ct}} + \frac{\int \sigma_n du_n}{G_{cn}} = 1 \qquad (3.18)$$

In Eq. 3.18, σ_t is the contact shear stress; u_t is the contact slip; σ_n is the contact normal stress; u_n is the contact gap; G_{ct} is the shear fracture energy; and G_{cn} is the normal fracture energy. ANSYS uses the mixed-mode of shear stress-slip model and normal contact stress-gap model.

According to fracture mechanics, the crack tip has a local yield zone, which can cause crack propagation under continuous loading. In this spliced pile case, the crack propagation can be suppressed when the crack propagates close to the concrete compression zone.

The contact penetration is shown in Fig. 3.40. It can be seen that the bottom portion of interface has lost contact due to joint opening and the compression is localized in the top area, where a plastic hinge is formed. The deformed shape of the finite element model is shown in Fig.3.41.

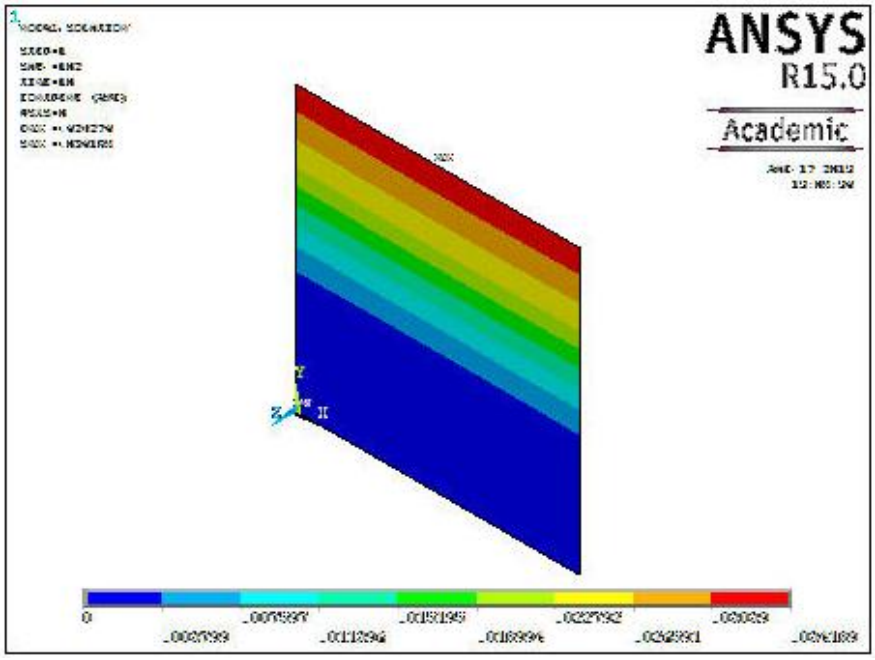

Figure 3.40 Contact penetration of contact elements

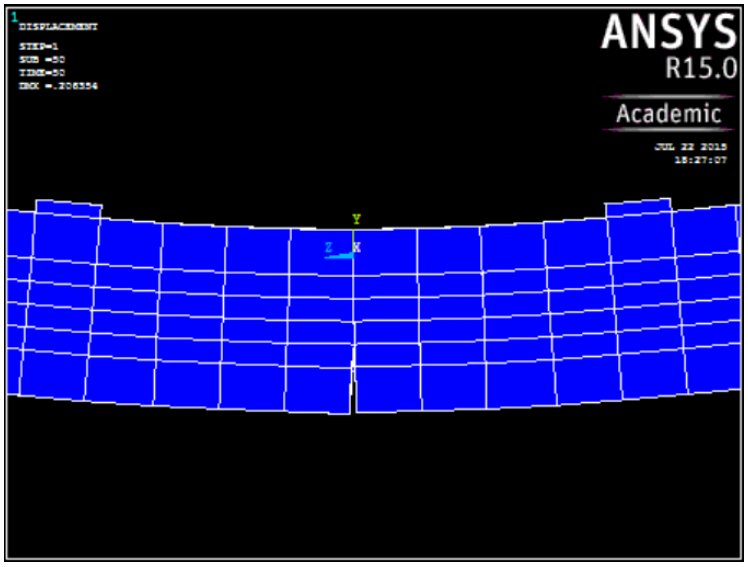

Figure 3.41 Deformed shape of the finite element model.

Comparisons between the predicted and test load versus mid-span deflection relationships are shown in Fig. 3.20 and 3.21. It may be seen that the predictions from the finite element models simulated the overall structural response of the test specimens. Agreement is better for test series 2 using deformed ducts because of the assumption of perfect bond.

Figure 3.42 shows the longitudinal stress variation in the spliced pile before and after cracking. Loads previously carried across the splice were transferred to the pile through the deformations in the ducts. Figure 3.43 shows the variation in longitudinal stress of these piles at ultimate stage. It can be seen that the force transfer in the tensile region is much greater.

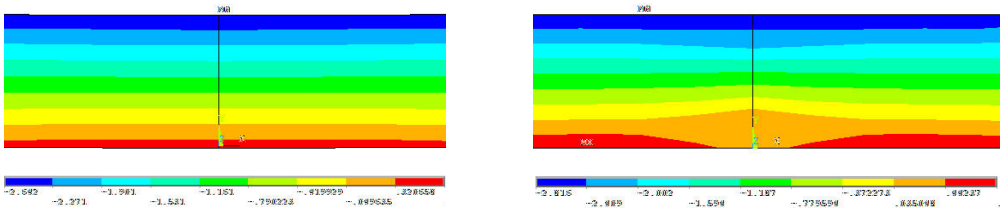

Figure 3.42 Longitudinal stress before (left) and after (right) cracking of spliced pile.

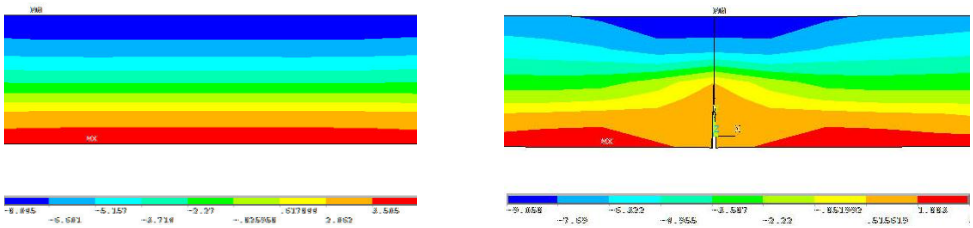

Figure 3.43 Longitudinal stress of control (left) and splice (right) piles at ultimate load.

The model showed the stress distribution in the spliced pile indicated that the concrete in the cover above the splice was crushed. Because this zone is smaller compared to that of the control, the ultimate capacity of the spliced pile was controlled by concrete failure. While it is a constant moment region, it is not a constant stress region due to the changing cross sectional properties across the splice region.

The relationships of load vs variation in the four post-tensioned strand layers are shown in Fig. 3.44. It can be seen that only one layer approached yield with the three others remaining in the elastic range. As a result, when the applied load was released, elastic rebound limited the permanent residual deformation in the pile, which is confirmed in the experiments.

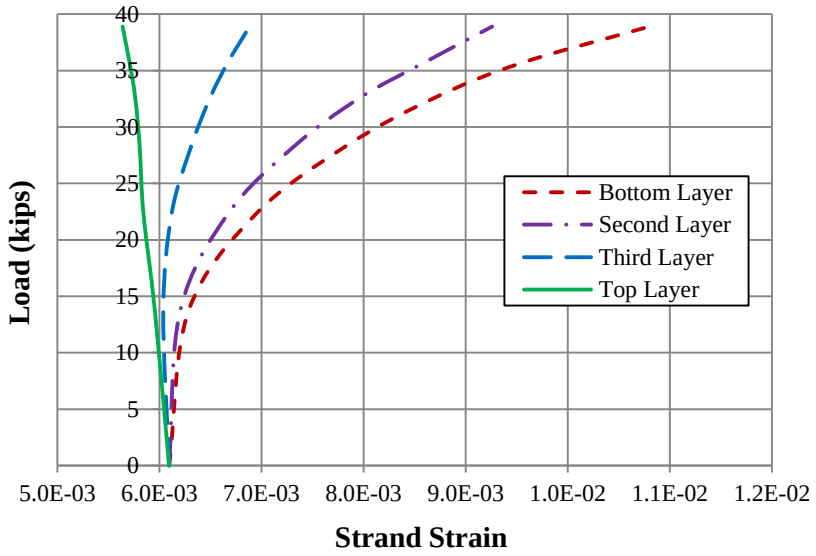

Figure 3.44 Load vs strand strain relationships for post-tensioned strands.

The effect of reduced residual deformation can be beneficial for pile supported structures in seismic zones where ground excitation may induce large secondary moments in piles due to the horizontal movement. These effects will be smaller in the post-tensioned spliced piles.

From this laboratory study, it is proved that the new technique of post-tensioning splice is feasible and efficient. In order to determine its scalability into practical use, a series of full-scale tests were conducted, which are presented in Chapter 4.

CHAPTER 4: FULL-SCALE SPLICED PILE STUDIES

4.1 Introduction

A series of full-scale spliced pile studies were conducted to demonstrate the scalability of the new post-tensioning splice system using dual embedded anchorages and to verify its bending capacity. In the full-scale spliced pile studies, four pile specimens were prepared and cast. The spliced pile specimens were manufactured as two half-length pile segments each 20 ft long. The 24 in. control pile specimens were 40 ft long. All the full-scale test specimens were cast at a commercial prestressing yard.

Based upon FDOT Standard Specifications (FDOT 2010), there are twenty 1/2" diameter special low-relaxation prestressing strands in 24 in. piles. The post-tensioning strands were located between the prestressing strands as shown in Fig. 4.1.

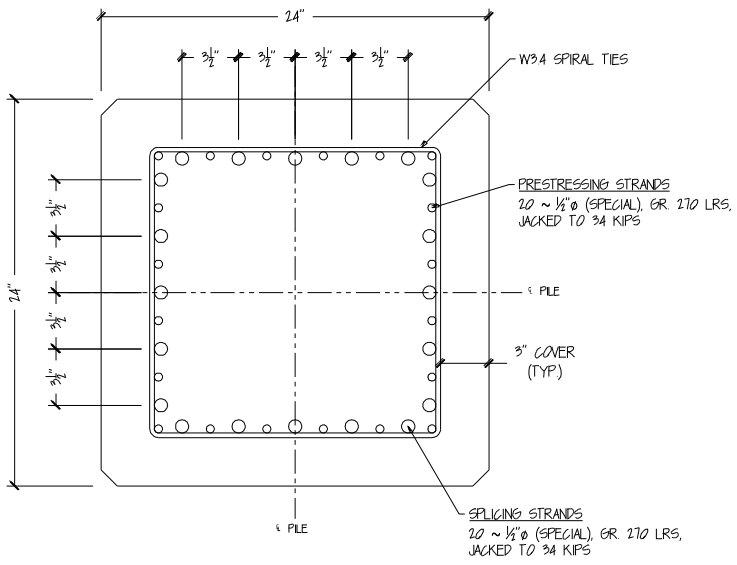

Figure 4.1 Strand configurations of full-scale test specimens. (Courtesy Mullins and Sen)

The post-tensioning ducts were placed in seven layers, symmetrically located around the cross section of the 24 in. pile. The spiral layout of the full-scale test specimens are shown in Fig. 4.2.

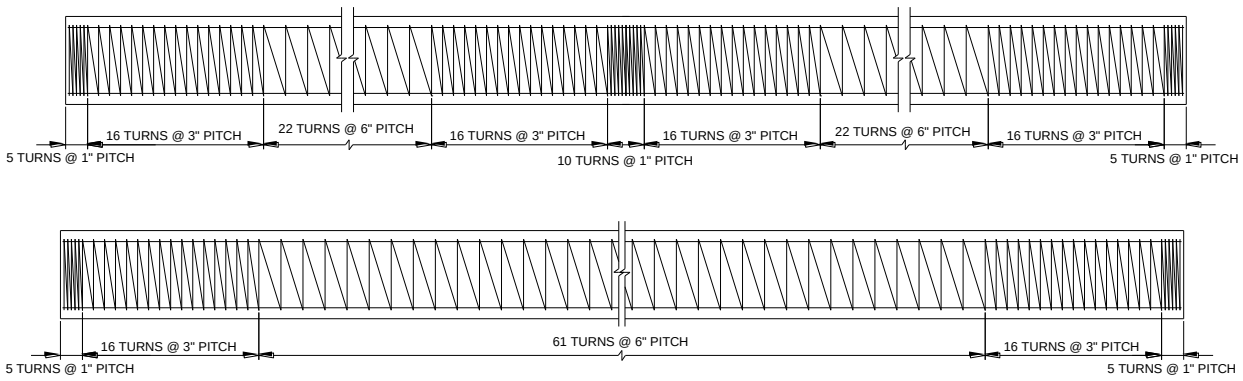

Figure 4.2 Spiral layouts of tight (top) and standard (bottom) design.

The spiral spacing in the spliced region of the spliced pile specimen is shown as the tight spiral design. One control pile was cast with standard spiral layout design while the other control pile was cast with tight spiral layout design in order to simulate the spliced pile and to assess the effect of confinement in the splice region.

4.2 Fabrication and Casting of Full-Scale Spliced Pile Specimen

The full-scale 24 in. spliced pile specimen needs 20 post-tensioning ducts and 40 anchorage assemblies.

Following similar procedures presented for the lab-scale splice pile specimens, fabrication preparations include anchorage assemblies, confinement coils, deformed ducts, grout manifolds, and 24 in. splice header plate. Fig. 4.3 shows the finished internal splicing components.

Figure 4.3 Finished internal splicing components.

All full-scale test specimens were prepared and cast at CDS Manufacturing Inc., Gretna, Florida. The internal splicing components were pre-assembled as four interchangeable panels. Each panel comprised five ducts and the predetermined duct spacing was based upon the strand configurations as shown in Fig. 4.4.

Figure 4.4 Pre-assembled five-duct interchangeable panel.

As for the lab-scale test specimens, in the transfer zone, the positioning of the internal anchorages for splicing strands was staggered to achieve a gradual superposition of stresses which avoids excessive pre-compression in the splice zone. The first pair of anchorages was placed 24 in. from the splice interface and the 10 in. stagger spacing was set for the remaining anchorages on each side. The symmetric layout avoids unwanted torsional stresses from jacking. The duct extensions were installed in the upper segment to the top of the pile.

The spliced header was inserted in the prestressing bed and the strands were threaded through the header. The duct assemblies were installed and the duct extensions were placed after the strands were tensioned. The spirals were pulled to the pre-determined spacing per FDOT Standards. The fully stressed bed and splicing header connection are shown in Fig. 4.5.

Figure 4.5 Fully stressed bed (left) and splicing header connection (right).

Similar to the lab-scale test specimens, the full-scale 24 in. test specimens were cast and cured based upon standard procedures before they were transported to Tallahassee, Florida for further studies.

4.3 Splicing of Full-Scale 24 in. Pile

The splicing procedures were performed at the Structural Research Center at the Florida Department of Transportation in Tallahassee, Florida. Before splicing, the borescope check was performed to inspect all ducts for any debris. The spring movements of wedges were also checked.

Twenty post-tensioning strands were inserted into the upper pile segment and ten feet of strands were left at the base of the upper pile segment. The exposed strands were clamped to

prevent slippage during assembly. Fig. 4.6 shows the strands that have passed the lower pile segment wedges.

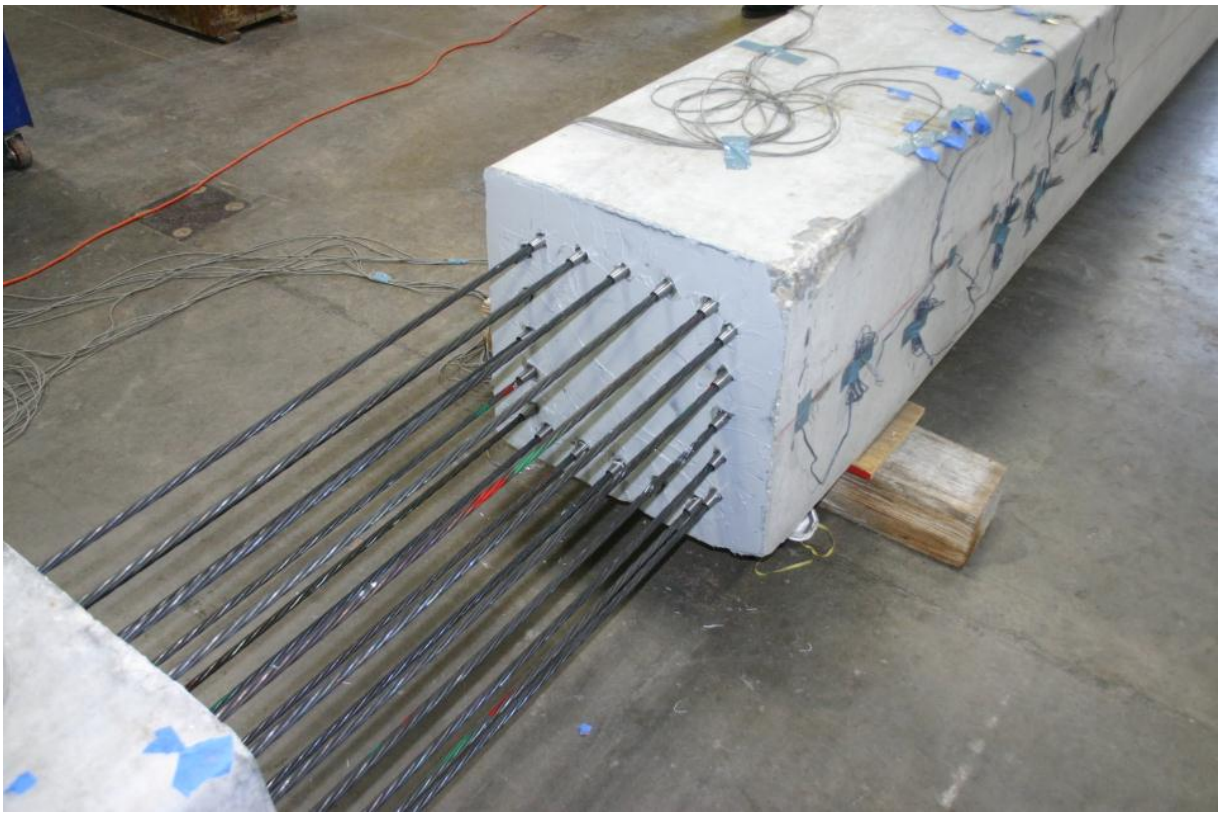

Figure 4.6 Strands passed the lower pile segment wedges.

During splicing, the upper pile segment was placed on rollers and a forklift was used to push the upper pile segment.

Before final contact, strand clamps were removed and non-sag epoxy sealant was applied to the splicing interface. Fig. 4.7 shows the final splicing stage when the pile segments were in close proximity.

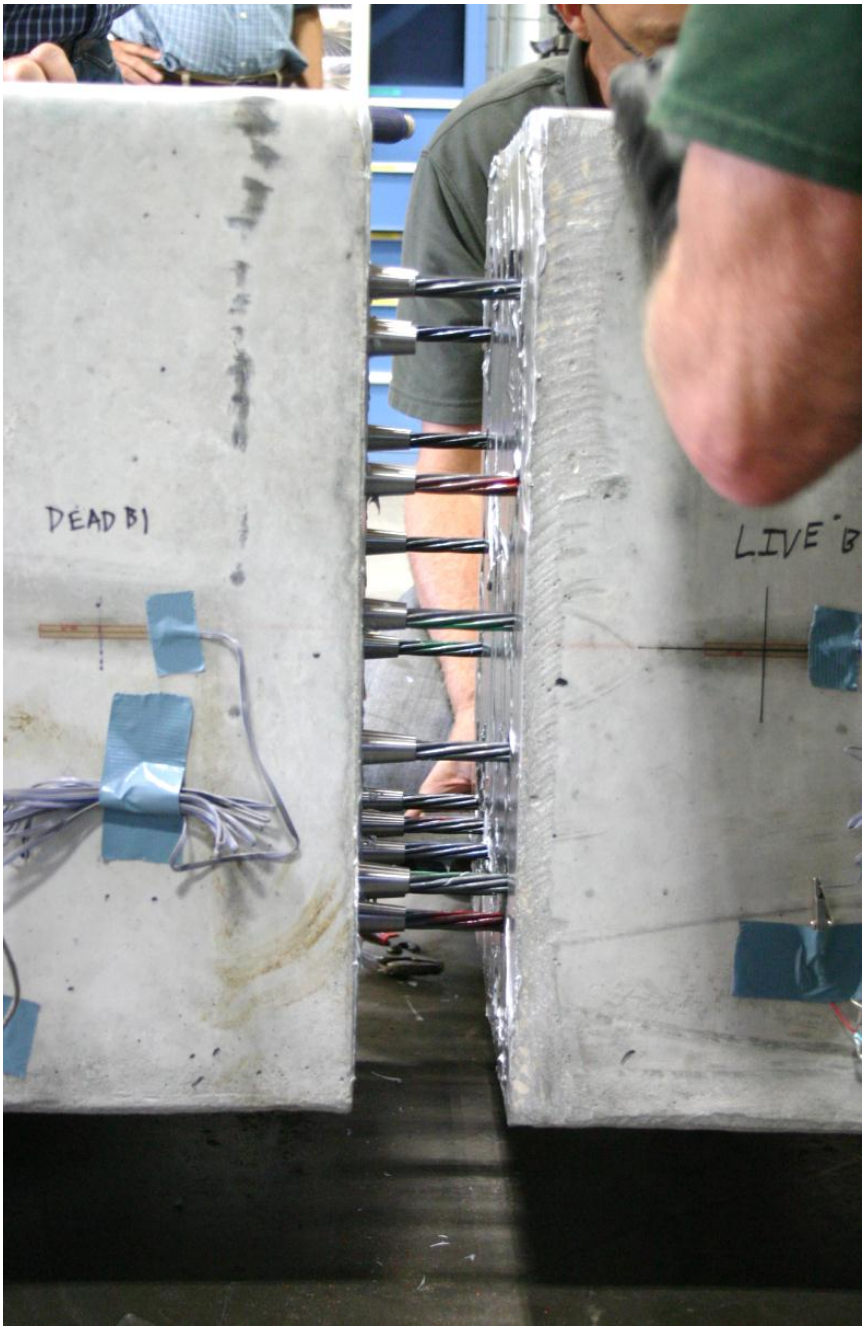

Figure 4.7 Final splicing stage when the pile segments were in close proximity.

The post-tensioning prestressing order is shown in Fig. 4.8. Each pair of opposite strands were jacked to predetermined loads in three load steps, which can maintain balanced strain and reduce prestress losses from elastic shortening of concrete. Two pairs or four strands were anchored at the same location on four faces of the pile section.

Figure 4.8 Jacking orders of strands

At the conclusion of the splicing procedure, the computed stress distributions based upon strain gage measurements are shown in Fig. 4.9.

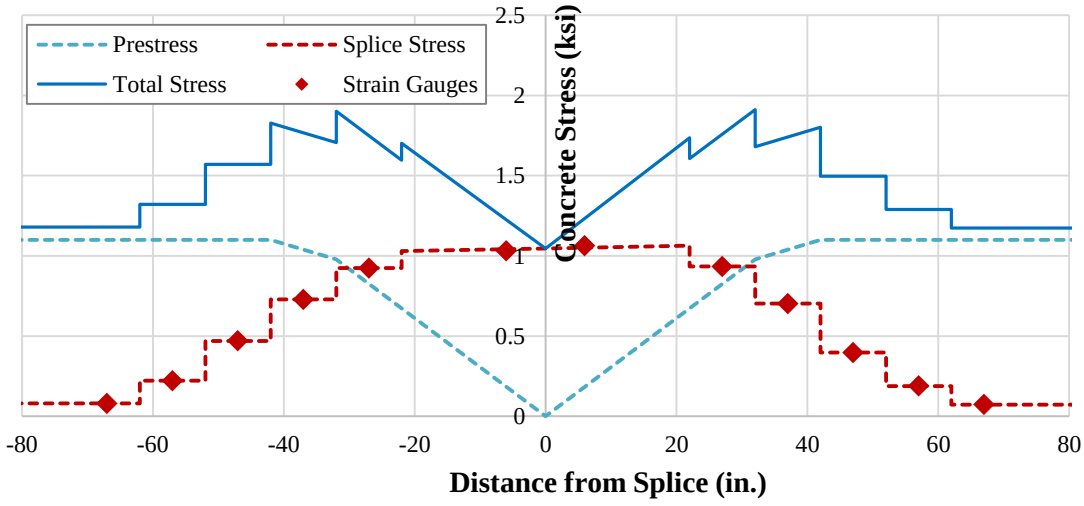

Figure 4.9 Stress distributions in the splicing procedures.

It may be seen that the staggered layouts of the dually embedded anchorages result in a gradual superimposition of stresses. The stress induced at the interface was close to the target

1000 psi. Since there was no sudden stress jump due to the staggered layouts, the excessive pre-compressive stress can be avoided at the splice zone.

After the splicing procedures, the post-tensioned strand ducts were grouted as shown in Fig. 4.10. Each panel of five ducts was piped together to provide four grouting circuits. Therefore, cable grout could be injected into any one of the ducts and returned out of the other four ducts of the circuit.

Figure 4.10 Grouting post-tensioned strand ducts.

4.4 Full-Scale Testing

A series of full-scale tests were conducted at the Structural Research Center at the Florida Department of Transportation in Tallahassee, Florida. In the tests, label C-1 refers to the control with tight spiral layout and label C-2 refers to the control with standard spiral layout. The measured concrete strength was 12,193 psi when the specimens were tested.

The four point bending test dimensions are shown in Fig. 4.11. The full-scale 24 in. piles were tested on a 38 ft span with two equal point loads applied between a 6'-6" spacing. This

setup can ensure the maximum moment under combined dead and applied load located at the mid-span, which is the critical case for testing the efficiency of the splice.

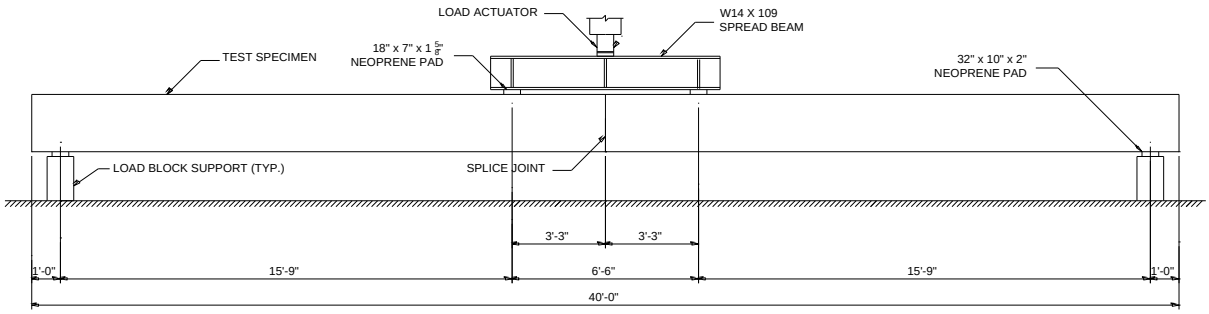

Figure 4.11 Four-point flexural test dimensions for full-scale tests.

The finished experimental setup is shown in Fig. 4.12.

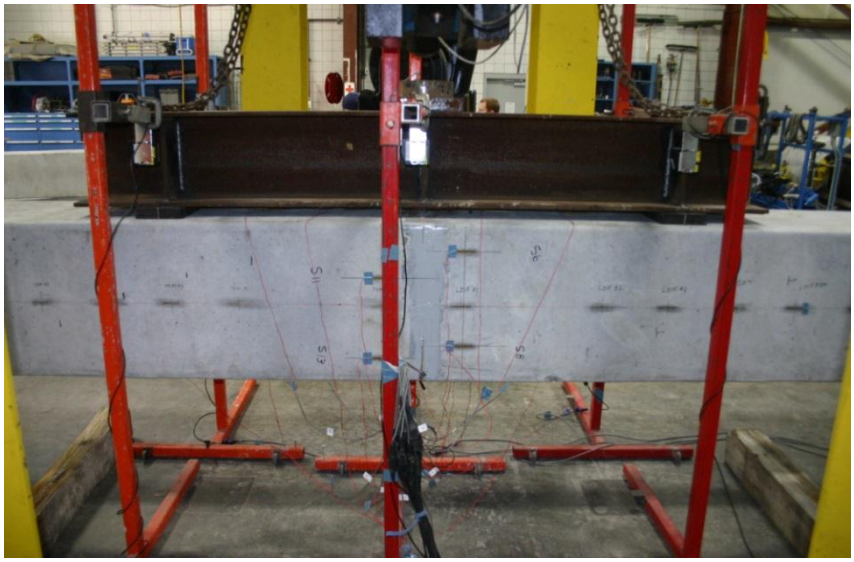

Figure 4.12 Finished experimental setup.

The initial load rate for the full-scale tests was 250lb/s through the elastic portion and gradually trailed off in relationship with the amount of damage induced into the test specimen.

The experimental data were recorded by a high resolution data acquisition system interfaced with a computer for further analysis.

4.5 Experimental Results

The failure modes in the controls and spliced pile are shown in Fig. 4.13 to Fig. 4.15.

Figure 4.13 Failure mode in standard control (C-2).

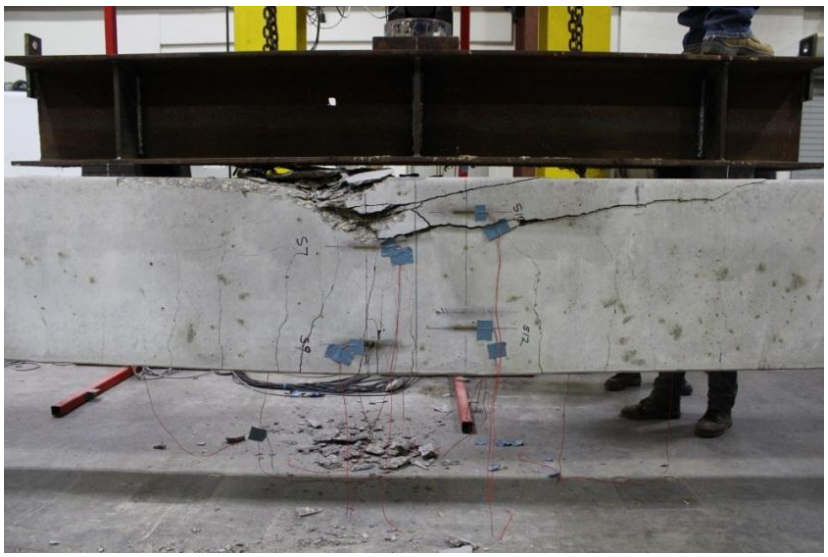

Figure 4.14 Failure mode in control with tight spiral layout (C-1).

Figure 4.15 Failure mode in spliced pile.

The controls had uniformly spaced tension cracks propagating from bottom and concrete crushed at the top compression zone.

In the spliced pile, tension cracking was confined to the spliced connection which opened when the load increased above the cracking load. Concrete crushing was confined to a relatively small region in the upper cover.

This resulted in permanent deformation of less than 0.5 in. after load was released in spliced pile. In control piles, the permanent deformations were 5.4 in. for C-1 specimen and 5.9 in. for C-2 specimen.

The permanent deformations of control specimens were much larger than that of the spliced piles. The corresponding load deflection plots appear in Fig. 4.16.

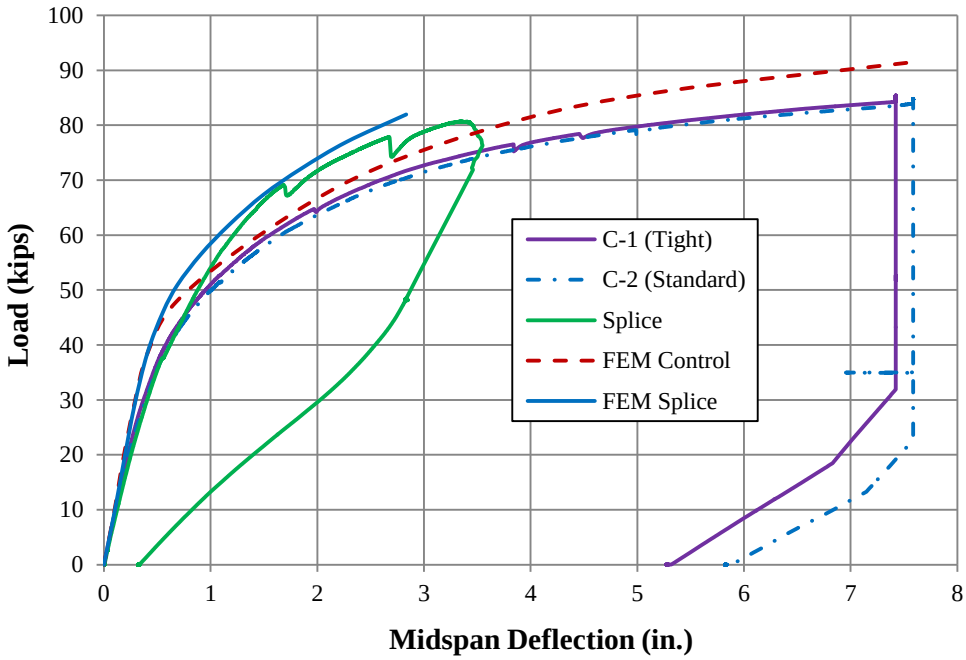

Figure 4.16 Load vs midspan deflection for controls and spliced pile.

The test results showed that the tight spiral layout in the highest moment region of the control had a minor effect on bending behavior. C-1 was slightly stiffer and exhibited smaller permanent deformation. The cracking load and the ultimate load for the spliced pile were close to that of the controls as shown in the Table 4.1.

Table 4.1 Comparison of cracking and failure loads for 24" pile specimens

Load (kips)	Controls		Splice
	Standard	Tight	
Cracking	39.6	40.2	38.7
Ultimate	84.8	85.4	80.8

4.6 Finite Element Analysis

Based on similar analysis procedures discussed in Chapter 3, the 24 in. piles were modeled using ANSYS. Comparisons between the predicted and observed load versus mid-span deflection plots are shown in Fig. 4.16. It may be seen that the predictions from the finite element models captured the overall structural response of the test specimens.

The longitudinal stress distributions for the control and splice at the ultimate stage are shown in Fig. 4.17.

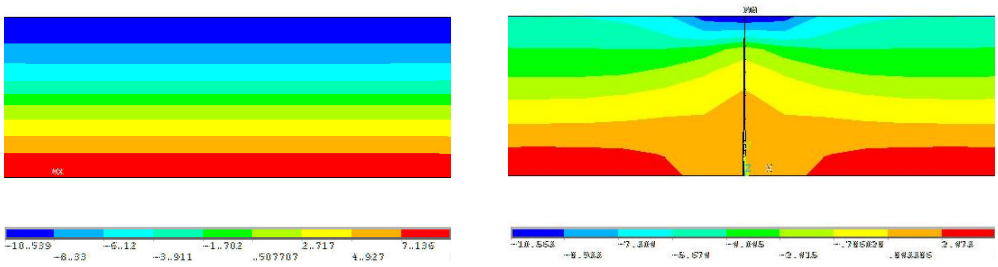

Figure 4.17 Longitudinal stress of control (left) and splice (right) at ultimate stage.

The compression failure region in the spliced pile is much smaller than that in the control as was observed in the testing (Fig. 4.13, 4.14). The analysis suggests that tensile separation at the splice interface bottom acted as a larger pivot about which the section rotated compared to the laboratory specimens.

As a result, the compression failure zone in the spliced pile is limited to a smaller region compared to the laboratory specimens.

During the tests, it was noted that, the diagonal cracks emanated from the base of the splice joint in both segments (Fig. 4.18).

Figure 4.18 Cracking patterns of 24 in. spliced pile.

Based upon current understanding, diagonal cracks should not occur in the pure tension zone. The probable explanation for this phenomenon is because of the joint opening at the splicing interface. The deformation mechanism due to plastic hinge rotation is shown in Fig. 4.19.

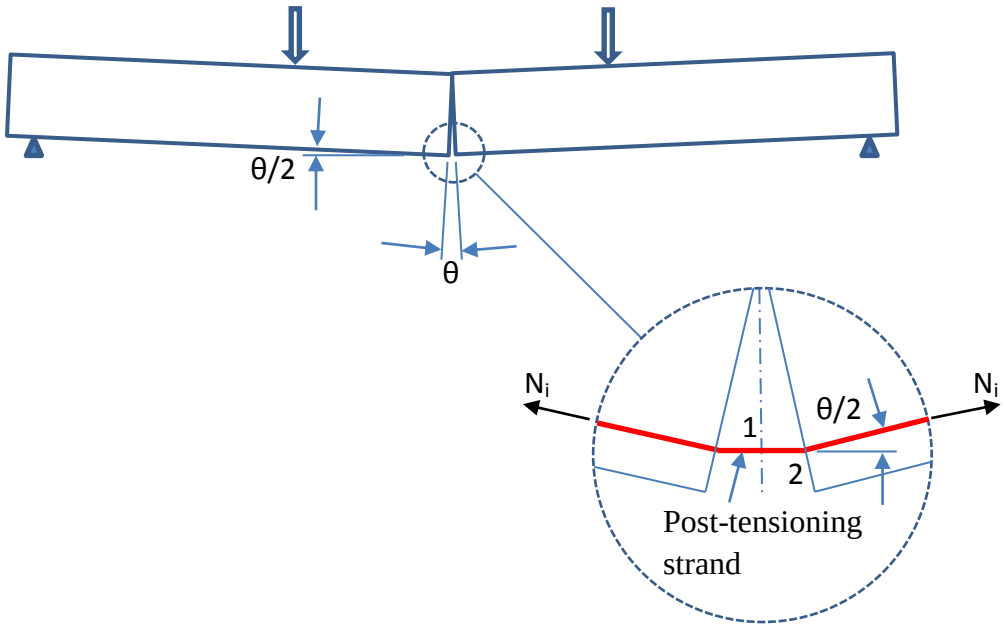

Figure 4.19 Deformation mechanism of spliced pile.

Using the equivalent load method, the force diagram is shown in Fig. 4.20.

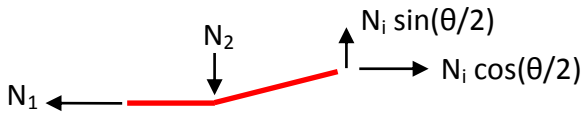

Figure 4.20 Equivalent loads.

Eq. 4.1 and 4.2 can be obtained since θ is small.

$$N_1 = N_i \cos\left(\frac{\theta}{2}\right) \approx N_i \qquad (4.1)$$

$$N_2 = N_i \sin\left(\frac{\theta}{2}\right) \approx N_i \frac{\theta}{2} \qquad (4.2)$$

It may be seen that N_2 is induced as a vertical shear component. The stress state of a concrete element in the vicinity of splice joint can be shown in Fig. 4.21.

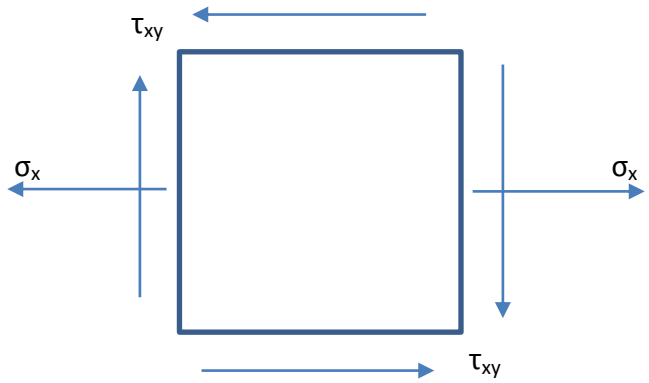

Figure 4.21 Stress state of concrete element at the vicinity of splice.

The Mohr's circle for stress state is established as shown in Fig. 4.22. The principal stress state of the element is shown in Fig. 4.23.

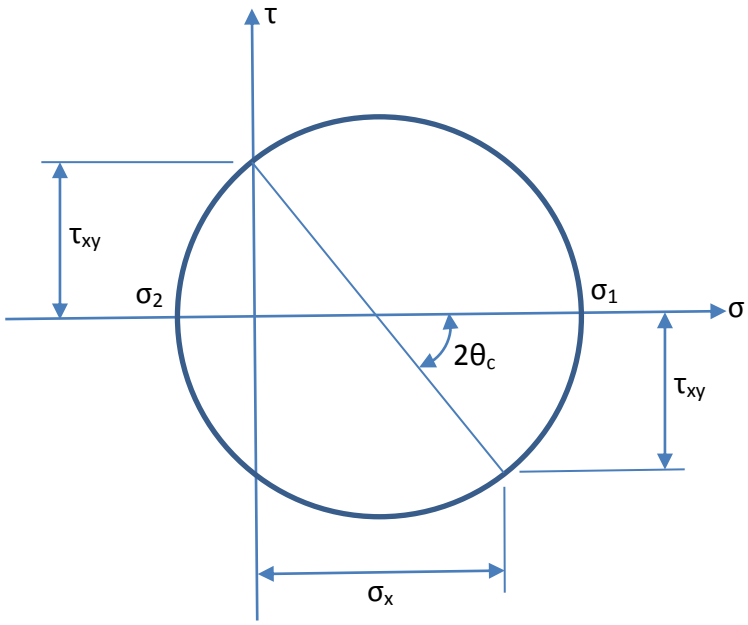

Figure 4.22 Mohr's circle of the stress state.

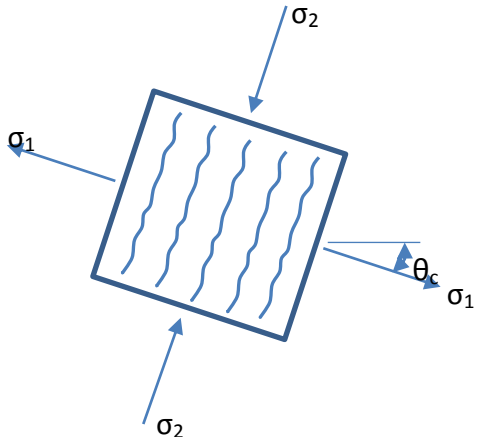

Figure 4.23 Stress state of principal stresses.

Therefore, explanations of the occurring of these abnormal diagonal cracks could attribute to the result of the inclined principal stress state. The cracks point to the joint where opening happens initially close to the location of the outer layer of post-tensioning strands. As loading continues, the secondary cracks will develop as the extensions of flexural cracks and horizontal compressive cracks.

Based upon the finite element model, the principal stress vector fields at midspan are shown in Fig. 4.24.

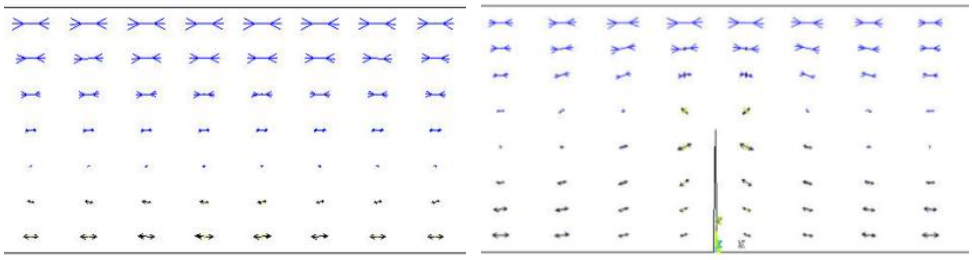

Figure 4.24 Principal stress vector fields at midspan before (Lt) and after joint opening (Rt).

It may be seen that after joint opening, the principal stress vector fields became inclined at the vicinity of the joint, indicating the possible occurrence of diagonal cracks, which is in accordance with the analytical reasoning. The cracking patterns at splice joint are shown in Fig. 4.25.

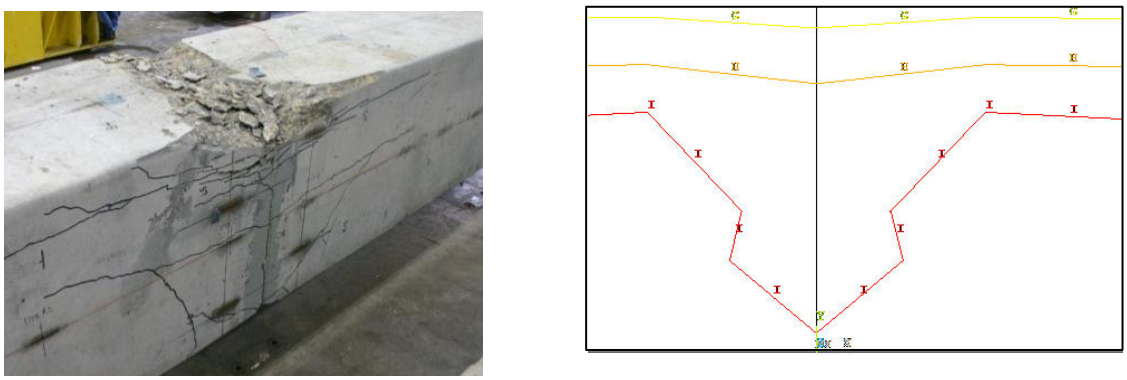

Figure 4.25 Cracking patterns at splice, experiment (Lt) and prediction (Rt).

The general trends of the predicted cracking patterns are similar to the actual cracking patterns observed in the experiments. Because of the close tie spacing (Fig.4.2), further diagonal propagation was not possible. Instead, bond splitting cracking developed along the interface between the duct and the concrete. The cracks propagated upward and were directed towards the supports when the tie spacing became larger (3 in.).

Based upon the finite element analysis, the strain variations in the post-tensioning strands are shown in Fig. 4.26. It may be seen that of the seven layers of post-tensioning strands, only one layer approaches yielding while other six layers remain in the elastic range. When the applied load is released, the spliced pile could bounce back to a large degree, which results in a small residual permanent deformation. This behavior of spliced pile is beneficial for structure in seismic zone.

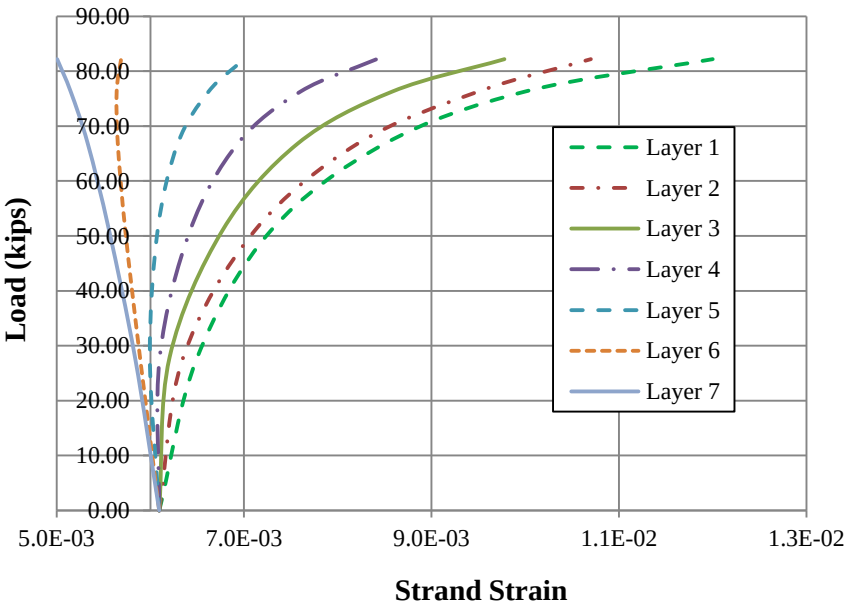

Figure 4.26 Load vs strand strain relationships for post-tensioned strands.

Due to cyclic loading in earthquake, the permanent deformation of piles will have large secondary moments on pile-supported structures, which often causes damages in earthquake. While in the post-tensioning spliced piles, the small permanent deformation will result in a minimum secondary moment. Therefore, it proves that, the new post-tensioned splicing system could achieve a better seismic resistance design.

CHAPTER 5: CONCLUSIONS

5.1 Introduction

Precast prestressed concrete piles are widely used in deep foundation construction for high-rise buildings, bridges, and offshore platforms. Heavy loads are transferred from the superstructure to the load-bearing soil strata through the pile foundation. Piles can decrease the long-term settlements and anchor the superstructures from uplifting.

The required pile lengths can be calculated based on structural loads and soils reports. However, during pile driving, unexpected site soil condition may be encountered that requires pile splicing to extend the pile length.

Aside from geotechnical considerations, due to the weight and difficulties associated with the transportation and handling of long precast piles, splicing may be necessary at the construction site. Shorter pile segments result in lower stresses and require smaller lifting capacity equipment.

Current splicing methods use mechanical connections that results in limits of stress capacity at the splice. This research solves this problem by developing a new post-tensioning splice technique. In the system, post-tensioning is introduced and confined to the splice region.

Investigations of concept splice design, laboratory tests, full-scale tests, and associated numerical modeling were performed to verify the feasibility, scalability, and efficiency of this new system. The conclusions of this study and recommendations are summarized in the following section.

5.2 Conclusions

This study describes the research effort for developing a new splicing system for precast prestressed concrete piles. The following conclusions are based on this study.

1) The conceptual design of the new post-tensioning splice using dual embedded anchorages was first implemented in laboratory prototypes. Four test specimens were fabricated including two spliced 14 in. square, 20 ft long precast prestressed concrete piles and two 14 in. square, 20 ft long control piles. Laboratory studies confirmed the feasibility of the conceptual design.

2) The scalability of the conceptual design was confirmed through full-scale testing. The test specimens included one spliced 24 in. square, 40 ft long precast prestressed concrete pile and two 24 in. square, 40 ft long control piles, which were fabricated at a commercial prestressing facility and tested at the Structural Laboratory, Tallahassee, Florida.

3) The flexural results from laboratory and full-scale tests indicated that the staggered layout of the dual embedded anchorages achieved a gradual superimposition of stresses in the splice zone. There was no sudden stress discontinuity due to the staggered layout.

4) The compressive stress induced at the splice interface was close to the target 1000 psi, which proves that prestress across the splice interface can be fully restored. The internal embedded anchorages can provide the required tension resistance while avoiding unnecessary full segment prestress.

5) The experimental results demonstrated that the spliced pile not only met but also exceeded the performance requirements of FDOT. At the ultimate stage, the spliced pile only separated at the splice and there was no failure of splicing system, which proves that the new splicing system is very effective and robust.

6) Nonlinear finite element analysis was conducted using ANSYS. The modified Hognestad concrete model and a strain hardening strand model were used in analysis. Smeared crack model was used to simulate concrete cracking behavior. The SOLID65 element was used to model concrete and LINK8 element was used for strand modeling with initial strain effect included. Contact elements were used to simulate the joint interface. William-Warnke criterion was used as the failure criterion of concrete under multi-axial stress state.

7) Through comparison with experimental results of load vs mid-span deflection, it was found that the numerical model accurately predicted the flexural behavior of the spliced piles. Agreement was better for specimens using deformed ducts because of the assumption of perfect bond. Deformed ducts improve bond between post-tensioned ducts and the surrounded concrete, which increased the bending capacity and stiffness of the spliced pile.

8) The numerical model showed that the concrete crush zone of spliced pile was smaller than that of the control. The cracking patterns of controls were typically tension-controlled. Evenly spaced tensile cracks developed in the tension zone and the top concrete crushed at the ultimate stage. The numerical model of spliced pile suggests that tensile separation at the splice interface acted as a pivot about which the section rotated. As a result, the compression failure zone in the spliced pile was limited to a smaller region. The stress distribution in the spliced pile indicated that the concrete in the cover above the splice was crushed at the ultimate stage. The ultimate capacity of the spliced pile was controlled by concrete failure.

9) The numerical results indicated that among the multiple layers of post-tensioning strands, only one layer approaches yielding while other layers remain in the elastic range. When the applied load is released, the spliced pile could rebound back to a large degree, which results in smaller residual permanent deformation. This behavior of spliced pile is beneficial for structure in

seismic zone where ground excitation may induce large secondary moments in piles due to the horizontal movement. These detrimental effects will be much smaller in the post-tensioned spliced piles.

The results of this study prove that the new technique of post-tensioning spliced pile is very effective and efficient. It meets and exceeds the splicing capacity requirements in the FDOT specifications.

The new splice restores full capacity of prestress across the joint to withstand the tensile stress that develops during pile driving. The embedded splicing components solves the corrosion problem. Its unique behavior could also achieve a much better seismic resistance design of piles, which no other commercial methods could provide.

5.3 Recommendations

Based upon the experiences accumulated in this study, recommendations are listed:

1) Cast of spliced pile could be made easier by reducing the number of splicing strands and using larger size strands, such as 16-0.6 in. low relaxation GR270 splicing strands. This improvement could also save splicing time during construction.

2) Grouting was slow because of the restrictions in the wedge assemblies. Improving flow path should be considered to save grouting time. Grout with better flow ability should be used to facilitate the grouting process.

3) Considering the complications at a casting yard, ducts should be preassembled into more convenient panels for quicker and easier field installation.

REFERENCES

[1] AASHTO (2004), LRFD Bridge Design Specifications, Third Edition, Washington DC.

[2] ACI 543R-12 (2012). Guide to Design, Manufacture, and Installation of Concrete Piles, American Concrete Institute, Farmington Hills, MI.

[3] ACI Committee 318 (2013). Building Code Requirements for Structural Concrete and Commentary. American Concrete Institute, Farmington Hills, MI.

[4] Ansley, M. (2002). "Load Test on Sure-Lock Square Pile Splice". FDOT Structures Research Center.

[5] Ansley, M., Abalo, V. and Potter, W. (2011). "Testing Square Precast Concrete Pile Splices". FDOT Structural Research Center. May.

[6] ANSYS Theory Manual V.15.0 (2013), ANSYS Inc, Canonsburg, Pennsylvania.

[7] Beitelman, T. (2011) "Structural Performance of ICP PHC Piles". FDOT Structural Research Center. September.

[8] Bruce, R. and Hebert, D. (1974). "Splicing of Precast Prestressed Concrete Piles: Part 1 – Review and Performance of Splices". PCI Journal. Vol. 19, No. 5, Sept-Oct, pp. 70-97.

[9] Bruce, R. and Hebert, D. (1974). "Splicing of Precast Prestressed Concrete Piles: Part 2 – Tests and Analysis of Cement Dowel Splices". PCI Journal. Vol. 19, No. 6, Nov-Dec, pp. 40-66.

[10] Chamberlain, R. (2010). "Industrial Concrete Products (ICP) Spun Cast Piles in Florida". Presentation slides for the 2010 FDOT/FTBA Construction Conference.

[11] Chen, W. F. (1976). Plasticity in Reinforced Concrete, McGraw-Hill, New York.

[12] Cook, R., et al. (2003), "Alternatives for Precast Pile Splices", Final Report to the Florida Department of Transportation, Contract No. BC354 RPWO #80.

[13] Fanning, P., (2001), "Nonlinear Models of Reinforced and Post-tensioned Concrete Beams", Journal of Structural Engineering, 2-2001, pp.111-117.

[14] FDOT (2010a), "Design Standards for Design Construction, Maintenance and Utility Operation on the State Highway System", Florida Department of Transportation, Tallahassee, Florida.

[15] FDOT (2010b), "State Specifications for Road and Bridge Construction", Florida Department of Transportation, Tallahassee, Florida.

[16] Gamble, W. and Bruce, R. (1990), "Tests of 24 in. Square Prestressed Piles Spliced with ABB Splice Units", PCI Journal, March/April, 1990, pp. 56-73.

[17] Gilbert, R. and Warner, R. (1978) "Tension Stiffening in Reinforced Concrete Slabs", Journal of Structural Division, ASCE, Vol.104, No.ST12, pp. 1885-1900.

[18] Gulf Coast Prestress (2015), SpunCast Concrete Cylinder Piles.

[19] Hand, F., Pecknold, D., and Schnobrich, W. (1973), "Nonlinear Layered Analysis of RC Plates and Shells", Journal of Structural Division, ASCE, Vol. 99, No. ST7, pp. 1491-1505.

[20] Hughes, T. (2000), "The Finite Element Method", Dover Publications, Inc., New York.

[21] ICP (2012). High Performance Pretensioned Spun High Strength Concrete Piles. Industrial Concrete Products, ICP Marketing SDN BHD.

[22] Kang, Y. (1977), "Nonlinear Geometric, Material, and Time Dependent Analysis of Reinforced and Prestressed Concrete Frame", PhD dissertation, University of California, Berleley, California.

[23] Kim, U. et al. (2010), "Nonlinear Finite Element Analysis of Unbonded Post-Tensioned Concrete Beams", Taylor & Francis Group, London

[24] Kupfer, H. et al. (1969), "Behavior of Concrete under Biaxial Stresses", ACI Journal, Vol. 66, No. 8, pp. 656-666.

[25] Laith, K. and Hamza, S. (2008), "Behavior of Reinforced Concrete Composite Beams with Embedded Prestressed Concrete Prisms Using Nonlinear Finite Element Analysis", The 1st Regional Conference of Eng. Sci. NUCEJ, Vol. 11, No. 1, pp. 202-215.

[26] Lau, K., Saques, A., and Powers, R. (2006), "Corrosion Performance of Concrete Cylinder Piles." NACE International, Conference Proceedings.

[27] Leet, K. and Bernal, D. (1997), Reinforced Concrete Design, 3rd Edition, McGraw-Hill, New York, NY.

[28] Lin, C. and Scordelis, A. (1975), "Nonlinear Analysis of RC Shells of General Form", Journal of Structural Division, ASCE, Vol.101, No.ST3, pp. 523-538.

[29] Lu, X. and Jiang, J. (2003), "Analysis of Concrete Structure under Complex Stress Condition with SOLID65 FEA Element of ANSYS", Building Structure, 33(6), pp.22-24.

[30] MacGregor, J.G. (1997), "Reinforced Concrete Mechanics and Design", 3rd Edition, Prentice-Hall Inc., Englewood Cliffs, NJ.

[31] Mullins, G. and Sen, R. (2015), "Investigation and Development of an Effective, Economical, and Efficient Concrete Pile Splice", Final Research Report, FDOT, Tallahassee, Florida.

[32] Mullins, G., Sen, R., and Sagues, A. (2012). "Design and Construction of Precast Piles with Stainless Steel Reinforcing Steel," Progress Report Submitted to FDOT in partial fulfillment of RFRP # 09/10-001, March.

[33] Naaman, A. (2004), "Prestressed Concrete Analysis and Design", 2nd Edition, published by Techno Press 3000.

[34] Nawy, E. G. (1996), "Prestressed Concrete", 2nd Edition, published by Prentice Hall.

[35] Nilson, A. (1987), "Design of Prestressed Concrete", John Wiley & Sons, 2nd Edition.

[36] PCI Design Handbook (1999), Precast and Prestressed Concrete, 5th Edition, Chicago, IL.

[37] Rogowsky, D. and Marti, P. (1991), "Detailing for Post-Tensioned," VSL International, Ltd., Bern, Switzerland, VSL Report Series.

[38] Schuler, G. (2009), "Producer's Experience with 10,000 psi Concrete and 0.7-in. Diameter Strands," HPC Bridge Views, Issue No. 54, March/April 2009.

[39] Scordelis, A. (1984), "Computer Models for Nonlinear Analysis of Reinforced and Prestressed Concrete Structures", PCI Journal, Nov./Dec. 1984, pp. 116-135.

[40] Si, B. and Sun, Z. et al. (2007), "The Application of Solid65 Element in the Finite Element Analysis of Concrete Structure", Industrial Construction, 2007.

[41] Timoshenko, S. and Woinowsky, S. (1959), "Theory of Plates and Shells", McGraw-Hill Inc., 2nd Edition.

[42] Timoshenko, S. and Gere, J. (1972), "Mechanics of Materials", Van Nostrand Reinhold.

[43] Tokyo Concrete Industry Co. Ltd. (1968), "Experimental Study on Structural Characteristics of Joint for Tokyo System PC Pile", Tokyo, Japan.

[44] Venuti, W. (1980), "Efficient Splicing Technique for Precast Prestressed Concrete Piles", PCI Journal, Sept/Oct, 1980, pp.102-124.

[45] William, K., and Warnke, E. (1975), "Constitutive Model for the Triaxial Behavior of Concrete", Proceedings of the International Association for Bridge and Structural Engineering, p.174, 1975.

[46] Zienkiewicz, O. and Taylor, R. (2000), "The Finite Element Method", Vol 1, 5th Edition. Butterworth-Heinemann, Oxford.

APPENDIX A: THEORETICAL CALCULATIONS OF PRESTRESS LOSSES

The calculations of prestress losses are based upon AASHTO lump sum method. In prestressed concrete structures, the stress in the prestressed strand decreased continuously due to several factors, such as elastic shortening, relaxation of strands, shrinkage of concrete, anchorage set, creep of concrete and so on. The detailed calculations are shown in the following.

- Prestress loss due to Anchorage seating:

Anchorage seating is the distance that the wedges set in to lock the prestressing strand. Based on a series of chuck experiments, the wedge set movement of 0.073 inch was obtained. This value was used in the following calculations for prestress loss due to anchorage seating.

$$\Delta f_p(0) = E_{ps}\frac{\delta}{L} = 27890 \times \frac{0.073}{10 \times 12} = 16.966ksi$$

The prestress loss due to the strand relaxation before transfer can be represented using the value of Δf_{pR1}.

$$\Delta f_{pR1} = \frac{\log(24t)}{40}\left(\frac{f_{pJ2}}{f_{py}} - 0.55\right)f_{pJ2}$$

where t is the time in days from stressing to transfer; f_{pJ2} is the initial stress in strand at the end of stressing; and f_{py} is the yield strength of strand.

$$f_{pJ2} = 0.75f_{pu} - \Delta f_p(0) = 0.75 \times 300 - 16.966 = 208.034\ ksi$$

$$\Delta f_{pR1} = \frac{\log(24 \times 3)}{40}\left(\frac{208.034}{270} - 0.55\right) \times 208.034 = 2.13\ ksi$$

$$208.034 - 2.13 = 205.904\ ksi$$

- Prestress losses due to elastic shortening:

$$\Delta f_{pES} = n_{pi}(f_{cgp})_{F_i+G}$$

$$n_{pi} = \frac{E_{ps}}{E_{ci}} = \frac{27890}{57\sqrt{6396}} = 6.12$$

$$(f_{cgp})_{F_i+G} = \left(\frac{F_i}{A_c} + \frac{F_i e_0^2}{I}\right) - \frac{M_G e_0}{I} = 1.286\ ksi$$

$$\Delta f_{pES} = 6.12 \times 1.286 = 7.87\ ksi$$

- Prestress loss due to shrinkage:

$$\Delta f_{pS} = 17 - 0.15RH = 17 - 0.15 \times 60 = 8\ ksi$$

where RH is the relative humidity and 60% is assumed.

- Prestress loss due to creep of concrete:

$$\Delta f_{pC} = 12(f_{cgp})_{F_i+G} - 7\left(f_{cgp}\right)_{sD} = 12 \times 1.286 = 15.43\ ksi$$

- Prestress loss of strand relaxation due to concrete elastic shortening, shrinkage, and creep:

$$\Delta f_{pR2} = 20 - 0.4 \times \Delta f_{pES} - 0.2 \times (\Delta f_{pS} + \Delta f_{pc})$$

$$\Delta f_{pR2} = 12.167\ ksi$$

- The time-dependent losses:

$$8 + 15.43 + 12.167 = 35.597\ ksi$$

- The effective prestress after losses:

$$f_{pe} = 205.904 - 7.867 - 35.597 = 162.44\ ksi$$

- Effective pre-compression in concrete:

$$\mathrm{f_{pc}} = \frac{\mathrm{f_{pe}}(8 \times 0.153\mathrm{in}^2)}{\mathrm{A_c}} = 1.014\mathrm{ksi}$$

The stress induced is close to the target 1000 psi pre-compressive stress across splice interface.

APPENDIX B: STRAIN COMPATIBILITY ANALYSIS

The strain compatibility procedures are shown in the following for 14" spliced pile.

- Dimension of the pile: width b = 14 in., height h = 14 in.
- Gross area of the cross section of the pile: A_g = b x h = 196 in^2
- Concrete ultimate compressive strain: ε_{cu} = 0.003
- Concrete compressive strength: f_c' = 9104 psi
- Strand ultimate tensile strength: f_{pu} = 300 ksi
- Strand yield strength: $f_{py} = 0.9\ f_{pu}$ = 270 ksi for low relaxation strands
- Effective prestress: f_{pe} = 162.44 ksi
- Young's Modulus of the strand: E_{ps} = 27890 ksi
- Area of the strand: A_{ps} = 8 x 0.153 in^2 = 1.224 in^2
- Net cross sectional area: $A_n = A_g - A_{ps}$ = 196 – 1.224 = 194.776 in^2
- Effective concrete stress:

$$\varepsilon_{ce} = \frac{A_{ps}\, f_{pe}}{A_n\, E_c} = \frac{1.224 \times 162.44}{194.776 \times 5439} = 1.877 \times 10^{-4}$$

- Effective strand stress:

$$\varepsilon_{pe} = \frac{f_{pe}}{E_{ps}} = \frac{162.44}{27890} = 5.824 \times 10^{-3}$$

After several iteration calculations, the depth of neutral axis was determined as: c = 4.1205 in.

The depth of equivalent compressive block: $a = \beta_1 c$ = 0.65 x 4.1205 = 2.678 in.

- Consultant compressive force: $C_c = 0.85f_c'ba = 290.163$ kips
- d_i is the distance from extreme compressive side to the i^{th} layer of strand.

$$i = 1 \text{ to } 4$$

$$d := \begin{pmatrix} 10.5 \\ 8.75 \\ 5.25 \\ 3.5 \end{pmatrix}$$

- The strain change in i^{th} layer of strand:

$$\Delta\varepsilon_{psi} = \varepsilon_{ce} + \varepsilon_{cu}\left(\frac{d_i - c}{c}\right)$$

$$\Delta\varepsilon_{ps} := \begin{pmatrix} 4.832 10^{-3} \\ 3.558 10^{-3} \\ 1.010 10^{-3} \\ -2.641 10^{-4} \end{pmatrix}$$

- The strain in i^{th} layer of strand: $\varepsilon_{psi} = \varepsilon_{pe} + \Delta\varepsilon_{psi}$

$$\varepsilon_{ps} := \begin{pmatrix} 0.011 \\ 9.383 10^{-3} \\ 6.834 10^{-3} \\ 5.560 10^{-3} \end{pmatrix}$$

- Proportional limit of strand: $\varepsilon_{pp} = 0.007$

If ε_{psi} is less than ε_{pp}, then f_{psi} is equal to $E_{ps}\ \varepsilon_{psi}$; otherwise, f_{psi} needs to be determined based on strain hardening model.

$$f_{psi} = E_{ps}\varepsilon_{psi}\left\{0.029 + \frac{0.971}{\left\{1 + \left(101.489\varepsilon_{psi}\right)^{9.942}\right\}^{0.101}}\right\}$$

$$f_{ps} := \begin{pmatrix} 248.542 \\ 236.945 \\ 190.610 \\ 155.075 \end{pmatrix} \cdot ksi$$

The Force in i^{th} layer of strand, T_{ip} is equal to $A_{psi}f_{psi}$. The strain in i^{th} layer of duct is represented as ε_{di}.

$$\varepsilon_{di} = \frac{\varepsilon_{cu}}{c}(d_i - c)$$

$$\varepsilon_d := \begin{pmatrix} 5.051 \cdot 10^{-3} \\ 3.709 \cdot 10^{-3} \\ 1.025 \cdot 10^{-3} \\ -3.165 \cdot 10^{-4} \end{pmatrix}$$

Yield strain of duct ε_{dy} is found using grade (GR) over Young's Modulus of duct E. If ε_{di} is greater than ε_{dy}, f_{di} can be determined as $E\varepsilon_{dy}$; otherwise, f_{di} is equal to $E\varepsilon_{di}$.

The force in i^{th} layer of duct, T_{di} can be found using $A_{di}f_{di}$. The nominal force resistance is represented as P_n. Summing up the axial forces on the section leads to the nominal force resistance P_n.

$$P_n = C_c - \sum_i T_{ip} - \sum_i T_{id}$$

$$p_n = -1.035 \times 10^{-4} \text{ kips}$$

Since P_n is very close to zero, the iteration calculations can be stopped. Summing up the moments with respect to the centerline leads to the nominal moment resistance M_n.

$$M_n = C_c\left(\frac{h}{2} - \frac{a}{2}\right) + \sum_i T_{ip}\left(d_i - \frac{h}{2}\right) + \sum_i T_{id}\left(d_i - \frac{h}{2}\right)$$

$$M_n = 153.747 \text{kips·ft}$$

The experimental result of M_n is 144.206 kips-ft. Compared with the results of strain compatibility analysis, the difference percentage is 6.6%.

APPENDIX C: PROPERTIES OF MATERIALS

EUCO cable grout was in this study. It is a high performance cable grout. The properties of the grout are shown in Table. C.1.

Table C.1 Properties of EUCO cable grout

Properties	Results @ 1.5 gal/50 lb mix water
Flow rate	9 to 20 sec initial flow 9 to 30 sec at 30 min.
Initial Setting Time at 70^{o}F	8 to 12 hours
Compressive Strength	7 days: >3,000 psi 28 days: >7,000 osi
Hardened Height Change	24 hours: 0.0%~0.1% 28 days: 0.0%~0.2%
Plastic Expansion	0.0%~2.0% for up to 3 hours
Wick Induced Bleed	0.0% at 3 hours
Schupack Pressure Bleed Test	0.0% (5 minutes)
Chloride Permeability	28 days (30V for 6 hrs) <2,500 Coulombs

DURAL106 epoxy was used in this study. It is a slow-setting precast segmental epoxy adhesive. The properties of the epoxy are shown in Table. C.2.

Table C.2 Properties of DURAL106 epoxy

Properties	Results within 60 ^{o}F~90^{o}F
Sag Resistance at High Temperature	Non-Sag
Gel Time at High Temperature	3 hours 40 minutes
Compressive Yield	7 days: 6,023 psi 14 days: 8,510 psi
Heat Deflection Temperature, 14 days	>140^{o}F
Open Contact Time at High Temperature	6 hours
Bond Strength, 14 days	>5,065 psi
Contact strength	3,623 psi at 14 days

High-strength concrete was used in this study. The properties of concrete are shown in Table C.3

Table C.3 Concrete compressive strengths

Series	Concrete Age (days)	Concrete Compressive Strength f'_c (psi)		
		Cylinder 1	Cylinder 2	Average
Lab Test 1	3	6344	6448	6396
	14	7874	7706	7790
	91	9324	9431	9377
Lab Test 2	3	5672	6000	5836
	10	7644	7754	7699
	56	9064	9143	9104
Full-Scale Test	65	11994	12391	12193

The post-tensioning duct used in this study was a galvanized GR60 steel pipe with outer diameter of 0.92 in. and inner diameter of 0.82 in. The cross-sectional area of the duct is calculated as 0.137 in^2.

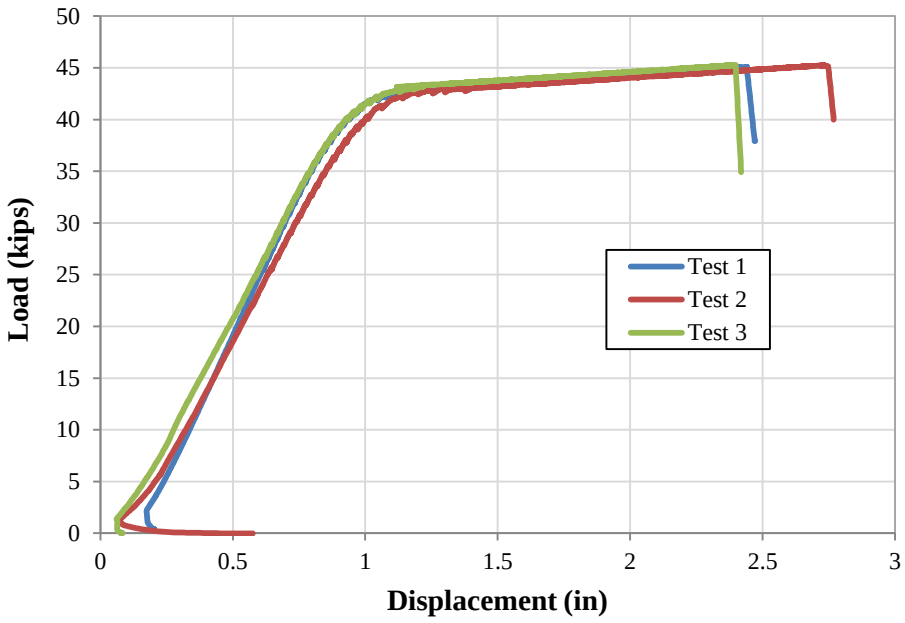

Figure C.1 Load vs displacement for strands used in tests. (Courtesy Mullins and Sen)

The High-strength low-relaxation ½" strands were used in this study. The jacking stress was 75%f_{pu}. The nominal ultimate strength is 270 ksi. Based upon the experimental tests, the ultimate strength can be as high as 300 ksi. The load-displacement relationships of the strands are shown in Fig. C.1.

APPENDIX D: FINITE ELEMENT ANALYSIS USING ANSYS

Finite element analysis using ANSYS is a complicated procedure which requires knowledge of finite element modeling and familiarity with ANSYS software. ANSYS provides a layer by layer Windows interface which is available for use based on modeling need. This study used the SOLID65 element for concrete modeling. The details of the SOLID65 element are shown in the Fig. D.1.

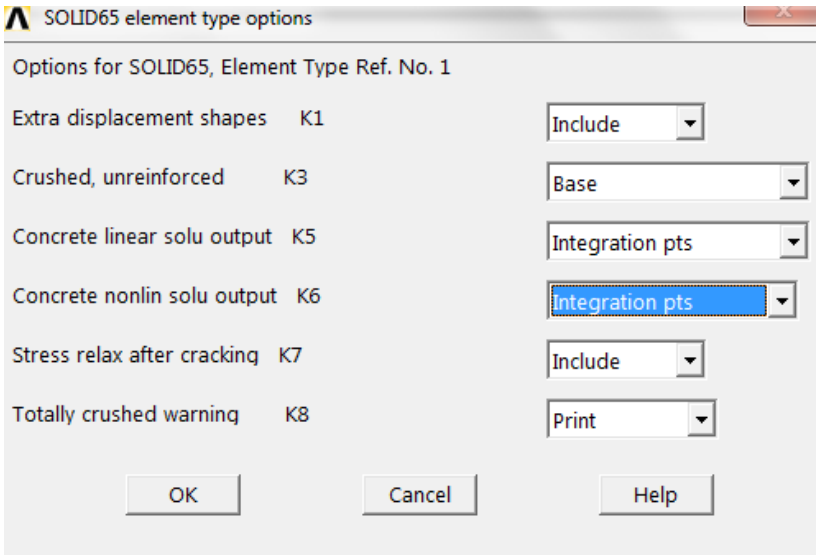

Figure D.1 SOLID65 element input interface.

It should be noted that the stress relaxation after cracking should be set as “include” to better simluate concrete softening behavior and attain convergnece. A smeared crack model was used so the shear transfer coefficents were defined in Fig. D.2.

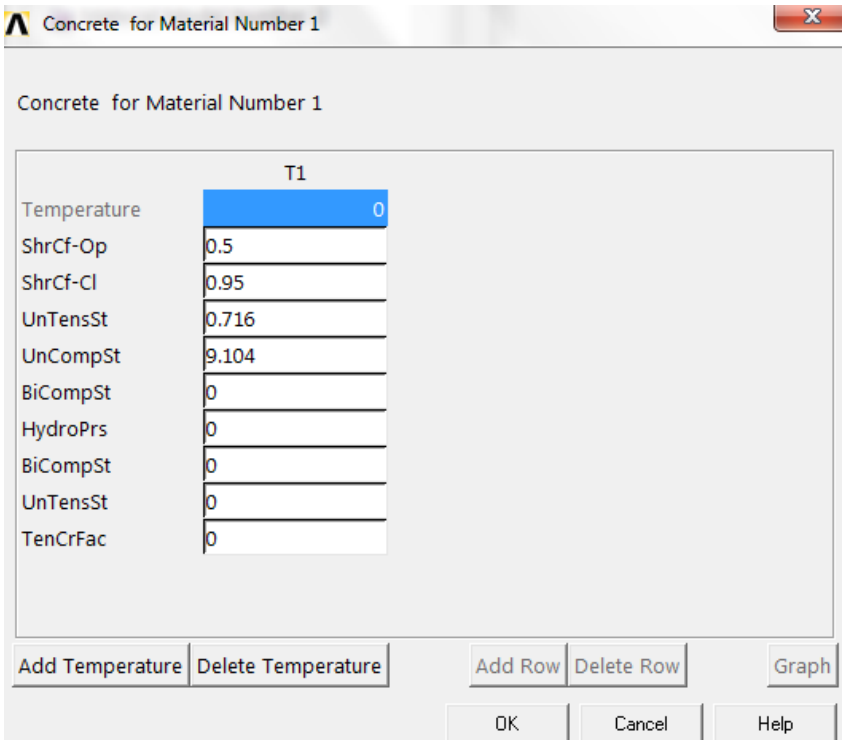

Figure D.2 Shear transfer coefficients.

The shear transfer coefficient incorporates the effect of dowel action of reinforcement across a crack and the aggregate interlock action along the crack interface. For 3D analysis, ANSYS provides two separate shear transfer coefficients: open crack shear transfer coefficient is applied to consider the shear transfer of opening concrete cracks and closed crack shear transfer coefficient is applied to consider the shear transfer of closed concrete cracks.

These shear transfer coefficients range from 0.0 to 1.0, where 0.0 refers to very smooth cracks with zero shear transfer; 1.0 refers to very rough cracks so that there is no loss of shear transfer.

The “ShrCf-Op” refers to shear coefficient for open cracks and it was specified as 0.5; the “ShrCf-Cl” refers to shear coefficient for closed cracks and it was set as 0.95.

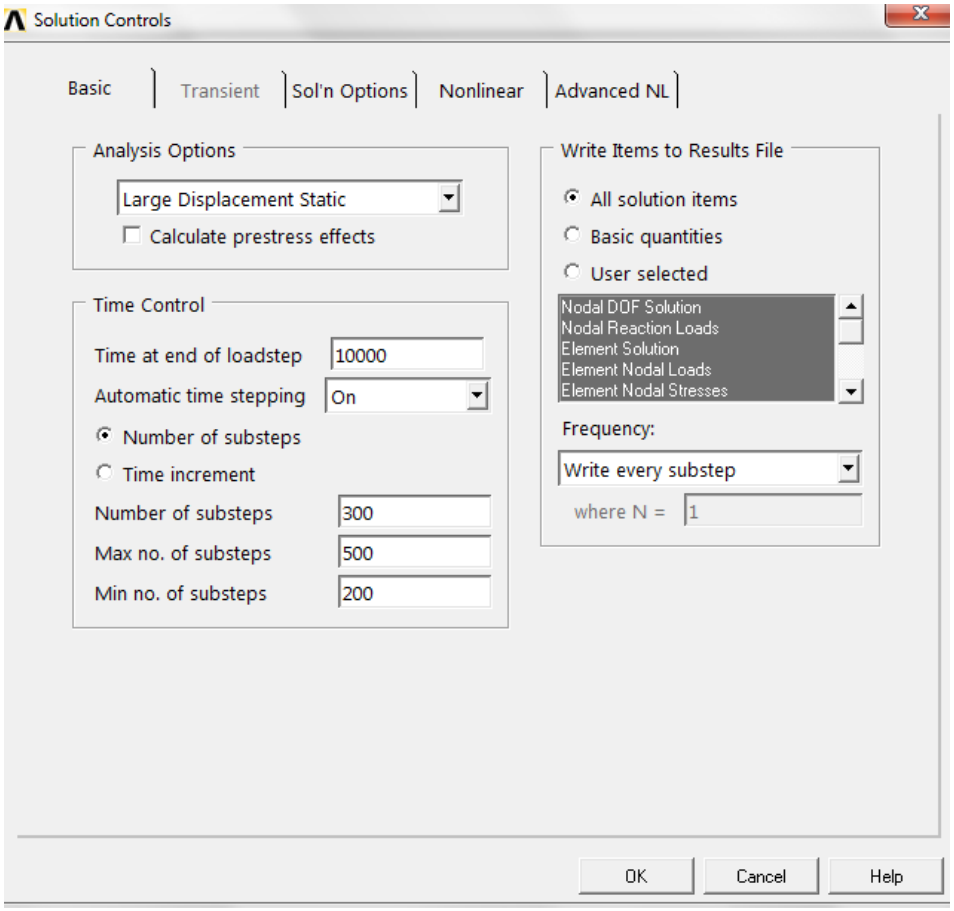

Figure D.3 Nonlinear analysis solution controls.

In nonlinear analysis, the load is applied in steps. The iterative analysis is performed in each load step. The solved force and displacement in current load step are applied in the next load step calculations, which can provide good approximations.

The nonlinear analysis options in solution controls are shown in Fig. D.3. Large displacement analysis was turned on to include geometric nonlinearity. The nonlinear analysis was conducted in steps and the numbers of load steps are defined in Fig. D.3. It should be noted that frequency was set as “write every substep” to make sure a full Newton-Ralphson method was performed at each step. The convergence criteria input interface is shown in Fig. D.4.

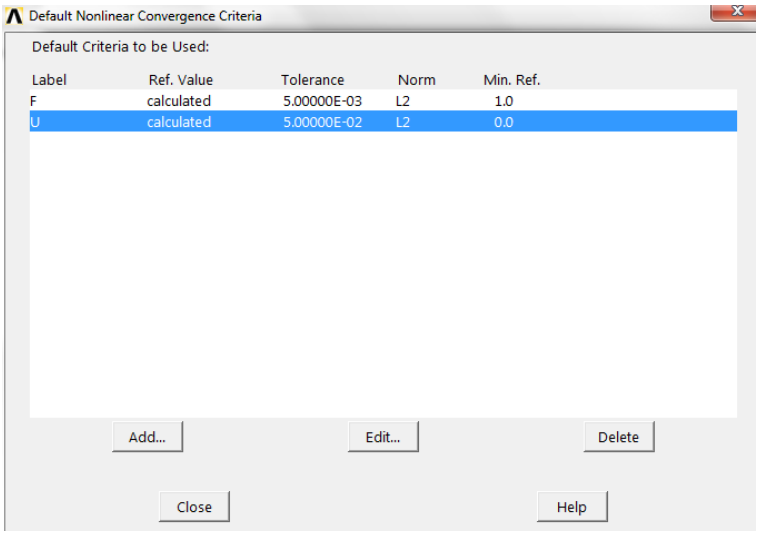

Figure D.4 Convergence criteria input interface.

The tolerance limits were set as 0.5% for force check and 5% for displacement check. The solution option was specified as sparse direct as shown in Fig. D.5.

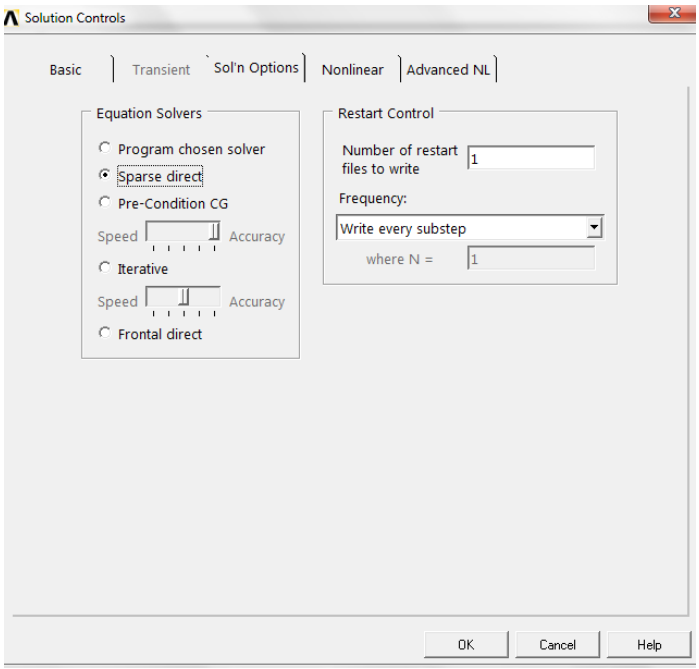

Figure D.5 Solution options in controls.

APPENDIX E: COPYRIGHT PERMISSIONS

The copyright permissions are shown in the following.

Zhongxin Wu <zwu@mail.usf.edu> Tue, Nov 1, 2016 at 2:59 PM
To: gmullins <gmullins@usf.edu>

Good afternoon, Dr. Mullins,

Thank you very much. I am interested in obtaining copyright permissions for the following graphs from your research for my dissertation.

Best Regards,

Zhongxin Wu
Department of Civil and Environmental Engineering
University of South Florida

Mullins, Gray <gmullins@usf.edu> Tue, Nov 1, 2016 at 4:39 PM
To: "Wu, Zhongxin" <zwu@mail.usf.edu>

Dr. Wu,

You are hereby permitted to use the requested images (below).

Regards,

Gray Mullins, Ph.D., P.E.

Professor

Department of Civil and Environmental Engineering

University of South Florida

4202 E. Fowler Avenue, ENB 118

Tampa, FL 33620

Figure 3.1

Figure 3.9

Figure 4.1

Figure C.1